UNIVERSITY OF CALIFORNIA,
IRVINE

Power Optimization for Fully-Implantable Brain-Computer Interfaces

DISSERTATION

submitted in partial satisfaction of the requirements
for the degree of

DOCTOR OF PHILOSOPHY

in Biomedical Engineering

by

Claudia Serrano Amenos

Dissertation Committee:
Professor Zoran Nenadic, Chair
Associate Professor Beth Lopour
Associate Professor Christine King

2023

© 2023 Claudia Serrano Amenos

DEDICATION

To my family

TABLE OF CONTENTS

Page

LIST OF FIGURES **v**

LIST OF TABLES **ix**

ACKNOWLEDGMENTS **x**

VITA **xi**

ABSTRACT OF THE DISSERTATION **xiii**

1 Introduction and Background **1**
- 1.1 Brain-Computer Interfaces . . . 1
  - 1.1.1 Signal Acquisition . . . 2
  - 1.1.2 Neural Signals . . . 4
  - 1.1.3 BCI Decoders for Motor Applications . . . 5
  - 1.1.4 Bi-directional BCIs . . . 10
- 1.2 Our Envisioned BD-BCI . . . 10
- 1.3 Active Implants . . . 15
  - 1.3.1 Thermal Safety . . . 17
- 1.4 Significance . . . 19

2 Power Budget of the Chest Wall Unit **21**
- 2.1 Motivation . . . 21
- 2.2 Methods . . . 22
  - 2.2.1 Bio-heat Model . . . 23
  - 2.2.2 Sensitivity Analysis . . . 28
  - 2.2.3 Benchtop Validation . . . 30
- 2.3 Results . . . 35
  - 2.3.1 Bio-heat Model . . . 35
  - 2.3.2 Sensitivity Analysis . . . 36
  - 2.3.3 Benchtop Validation . . . 38
- 2.4 Discussion . . . 41
- 2.5 Conclusion . . . 46

3 Power Budget of the Skull Unit **47**
3.1 Motivation . . . 47
3.2 Materials & Methods . . . 48
3.2.1 Geometric Model . . . 48
3.2.2 Mathematical model . . . 50
3.2.3 Sensitivity Analysis . . . 60
3.3 Results . . . 63
3.3.1 Nominal Model . . . 63
3.3.2 Sensitivity Analysis . . . 65
3.4 Discussion . . . 67
3.5 Conclusion . . . 71

4 ECoG-based Step Decoder **73**
4.1 Motivation . . . 73
4.2 Methods . . . 74
4.2.1 Data Collection . . . 74
4.2.2 Decoder Overview . . . 75
4.2.3 Decoder Training . . . 78
4.2.4 Decoder Testing . . . 85
4.3 Results . . . 87
4.3.1 Subjects . . . 87
4.3.2 Feature Extraction . . . 87
4.3.3 Fokker-Planck-based Bayesian Filter . . . 88
4.3.4 Decoder Performance . . . 89
4.4 Discussion . . . 92
4.5 Conclusion . . . 95

Bibliography **97**

Appendix A MATLAB Code of the Step Decoder **117**

LIST OF FIGURES

Page

1.1 Diagram of a typical BCI system. Recorded brain signals are decoded into control commands for an external device. Different recording modalities, signal processing techniques, and external devices are used for different BCI applications. 2

1.2 Sketch of human head tissues and different non-invasive (EEG) and invasive (ECoG and MEA) recording modalities. The annotated dimension ranges are based on common designs for each technique. The scales of the electrodes and head tissues are altered for illustration purposes. 3

1.3 Example of ERS and ERD from ECoG signals during elbow movement intervals. (A) Time series of the μ (green) and γ (orange) powers, as well as gyroscope (black). During motor movement (gyroscope $\neq 0$), μ-power decreases (ERD), while γ-power increases (ERS). (B) Spectrogram of ECoG signals up to 160 Hz and gyroscope signal. ERD is visible at $\sim$ 10–30 Hz, and ERS is apparent at $<$10 Hz and $>$40 Hz. 6

1.4 Types of motor decoder architectures. (A) Classical approach, where first features are extracted from the raw neural signals and then the decoder uses a classifier/regression to generate the decoded output. (B) Deep learning approach where both feature extraction and classification/regression are learned together. (C) Hybrid decoder where multiple classification/regression decoders are implemented simultaneously and their individual outputs are combined to generate one final decoded output. 7

1.5 Diagram of a BD-BCI paradigm. Recorded brain signals are decoded into control commands for an end-effector. Sensors in the end-effector capture motion signals, which, in turn, are converted into a stimulation signal that is delivered to the sensory cortex to elicit artificial sensation. 11

1.6 Envisioned fully-implantable BD-BCI system for restoration of walking and leg sensation. The system comprises several implantable subsystems. A skull unit (SU) (2) is implanted on the exterior aspect of the skull and is connected to the motor (1) and sensory (6) ECoG grids. A chest wall unit (CWU) (4) is implanted subcutaneously in the pectoral area. The SU and CWU are connected by a subcutaneous tunneling cable (3), similar to the current deep brain stimulator (DBS) design. The system communicates wirelessly with an external exoskeleton (5). 12

2.1 Geometric model of the thoracic area and CWU from different views, dimensions in mm. (A) 3D view. The red line indicates the axis where the thermal impact due to the CWU is highest, see Section 2.3.1 for details. (B) Central cross-section of the volume in (A). (C) A zoomed-in view of the inset in (B). (D) Different layers of the CWU. 24
2.2 Different views of our custom-designed CWU thermal prototype and its COMSOL model. (A) View of the prototype's interior prior to laser-welding the two clamshells. Different switch positions engage different combinations of resistors for the prototype to operate at different powers. (B) A front view of the laser-welded prototype. (C) Cross-section of the prototype's COMSOL model (lateral view). (D) Cross-section of the prototype's model (top view). 32
2.3 Temperature increase, $\Delta T(P_{\mathrm{CWU}})$, for different values of P_{CWU}, calculated along the axis of the CWU with the tissues' highest ΔT. This region undergoes the highest thermal impact within the overall geometry. The solid vertical lines mark the boundaries of each layer, which are colored in different shades of gray and labeled at the top. The dashed horizontal line marks the 2°C thermal safety threshold. The dotted vertical line marks the depth, d^*, at which ΔT is highest for all power levels. 36
2.4 $\Delta T(458)$ in °C over the central 2D cross-section from Fig. 2.1B. Areas where $\Delta T > 2$°C were not assigned a color to visually preserve the temperature resolution. The red dashed line indicates the axis with the tissues' highest ΔT. 37
2.5 2D temperature maps of the CWU thermal prototype and its benchtop COMSOL model for the 500 mW configuration. The bright spot in the lower right corner overlaps with the position of the resistors. (A) Thermal camera image of the prototype placed on the benchtop. (B) An equivalent map produced by the benchtop computational model with $T_{\mathrm{ext}} = 22.9$°C. 40
2.6 Cooling profile of a Ti bar in an open-air benchtop environment. The black dots show the temperature decay measured experimentally, while the red line is an exponential model derived from Eq. (2.6), with the best linear fit, $h = 13$. 41
2.7 The average top surface temperature of the thermal prototype in comparison to the simulated temperature range for different power consumption levels. (A) Actual temperature. (B) The same values expressed as a deviation from the room temperature. The black crosses are experimental temperature measurements, T_{p}, repeated at ∼10 minute intervals. The cyan boxes represent the simulated temperature range $[T_{\mathrm{m}}(P_{\mathrm{b}}^{\mathrm{min}}), T_{\mathrm{m}}(P_{\mathrm{b}}^{\mathrm{max}})]$. The pink stars show the average room temperature, T_{ext}. 42

3.1 Model of the human head, with relevant tissues and implanted components. The dimensions are in mm (cf. Table 3.1 for the thickness of each tissue layer and component). (A) 3D view of the model geometry. (B) Central cross-section of the view in (A). (C) Zoomed-in view of the inset in (B). (D) 3D view of the SU. (E) Central cross-section of the SU. (F) 3D view of the electrode grid. The green and red electrodes indicate the positive and negative stimulating electrodes, respectively. (G) Zoomed-in view of the cross-section of the electrode grid. 51

3.2 Plot of I_{stim}, a biphasic square pulse stimulating current, and I_{RMS}, its corresponding RMS value. T_{p} is the signal's time period and W is the phase width. 56
3.3 (Top) Sketch showing the location of the stimulating electrodes in contact with tissues. The electrodes are represented as light gray boxes with their top and bottom boundaries outlined in red and light blue, respectively. The corresponding boundary conditions are also shown and appropriately color coded. The yellow arrows show hypothetical current paths between the top boundaries of the anode and cathode. (Bottom) Simplified (lumped) circuit model of the above system, where Z_{E} is the electrode impedance, $Z_{\text{C}}(\rho_s)$ is the contact impedance, and Z_{T} is the equivalent impedance of tissues. 59
3.4 The distribution of T (°C) across the central cross-section of the nominal model for an inactive implant ($P_{\text{SU}} = 0$, $V_{\text{stim}} = 0$) calculated using COMSOL-defined *extra fine* mesh size. 63
3.5 The distribution of $\Delta T(P_{\text{SU}})$ across the central cross-section of the model for different P_{SU} levels. The areas where $\Delta T > 1$°C are colored in red (for all other areas $\Delta T \leq 1$°C). The SU's Ti shell is shaded in a striped pattern for visualization purposes. (A) 50 mW (B) 60 mW (C) 70 mW (D) 80 mW. . . . 65
3.6 ΔT(70 mW) in °C across the central (worst-case) cross-section of the model. For a better color resolution, we limited the color to 0°C$\leq \Delta T \leq$ 1°C. (Top) View of the overall 2D cross-section. (Bottom) Zoom-in of the top inset. . . 66
3.7 The spatial distribution of the electric potential (V) across the central cross-section of the model in response to $V_{\text{A}} = V_{\text{stim}}$ and $V_{\text{C}} = -V_{\text{stim}}$ ($V_{\text{stim}} = 1.1$ V). Arrows represent the electric current density, with the length proportional to the current density magnitude. When integrated over the anode or cathode surface, the total current is 2.2 mA (see Section 3.2.2). The SU's Ti shell is shaded in a striped pattern for visualization purposes. 67

4.1 (Top) Overview of the experimental setup.Participants walked on a treadmill while being placed in a 0% weight-support harness to prevent falls. Their ECoG signals were recorded with a bio-amplifier system and their leg trajectories were measured using gyroscopes mounted on the distal femur (not visible) and distal tibia. (Bottom) Treadmill walking speed during the two experimental tasks.In the constant-speed task, the participants alternated between epochs of idling and walking at casual speed. The variable-speed task consisted of walking epochs at three speeds (slow, casual, fast), and the initial and final idling epochs. Each epoch lasted ∼30 s with the overall task duration of ∼5.5 min. 76
4.2 Pipeline of the proposed decoder. Raw ECoG signals are preprocessed and bandpass filtered. The resulting signals input into a logistic regression-based feature extraction algorithm. For the state signal, principal component analysis (PCA) is implemented before the logistic regression. The state and step logistic regression outputs are multiplied to create the extracted feature, f. The final step is a Fokker-Planck-based Bayesian filter, whose input is f and output is the decoded walking steps. 77

4.3 Example of the preprocessing steps for a tibial gyroscope signal. The raw signal was bandpass filtered to retain only frequencies related to the stepping rate. We set to 0 all negative values, thus retaining leg swings only. Then, to compute G_{norm} we normalized each peak (i.e., swing) by dividing its magnitude by its height. Then, we computed G_{step} as a binary signal that is 1 during leg swings (when $G_{\text{norm}} > 0$) and 0 otherwise (when $G_{\text{norm}} < 0$). Similarly, G_{state} is a binary signals that is 0 during idling and 1 during walking. 79
4.4 Plot of the instantaneous power of different frequency bands from multi-channel ECoG signals during an idle-move transition. The instantaneous power signals were obtained by bandpassing raw ECoG data to the specified frequency bands and then squaring it. The bottom red signal is raw gyroscope data from the contralateral tibia. The white and green background represent idle and move states, respectively. 80
4.5 Time series of representative extracted signals during an idle/move transition (move segment is shaded in gray). Gyroscope data is used to determine idle (static signal) and move (changes in signal indicate leg swings) periods. (Left) Plot of signals used to decode the state: two principal components, PC_{state} ($k = 2$), and the state logistic regression feature, p_{state}. (Middle) Plot of signals used to decode steps: hγ power envelopes, P_{step}, and the step logistic regression feature, p_{step}. (Right) Plot of the state and step logistic regression features (p_{state} and p_{step}), and their product, the extracted feature f. 83
4.6 Location of the interhemispheric ECoG grid electrodes, determined by MRI, for SJ1 (A) and SJ2 (B). The approximate location of anatomical features are shown as colored lines. CS: Central Sulcus, PS: Precentral Sulcus, and CgS: Cingulate Sulcus. Green electrodes are located in M1 and pre-motor cortex areas, whereas red electrodes are located outside the motor areas. We only decoded data from the green electrodes. For SJ2, data from electrode 29 (outlined in white) was not available during the constant-speed task. 88
4.7 Representative feature extraction map (SJ1, variable-speed task, run 1) shown as the magnitude of the trained coefficient matrices: pc, c_{step} and c_{state}. Warmer colors indicate electrodes / frequency bands that were most informative for the principal component analysis and/or logistic regressions. White electrodes were excluded in our study, as they fall outside the cortex of interest. 89
4.8 Representative segments of an extracted feature f, decoder output, and ground truth, G_{step} signals. The decoder output is obtain by implementing a Fokker-Planck-based filter on the extracted feature f. The decoder's performance is quantified by comparing the decoder output against G_{step}. These signals are part of the constant-speed task (run 2) for SJ1. 90
4.9 Representative measurement model examples for SJ1 (left) and SJ2 (right) for the variable-speed task (Run 1). The trained parameters that described these models were $\lambda = 0.11$, $f_0 = 0.34$ for SJ1, and $\lambda = 0.12$, $f_0 = 0.35$ for SJ2. 91

LIST OF TABLES

Page

2.1 The average thickness of the relevant tissue layers 23
2.2 The average values of tissues' thermal parameters: thermal conductivity, k, metabolic heat, Q_{m}, and blood perfusion, $\rho_b C_b \omega$ 27
2.3 The nominal parameters, θ_i^0 , and their negatively and positively perturbed values, θ_i^- and θ_i^+, respectively. 30
2.4 The sensitivity coefficients, S_i^- and S_i^+, for the respective perturbation of each parameter, as indicated in Table 2.3. The critical parameters are highlighted in grey. 38

3.1 The average thickness of tissue layers and implantable components. 49
3.2 Thermal properties of the tissues and implanted components 53
3.3 Electrical conductivity of the tissues and components. 54
3.4 Combinations of stimulation parameters that result in the same I_{RMS} and in turn the same heat effect. 57
3.5 The nominal values of the physiological and environmental parameters, θ_i^0 , and their negatively and positively perturbed values, θ_i^- and θ_i^+, respectively. l – thickness (mm), k – thermal conductivity (W/(m K)), Q_{m} – metabolic heat (W/m^3), ω – blood flow rate ((ml/s)/ml), T – temperature (°C), h – heat transfer coefficient (W/(m^2 K)), σ – electrical conductivity (S/m). . . . 62
3.6 The nominal values of parameters, θ_i, and the sensitivity coefficients associated with their positive and negative perturbations, S_i^+ and S_i^-, respectively. The critical parameters are highlighted in grey. l – thickness, k – thermal conductivity, Q_{m} – metabolic heat, ω – blood flow rate, T – temperature, h – heat transfer coefficient, σ – electrical conductivity. 68

4.1 Sensitivity and precision values for every participant's tasks. 90
4.2 Approximate number of clock cycles necessary to implement each decoding operation in a microprocessor for a 50 ms ECoG signal. 92

ACKNOWLEDGMENTS

I would like to thank my Ph.D. advisor, Dr. Zoran Nenadic, for his many lessons and guidance throughout the last 5 years.

Special thanks to my labmates Dr. Jeffrey Lim, Mina Ibrahim, Piyashi Biswas and Shravan Thaploo for their support and encouragement. I am also grateful to Dr. Po T. Wang for his endless knowledge and contributions, and Dr. An H. Do for his insightful advice.

To my parents and my sister, your infinite patience, love and support means everything to me. To Byron, thank you for being my rock and partner on this journey, I am forever grateful to you. To my friends and family, thank you for being my continuous source of motivation and inspiration.

I would like to thank the National Science Foundation (NSF-1646275) and the Balsells Fellowship for funding this work.

VITA

Claudia Serrano Amenos

EDUCATION

Master of Science in Biomedical Engineering **2021**
Unviersity of California, Irvine *Irvine, California*

Bachelor of Science in Biomedical Engineering **2018**
Unviersitat Politecnica de Catalunya *Barcelona, Spain*

RESEARCH EXPERIENCE

Graduate Student Researcher **2018–2023**
University of California, Irvine *Irvine, California*

Student Researcher **2017–2018**
Hospital San Joan de Deu *Barcelona, Spain*

TEACHING EXPERIENCE

Teaching Assistant **2017–2018**
Unviersitat Politecnica de Catalunya *Barcelona, Spain*

REFEREED JOURNAL PUBLICATIONS

Simulation-informed Power Budget Estimate of a Fully Implantable Brain-Computer Interface **2023**
Under Review

Power Budget of a Skull Unit in a Fully-Implantable Brain-Computer Interface: Bio-heat Model **2023**
Under Review

REFEREED CONFERENCE PUBLICATIONS

Thermal Analysis of a Skull Implant in Brain-Computer Interfaces **Jul 2020**
42nd Ann. Int. Conf. IEEE Eng. Med. Bio. Soc.

ABSTRACT OF THE DISSERTATION

Power Optimization for Fully-Implantable Brain-Computer Interfaces

By

Claudia Serrano Amenos

Doctor of Philosophy in Biomedical Engineering

University of California, Irvine, 2023

Professor Zoran Nenadic, Chair

Brain-Computer Interfaces (BCIs) are an emerging approach to restore walking capabilities in people with paraplegia due to spinal cord injury (SCI) or other neurological conditions. BCIs record brain signals in real time to decode users' intentions and use this information to operate external devices, such as orthoses, exoskeletons, or muscle stimulators. BCIs based on invasively recorded brain signals, such as electrocorticograms (ECoG), can achieve a better performance than their non-invasive counterparts. This advantage comes from the fact that ECoG signals have higher spatio-temporal resolution than scalp recorded electroencephalograms (EEG). Moreover, subdurally implanted ECoG electrodes can elicit leg sensation by delivering cortical electrostimulation. Therefore, an ECoG-based BCI can restore both motor and sensory function to those paralyzed due to SCI. These so-called bi-directional BCIs (BD-BCIs) have the potential to be fully implantable, which greatly increases their potential for a widespread adoption.

The main challenge in the development of fully-implantable BD-BCIs is complying with the FDA safety regulations for active implantable devices. These include protection from current leakage, thermal injury, and inflammatory responses, among others. In this work, we assessed the thermal safety of a fully-implantable ECoG-based BD-BCI system using the Finite Element Method (FEM). Specifically, starting from the FDA's thermal safety constraints, we

used bio-heat transfer models implemented in COMSOL to estimate the maximum power consumption (power budget) of the BD-BCI's active components, namely, a chest wall unit (CWU) and a skull unit (SU). We also assessed the robustness of these computational models against the natural variation of physiological and environmental parameters, such as thermal, physiological, and metabolic properties of the tissues. Furthermore, we fabricated a CWU thermal prototype and performed benchtop experiments to validate our modeling approach. Finally, given that the decoder is one of the most "power-hungry" functional modules of the CWU, we developed a novel power-efficient decoding methodology capable of decoding individual steps with excellent accuracy and negligible lag. Specifically, we employed a combination of logistic regressions and the Fokker-Plank equation to design a recursive Bayesian filter that estimates the probability of leg swings from ECoG signals. We validated the performance of this decoder using ECoG signals recorded from motor cortical areas of two human subjects as they performed multiple walking tasks.

Chapter 1

Introduction and Background

1.1 Brain-Computer Interfaces

Brain-Computer Interfaces (BCIs) record electrophysiological signals from the brain and translate them in real-time into control commands for various types of end-effectors, such as computer cursors [197], spellers [30], and robotic prosthesis [199]. BCI systems can be used as rehabilitation tools for individuals with communication and motor impairments. For example, BCIs can restore communication in individuals with locked-in syndrome (LIS) [121] and can restore lost motor function in individuals with stroke, spinal cord injury (SCI), and traumatic brain injury [19]. In the future, BCI systems could potentially extend beyond the treatment of medical conditions to enhance the performance of able-bodied individuals [212, 227].

BCIs for motor restoration work under the principle that neural pathways responsible for impaired motor functions are partially intact. For example, people with paraplegia may retain electrophysiological signals in the central nervous system that correspond with motor intent. Therefore, the goal of BCIs is to bypass the disrupted motor pathways by decoding

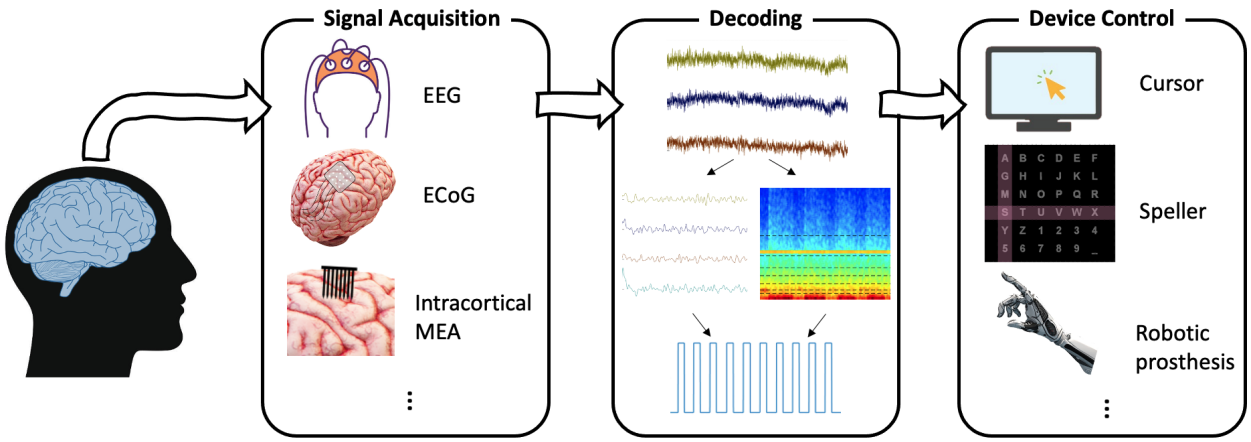


Figure 1.1: Diagram of a typical BCI system. Recorded brain signals are decoded into control commands for an external device. Different recording modalities, signal processing techniques, and external devices are used for different BCI applications.

motor commands directly from electrophysiological brain signals. We know that behavioral tasks, such as physical or imagined movements, cause frequency-domain changes in the sensory and motor cortices, known as neural features. Thus, BCIs record brain signals, extract their neural features using signal processing and statistical techniques and translate them into motor commands.

1.1.1 Signal Acquisition

There are many recording modalities used in BCIs, but they can be classified into two main categories: non-invasive and invasive techniques. Some examples of non-invasive techniques are electroencephalography (EEG) [63, 115], functional magnetic resonance imaging (fMRI) [70, 189], and magnetoencephalography (MEG) [188, 144]. These techniques are safer than invasive approaches given that they do not require surgical implantation. However, many non-invasive modalities, including fMRI and MEG, require the use of very large and expensive non-portable machines. This is an impediment to many BCI applications that require portability, such as motor restoration and rehabilitation. Instead, the most popular non-invasive technique for BCI is EEG, due to its low cost and portability. EEG records

the cumulative electrical activity of large populations of neurons from the scalp [63], see Fig. 1.2. This technique has been extensively used for many BCI applications [58, 164, 101], including motor restoration and rehabilitation [221, 120, 3, 47, 48]. However, EEG has certain limitations that hinder its usability. First of all, typical EEG can only detect brain activity $<$ 50 Hz [163], and thus cannot capture γ activity (40 - 200 Hz), which encodes motor information [140, 123, 207]. Furthermore, EEG has a limited spatial resolution (5-9 cm) [156, 8]. This is inconvenient for motor decoding, given that the motor representation areas in M1 are small and can overlap [177]. Instead, to distinguish between different precise motor movements, a spatial resolution of a few millimeters is needed. Additionally, EEG is highly susceptible to biological and motion artifacts such as eye blinks or electromyographic (EMG) contamination [10, 216].

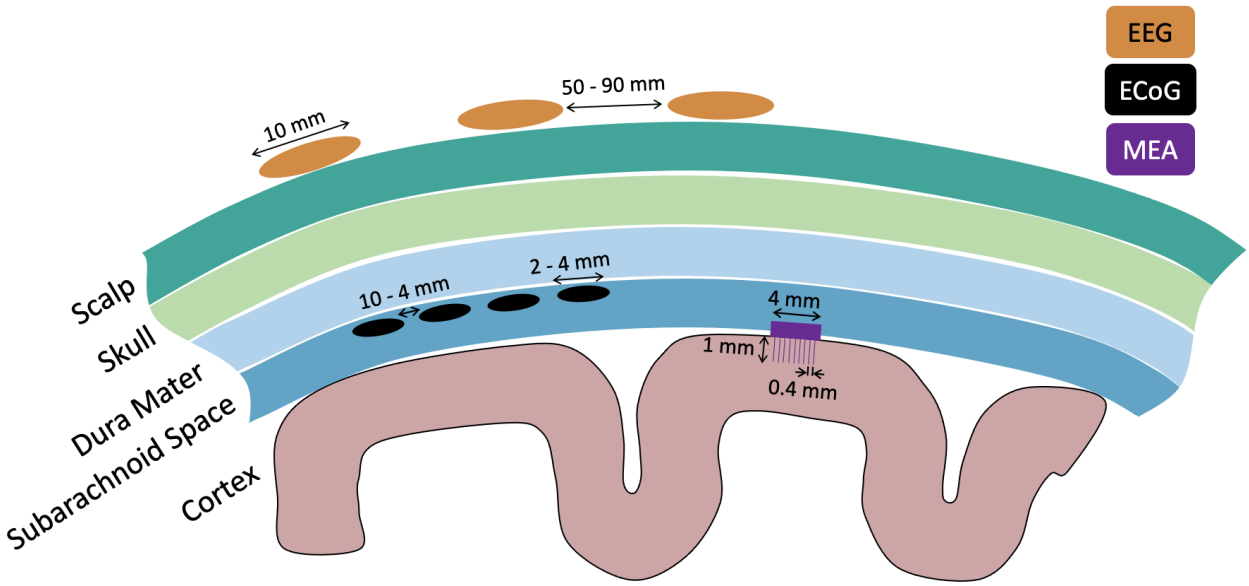


Figure 1.2: Sketch of human head tissues and different non-invasive (EEG) and invasive (ECoG and MEA) recording modalities. The annotated dimension ranges are based on common designs for each technique. The scales of the electrodes and head tissues are altered for illustration purposes.

On the other hand, invasive recording modalities must be surgically implanted. A common example is electrocorticographic (ECoG) electrodes, which are arrays of platinum or stainless steel electrodes embedded in a flexible plastic substrate implanted in the subdural space [122],

see Fig. 1.2. Another common example is intracortical micro-electrode arrays (MEAs), which are arrays of shank-like electrodes that penetrate the cerebral cortex [104], and thus are slightly more invasive than ECoG (Fig. 1.2). ECoG and MEAs can accurately record brain signals up to 250 Hz and 400 Hz, respectively [50]. Thus, these techniques are more adequate for capturing high-*gamma* activity (80 - 200 Hz), which contains critical motor information that can improve the decoding accuracy of BCIs [207]. Furthermore, ECoG has a spatial resolution of 10 mm for standard grids [7] and 3-4 mm for high-density grids [171], while MEAs have an even greater spatial resolution, in the order of μm [15]. Due to their higher spectral and spatial resolution, these invasive techniques have been used in BCIs for motor restoration and rehabilitation [176, 13, 85, 24]. However, although long-term implantation and decoding from MEAs has been safely accomplished [187], studies have shown that the signal quality of MEAs degrades over time [203]. This is likely due to foreign-body immune response to the electrodes, which results in glial scarring and eventual signal degradation [18, 61]. Therefore, ECoG is a more suitable recording technique for BCIs that aspire to be life-long solutions, and thus require long-term implantation.

1.1.2 Neural Signals

To translate brain signals into control commands, BCIs must record and analyze certain neural features that are relevant to the system's application. A common neural feature used by BCIs is visually evoked potentials (VEPs), which are neural signals that reflect the visual information-processing mechanism in the occipital cortex [211]. For example, BCIs that aim to restore communication for subjects with LIS can provide the user with multiple images (e.g., different types of foods) on a screen, flickering at different frequencies, and then instruct the user to focus their attention on the desired image, while simultaneously recording their brain signals using EEG. These recorded signals, known as steady-state VEPs (SSVEPs), will oscillate at the same frequency as the image that the user was focused on [229]. Another

common neural feature is event-related potentials (ERP), which are electrical potentials generated by the brain that are time-locked to a specific internal or external event, such as stimuli or decisions [131]. For example, the P300 is an ERP in the parietal lobe that is elicited during an oddball paradigm, ∼300 ms after a subject is presented with a rare/unexpected stimulus [168, 59]. This is particularly useful for BCI spellers, where the user is presented with a matrix of letters where the rows and columns are randomly flashed. When the row/column of the letter that the user is focused on flashes, a P300 response can be detected using EEG [110].

For motor restoration purposes, the most relevant neural features are sensorimotor rhythms. They are oscillations in the electric or magnetic field recorded over the sensory and motor cortices that are defined by their frequency, bandwidth, and amplitude [198]. For example, certain frequency bands like the μ (8–13 Hz) and β (14–40 Hz) frequencies experience a power attenuation during physical motor execution and mental motor imagery [152], see Fig. 1.3. This phenomenon is known as event-related desynchronization (ERD) [36, 165]. Conversely, the γ frequency band (40–200 Hz) experiences a power increase during movement or imaginary movement (Fig. 1.3), which is known as an event-related synchronization (ERS) [35, 165]. Although individuals with SCI can lose motor function below the level of injury, usually their sensorimotor rhythms are still intact. Thus, BCIs can use EEG or ECoG to record these neural features, decode motor intentions, and restore motor functions.

1.1.3 BCI Decoders for Motor Applications

One of the key components of BCIs is the decoder, which is an algorithm that translates neural signals into control commands. This section describes different types of decoders that have been used for EEG, ECoG, and MEA-based motor BCIs. Depending on the algorithm's structure, decoders can be grouped into three different categories (Fig. 1.4). Below we explain

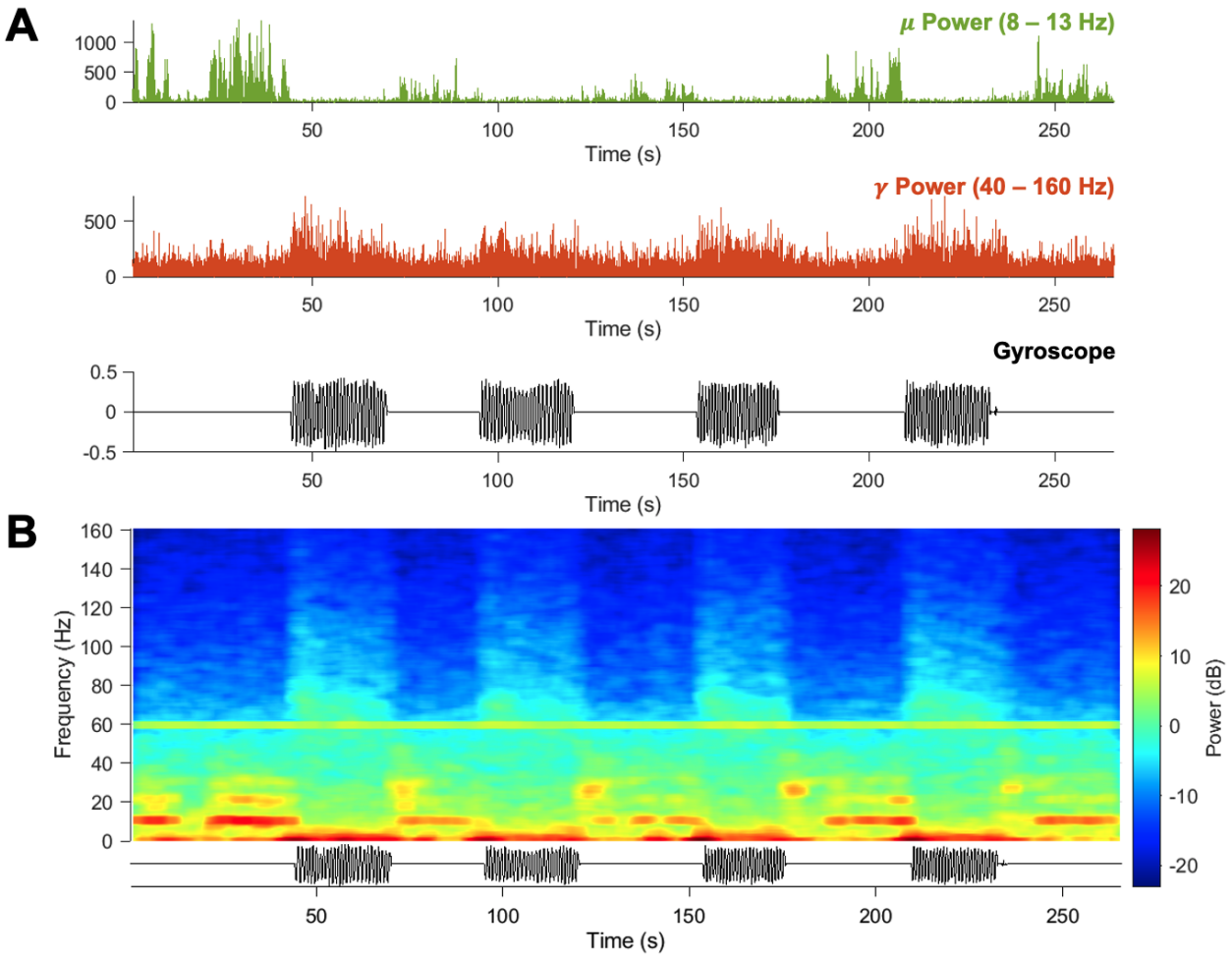


Figure 1.3: Example of ERS and ERD from ECoG signals during elbow movement intervals. (A) Time series of the μ (green) and γ (orange) powers, as well as gyroscope (black). During motor movement (gyroscope $\neq 0$), μ-power decreases (ERD), while γ-power increases (ERS). (B) Spectrogram of ECoG signals up to 160 Hz and gyroscope signal. ERD is visible at $\sim$ 10–30 Hz, and ERS is apparent at $<$10 Hz and $>$40 Hz.

and discuss examples of each category separately.

Classification and regression

The first step in classification and regression algorithms is to extract spectral neural features (i.e., sensorimotor rhythms) from raw neural signals. Examples of techniques used to extract these spectral features include bandpass filters [32, 42], non-parametric methods such as Fourier transform [191, 77], multitaper methods [100], parametric techniques such

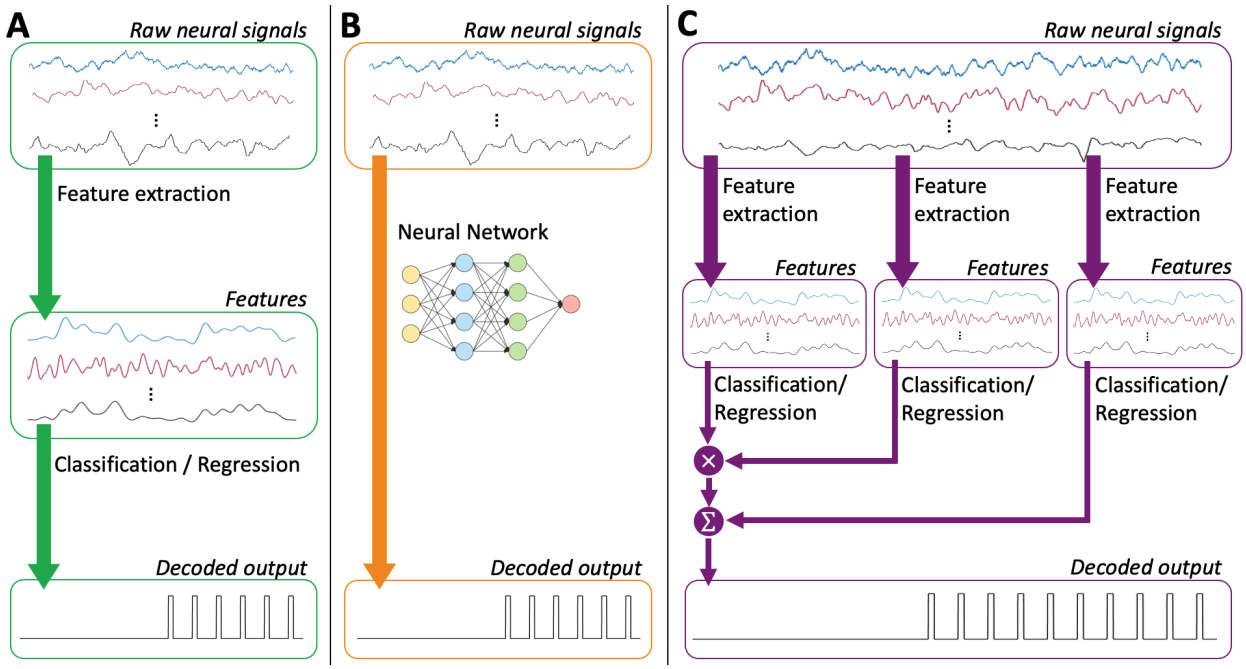


Figure 1.4: Types of motor decoder architectures. (A) Classical approach, where first features are extracted from the raw neural signals and then the decoder uses a classifier/regression to generate the decoded output. (B) Deep learning approach where both feature extraction and classification/regression are learned together. (C) Hybrid decoder where multiple classification/regression decoders are implemented simultaneously and their individual outputs are combined to generate one final decoded output.

as autoregressive model estimation [214, 93], and maximum entropy approach [26].

BCI decoders usually benefit from using spatial filters, which combine multiple original time series to create new signals with higher signal-to-noise (SNR) ratio than that of the individual time series. Data-independent spacial filters are based only on the location and physical considerations of the recorded signals. Common examples are the Laplacian filter [141] and the common average reference (CAR) [111]. Conversely, other spacial filters are data-driven, and common examples include principal component analysis (PCA) [22] and independent component analysis (ICA) [98].

Classification algorithms use neural features to forecast classes, such as move or idle, right or left, upwards or downwards. There are many classification algorithms used in BCI decoders, and here we discuss two main types: linear classifiers and nonlinear Bayesian classifiers.

Linear classifiers are discriminant algorithms that use linear functions to distinguish classes. Two commonly used linear classifiers in BCIs are linear discriminant analysis (LDA) and support vector machines (SVM). For example, Jiang et al. used LDA to decode hand flexion and extension from ECoG data [94], and Blankertz et al. used SVM to decode finger movements for keyboard typing from EEG data [20]. Opposite to linear classifiers, nonlinear Bayesian classifiers use nonlinear decision boundaries. The most common examples are Bayesian filters and hidden Markov models (HMM). For example, Wang et al. used a Bayesian filter to decode walking states from ECoG data [208], and Obermaier et al. used HMMs to decode left and right-hand movements from EEG data [157].

Regression algorithms use neural features to determine continuous parameters such as position, velocity, and acceleration. These algorithms are less commonly used in BCIs than classifiers. Typically, regression provide very precise information and, thus, require input data to be recorded invasively (e.g., ECoG or MEA), since signals recorded closer to the source (neurons) encode more information. Linear regression is the most common type of regression. For example, Nakanishi et al. used a multilinear regression to decode 3D hand positions from ECoG data during reaching experiments [150]. Other linear regression algorithms are the Wiener filter and the Kalman filter. For example, Sanchez et al. used a Wiener filter to decode cursor trajectories from ECoG recordings [173], and Pistohl et al. used a Kalman filter to decode 2D arm trajectories from ECoG signals [166].

Neural networks can be applied to both classification and regression problems. These algorithms are highly versatile and can handle complex, non-stationary neural data [200]. While shallow and simple neural network algorithms use neural features as input data, more complex algorithms, known as deep neural networks, use raw brain data as input, and can extract features within the neural network. Deep neural networks are discussed below in further detail.

Deep Learning

Deep learning is a type of machine learning algorithm in which the neural features and the classifier/regression are jointly learned directly from raw data [129]. A very common example is convolutional neural networks (CNN), which are feedforward neural networks with at least one convolutional layer, which maps its inputs to an output through a convolution operator. This layer is usually followed by nonlinearities and a pooling layer. For example, Zhang et al. used a CNN to decode left and right-hand motor imagery tasks from EEG data [228], and Choi et al. used a CNN to estimate bimanual movements from ECoG data [33].

Hybrid Decoders

Hybrid decoders combine multiple classification and/or regression algorithms to improve the decoding performance. Researchers use different strategies to create hybrid decoders. For instance, boosting consists of using multiple classifiers/regressions in cascade, where each algorithm focuses on the errors committed by the previous ones [86]. Another strategy is voting, where algorithms try to classify or decode the same variable, and the overall decoder's output is based on the most common output from all the algorithms [170]. Finally, hierarchical decoders stack multiple algorithms, where each algorithm decodes a different variable. For example, Yanagisawa et al. developed an ECoG hierarchical decoder, where the first SVM algorithm classified the movement state (rest and movement), and the second SVM algorithm predicted the type of hand movement [223]. Another hierarchical example is an ECoG decoder developed by Hotson et al., where a LDA algorithm distinguished between hand movement and rest, and a second LDA algorithm determined which of the five fingers was moving [88].

1.1.4 Bi-directional BCIs

SCI causes disruption of nerve axons running through spinal cord tracts, which leads to loss of both motor and sensory function below the level of injury [14]. Given that sensory information is key for proper motor function [95, 147, 52], to fully restore able-bodied functionality after SCI, BCIs will need to integrate both motor and sensory modalities [89]. Furthermore, preliminary studies have shown that sensory feedback improves BCI performance [64].

Artificial sensation can be evoked by delivering electrostimulation directly to the sensory cortex through ECoG electrodes [96, 84, 117] and MEAs [5, 62]. The stimulation signal usually consists of a bipolar pulse train, with an electric current in the order of mA [105]. These forms of stimulation can produce naturalistic sensory responses such as brushing or tapping sensations, and even proprioceptive movement sensations [5].

BCI systems that can deliver electrostimulation are referred to as bidirectional BCIs (BD-BCIs). These systems combine the feed-forward path that decodes neural signals and controls and an end-effector with the feedback path that delivers electrostimulation directly to the cortex (see Fig. 1.5). Moreover, these systems have the potential to be fully implantable, which greatly increases their practicality. Although a clinically deployable BD-BCI has yet to be developed, researchers have already introduced preliminary BD-BCI designs [172, 21].

1.2 Our Envisioned BD-BCI

During the last few years, our group has been working on developing a fully implantable BD-BCI to restore walking and leg sensation in subjects with paraplegia. The envisioned system (Fig. 1.6) consists of an ECoG grid implanted over the leg motor cortex to record brain activity. This electrode grid is connected to a skull unit (SU) that amplifies, serializes and A/D converts the recorded data [133, 99, 135]. Then, a tunneling cable sends this

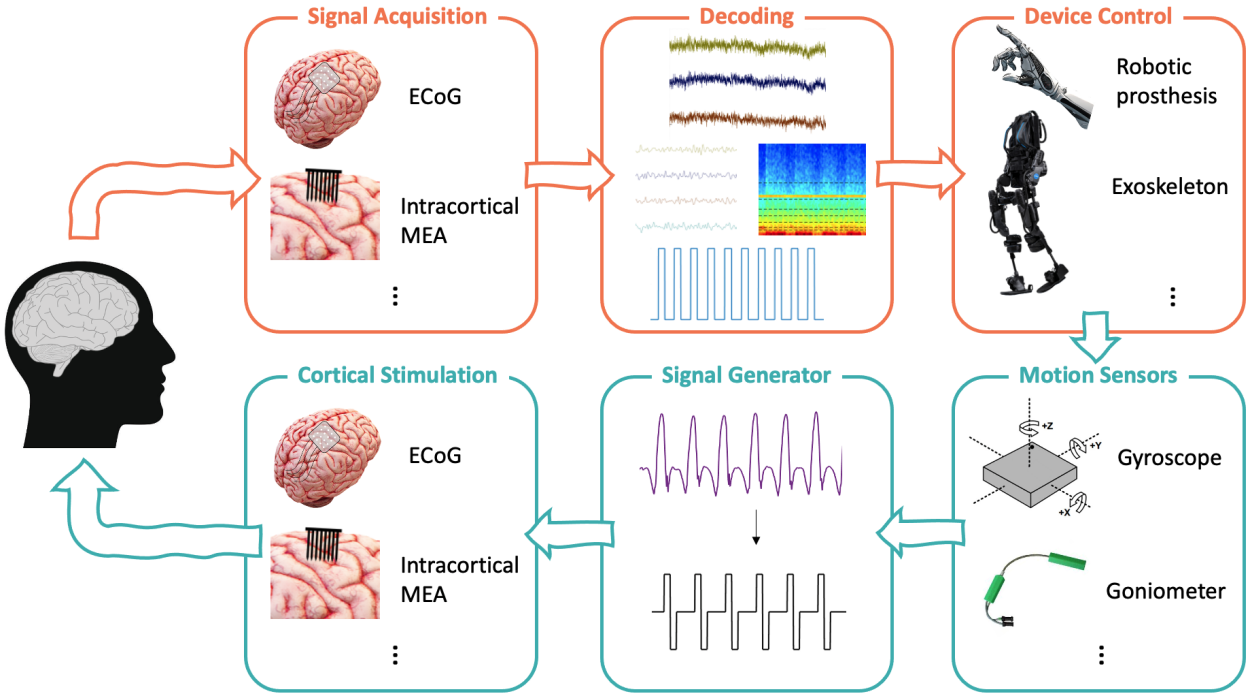


Figure 1.5: Diagram of a BD-BCI paradigm. Recorded brain signals are decoded into control commands for an end-effector. Sensors in the end-effector capture motion signals, which, in turn, are converted into a stimulation signal that is delivered to the sensory cortex to elicit artificial sensation.

information to a Chest Wall Unit (CWU), which, in turn, analyzes and decodes the signals into walking commands. Then, the CWU wirelessly transmits the walking commands to an exoskeleton [118]. At the same time, sensors in the exoskeleton capture motion information and send it back to the CWU. There, the motion information is translated into stimulation patterns, which are sent back to the SU through the tunneling cable. In the SU, the stimulation signal is D/A reversed and sent to the ECoG grid in the sensory cortex, where cortical stimulation to elicit leg sensation is delivered.

Our end goal is to implant this BD-BCI in individuals with paraplegia to restore their walking and leg sensation capabilities. However, multiple challenges must be addressed before we can surgically implant this system in humans. First, we must demonstrate that a system can perform all the envisioned BD-BCI functionalities properly, including ECoG data acquisition, neural data decoding, wireless communication, and generation of electrostimulation. So

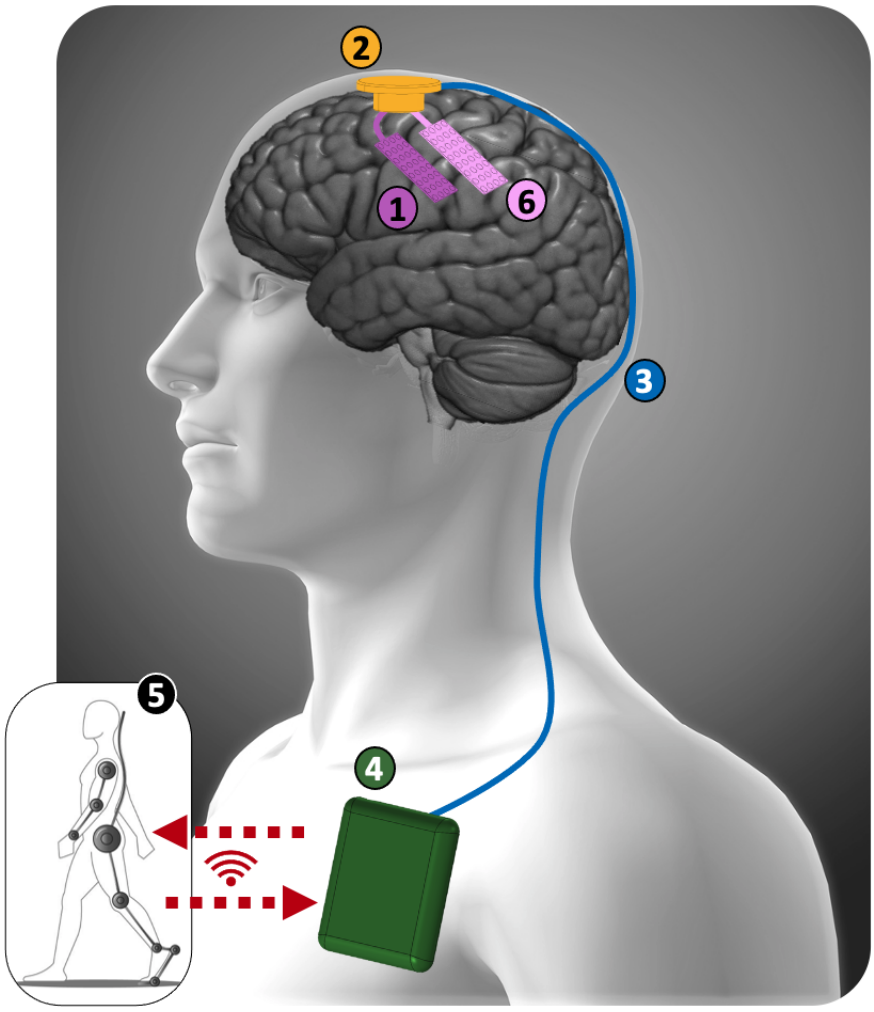


Figure 1.6: Envisioned fully-implantable BD-BCI system for restoration of walking and leg sensation. The system comprises several implantable subsystems. A skull unit (SU) (2) is implanted on the exterior aspect of the skull and is connected to the motor (1) and sensory (6) ECoG grids. A chest wall unit (CWU) (4) is implanted subcutaneously in the pectoral area. The SU and CWU are connected by a subcutaneous tunneling cable (3), similar to the current deep brain stimulator (DBS) design. The system communicates wirelessly with an external exoskeleton (5).

far, our group has developed a benchtop prototype of the BD-BCI system using off-the-shelf components [205, 192]. To ensure that this prototype can perform all the envisioned BD-BCI functionalities, we tested its performance with individuals undergoing Phase II epilepsy monitoring in the hospital [124]. Using the prototype, these individuals controlled an external walking exoskeleton through motor-modulated ECoG signals, which we recorded from grids implanted over their motor and sensory cortices for surgical evaluation purposes.

At the same time, when the exoskeleton's leg (contralateral to the ECoG grid) stepped, we delivered electrostimulation to the users' sensory cortex. Overall, the subjects were able to wirelessly control a walking exoskeleton using motor-modulated brain signals, while simultaneously receiving cortical stimulation that elicited artificial sensation. As new and improved functionalities are added to the prototype, we will continue to test its functionality with similar hospital experiments.

One of the most important functionalities of our BD-BCI design is the decoder. An adequate decoder should be reliable and suitable for our BCI application. Specifically, it should decode commands that are appropriate to control our walking exoskeleton. Given that our exoskeleton requires manual activation for individual steps, the decoder's optimal output is individually decoded steps. Furthermore, a reliable decoder should correctly identify the user's motor intentions (minimize false detections and missed detections), and have a response time suitable for real-time implementation ($<$ 0.1–0.2 s) [113]. The decoder implemented in the current BD-BCI benchtop prototype does not decode individual steps, instead, it decodes walking states (idling/walking). Thus, when the decoder identifies an idle state, the exoskeleton remains inactive, and conversely, when the decoder identifies a walking state, we continuously activate the exoskeleton to trigger consecutive walking steps. This way, the user can prompt the exoskeleton to walk, but has no control over when individual steps are triggered, and, hence, cannot regulate the walking speed.

The current decoder uses information from the α and β bands (8–35 Hz), as well as the high-γ band (80–160 Hz). The algorithm uses classwise principal component analysis (CPCA) for dimensionality reduction, and linear discriminant analysis (LDA) to further enhance the class separability. Additionally, the decoder uses Bayes' rule to calculate the posterior probabilities of each state (idle/walk). Overall, this decoder can predict walking states in real-time with an average accuracy of 99.8% and latency of 250 ms [208]. More recently, our team developed a decoder that can detect the stepping rate during walking [208]. Although

the decoded speed must be transformed into individual steps to trigger the exoskeleton, it is still a more appropriate output than general walking states. Specifically, this new decoder integrates, in a hierarchical fashion, the previous state decoder with a step rate decoder, which includes a matched filter and a Bayesian filter. Overall, this decoder has an average Pearson correlation coefficient of 0.93 and root mean square error (RMSE) of 0.06. The main drawbacks of this decoder are its high computational complexity, due to the use of two separate Fourier Transforms, and its latency of $\sim$ 5.5 s. These drawbacks hinder its real-time implementation.

Another hurdle we must address before developing a fully-implantable BD-BCI is artifact suppression [124]. When recording and stimulating simultaneously with ECoG grids on the cerebral cortex, strong electrical artifacts propagate from the stimulation site to the recording site. The voltages from these artifacts can reach or exceed the nominal supply voltage of the system's analog front-end, which causes a saturation of the recording amplifiers, thereby leading to a permanent loss of data. To reduce the artifact on the front-end amplifiers, we implemented a technique called dipole cancellation. Specifically, we applied auxiliary stimulation between the recording and stimulation sites. This secondary stimulation was delivered simultaneously, and in opposite polarity to the primary stimulation, but with a fraction of the primary stimulation amplitude. However, even after using dipole cancellation, residual artifacts still persisted in the back-end, so we had to further suppress the artifacts using software-based methods. To do so, we developed a technique based on pre-whitening and null projection that efficiently separates the stimulation artifact from true neural signals. When combining both artifact suppression techniques, we predict that the BD-BCI system will allow to simultaneously record and stimulate on the cerebral cortex.

The last hurdle that must be considered when designing a fully-implantable BD-BCI are the Food and Drug Administration (FDA) regulations that apply to our device. Our envisioned system includes both inactive implantable devices, such as the tunneling cable and the ECoG

recording grid, and active implantable devices, like the SU, CWU and ECoG stimulating grid. For example, the FDA requirements for ECoG electrodes include biocompatibility, sterility and electrical safety, among others [65]. However, given the risks associated with electrically-powered devices, the FDA requirements for active implantable devices are more stringent. The next section discusses these type of devices and the applicable FDA regulations.

1.3 Active Implants

Recent technological advancements have led to significant improvements in implantable medical technology and have spurred the development of novel active implantable devices. These systems are crucial in tackling medical conditions for which pharmacological or surgical approaches are deemed inadequate. Examples of active implantable devices include next-generation pacemakers [6], which send electrical pulses to help the heart beat at a normal rate and rhythm, and implantable cardioverter-defibrillators [46], which deliver energy shocks to restore abnormal heartbeats. Another example is vagus nerve stimulators [69], which are used to stimulate the vagus nerve with electrical impulses to treat conditions such as epilepsy, depression, and stroke. A specific subset of these active devices are those implanted in the head, which are typically equipped with stimulation and/or recording capabilities. The earliest successful examples of these head devices are cochlear implants, which can restore hearing to those with severe or profound hearing loss by processing sound signals and stimulating the auditory nerve accordingly [40]. Other examples include deep brain stimulators (DBS) to treat motor disorders such as Parkinson's disease, essential tremor, and dystonia by delivering electrical impulses to the brain [130]. A more recent example is the development of a responsive neurostimulator (RNS) [148], which monitors brain activity and delivers electrical stimulation to disrupt an impending seizure.

Active, electrically-powered implants pose significant safety risks for the human body, includ-

ing current leakage and thermal injury. Accordingly, the FDA imposes certain regulations to maximize the safety of these devices. Specifically, an FDA-recognized standard for active implants is ISO 14708-1, which determines the general safety requirements for these devices. For example, to ensure protection from unintentional biological effects, an implant must be biocompatible, properly sterilized, and free of surface features such as sharp corners or edges that could cause excessive reaction or inflammation. To provide protection from electricity, the ISO standard specifies that active devices must be electrically neutral, i.e., the direct current density at the surface of any conductive surfaces or electrodes must be $\leq 0.75\ \mu\text{A/mm}^2$. Additionally, to guarantee protection from heat damage, the implant's surface temperature must not be greater than 2°C above the normal surrounding body temperature. Other implant safety requirements include the ability to withstand changes in environmental conditions such as minor mechanical shocks that might occur during the implantation procedure, and changes in pressure and temperature that can occur during transit or normal usage conditions.

Implantable neurostimulators (INS) are active implants intended for electrical stimulation of the central or peripheral nervous system. Given that these devices are usually implanted near the brain (which is highly sensitive to heat [71]), the FDA has additional requirements for INS. In this case, the recognized FDA standard is the ISO 14708-3. When compared to ISO 14708-1, the standard pertaining to INS defines more stringent thermal safety requirements. Namely, the thermal requirements for INS are either the temperature of the implant's outer surface cannot be greater than 39°C, or no tissue can receive a thermal does greater than the established CEM43 dose thresholds, where the CEM43 is defined as:

$$\text{CEM43} = \sum_{i=1}^{n} t_i \times R^{43-T_i} \tag{1.1}$$

where t_i is the i-th time interval in minutes, T_i is the average temperature of the tissue in °C during the interval t_i, R is 0.25 for $T < 43$°C and 0.5 for $T \geq 43$°C, and n is the number of samples taken during the heating duration. Note that this equation only applies for $T > 39$°C.

1.3.1 Thermal Safety

Heat can be used in beneficial ways to aid the human body. For example, slight thermotherapy (1 or 2°C increase) can have beneficial effects on injured and aching muscles and joints when used for short periods of time (tens of minutes) [213]. Moreover, some current medical practices use high temperatures, which can cause cell and tissue damage, to treat certain medical conditions. For example, certain cancer treatments use a hyperthermia of 39–45°C for varying lengths of time to target and kill localized cancerous cells [17]. Another common practice is ablation, which consists on using very high temperatures (50–100°C) for very short periods of time (a few seconds) to remove or destroy tissues. For example, thermal ablation is commonly used to destroy cancerous tissues [154], to kill arrythmogenic tissue in the heart[143], and to remove epileptogenic foci in the brain [73]. However, besides these controlled medical practices, exposure to high temperatures poses significant risks, such as burns. For this reason, it is important to consider the thermal risks associated with active implants.

Excessive heat dissipation from an active implant can lead to irreversible damage of the surrounding cells and tissues, including necrosis [45]. Consequently, the FDA imposes stringent limitations on the thermal impact of active implants. The thermal behavior of active implants depends on several factors, including the power dissipated by the electronics (e.g., microchips, PCB, telemetry coil, and stimulating electrodes) [116], the shape, size, and materials of the device, and the implantation site. For fully-implantable BCI systems, it is

important to consider their power dissipation, since BCIs use significantly more power than other active implants [220]. For example, the power consumption of implantable pulse generators (IPGs) ranges between 200 and 1600 μW [38], and the power consumption of active head implants ranges from 40 μW [9] to 3 mW [136]. These power consumption levels are one to two orders of magnitude smaller than that might be needed to power a BCI system [192].

The overall power consumption of BCIs is the sum of the power consumed by each system component [56]. On one hand, amplifiers, A/D converters, and serializers use power to record neural signals. The power consumption of these components depends on the number of channels recorded and the sampling frequency. Next, the decoder uses power to translate neural signals into control commands. The decoder's power usage is determined by the algorithm's computational complexity and its refresh rate. Furthermore, telemetry uses power to wirelessly communicate with external devices. The power consumption of telemetry is dependent on the transmission frequency and data volume. Finally, in the case of BD-BCIs, power is also needed to generate stimulation signals for cortical stimulation. The power consumption due to cortical stimulation is dependent on the stimulation parameters, such as current amplitude, pulse length, and frequency.

Thermal safety, and, specifically, the FDA thermal safety requirements, must be considered during the design of a BCI system. An important design step is to determine a thermally safe power budget for the system. Numerical methods are often used to simulate the thermal behavior of active implants, and, thus, predict their power budget. These thermal simulations require an anatomically correct human body model, the thermal properties of the biological tissues, and the mathematical equations that describe bio-heat transfer. Nowadays, there are many available commercial software for numerical thermal simulations. For example, COMSOL Multiphysics (COMSOL Inc., Stockholm, Sweden) is a finite-element analysis, solver and simulation software that researchers often use to model the thermal behavior of medical implants [54, 55, 103, 160]. Note, however, that thermal simulations are only

an initial step to estimate a thermally safe power budget for BCIs. To ultimately validate a thermally safe operation of these implants, *in vivo* testing, such as animal studies, is necessary.

1.4 Significance

After building a BD-BCI benchtop prototype, our research groups is currently working on designing implantable versions of the CWU and SU prototypes. An important design constraint for these prototypes is their power consumption, which affects the system's thermal safety. Consequently, in this dissertation, we aim to study and optimize the power consumption of a fully-implantable BD-BCI. To that end, we first estimated the power budgets of the CWU and SU that guarantee thermal safety. Specifically, we used numerical thermal models of the CWU and SU to predict the power consumption levels that comply with the FDA thermal safety requirements. Understanding the thermal impact of fully-implantable BCI systems remains an underresearched topic [220]. In this work, we consider the thermal behavior of an implantable BCI and provide specific constraints for its design.

With the design of the implantable version of the BD-BCI prototype, comes the opportunity of improving certain components of the system. However, when doing so, we must consider how any modifications will affect the BCI's power consumption, which ia limited by the estimated power budget. One of the most crucial and power-hungry operations of the system is the decoder. The limitations of the existing decoder hinder the system's ability to restore natural walking capabilities. Moreover, the existing decoder was originally EEG-based and, thus, does not fully exploit the higher frequencies present in ECoG recordings. In this work, we propose a novel power-efficient decoding paradigm for an ECoG-based BD-BCI. By exploiting frequencies > 40 Hz, this new algorithm can decode individual steps, which enables a more natural walking pattern compared to the current decoder. Additionally,

this algorithm's low computational complexity lends a power-efficient implementation of the decoder that is suitable for real-time deployment. Overall, the the proposed decoder improves upon the existing one by enabling a more natural walking pattern, while being mindful of the power consumption. Thus, the proposed decoder optimizes the system's power usage by enhancing the performance of the system without significantly increasing its power consumption.

Chapter 2

Power Budget of the Chest Wall Unit

2.1 Motivation

Addressing the thermal impact of implantable BCIs remains an underresearched topic. This is an interesting problem to address, given that BCIs consume significantly more power than other existing active implants [220]. In our envisioned BD-BCI system, the CWU processes motor and sensory data, and communicates with the other BCI components; thus, it is the most "power-hungry" component of the system. In this chapter, we propose to use computational models to estimate the CWU's maximum power consumption that guarantees its thermally safe operation.

While previous studies have used computational models to analyze the thermal impact of active implants, to the best of our knowledge, there are no studies on the long-term thermal impact of CWU-like implantable devices. Researchers have used numerical models to simulate the thermal behavior of pacemakers [29] and deep brain stimulators [146, 219] under transient overheating conditions like MRI scanning. Others have used simulations to analyze the thermal effects of specific operations like biotelemetry for head and chest implants [102],

deep neural implants [151] and cortical implants [90]. On the other hand, the studies that have modeled the long-term thermal effects of active devices have mainly focused on head implants. For example, researchers have used software like COMSOL to study the thermal impact of active intracortical microelectrode arrays [103], deep brain stimulator leads [54], retinal implants [160], and a BCI skull implant [181].

Motivated by this knowledge gap, we sought to evaluate the thermal impact of a subcutaneously implanted CWU on adjacent pectoral area tissues. To this end, we used the Finite Element Method (FEM) implemented in COMSOL to simulate the temperature of nearby tissues in response to various CWU power consumption levels. We refer to this model as the bio-heat model. Furthermore, we performed a sensitivity analysis to assess the robustness of this bio-heat model against the natural variations of the physiological and environmental parameters. This analysis also yielded the prediction of a thermally safe CWU power budget range. Our ultimate goal is to verify these predictions *in vivo* and will be pursued in our future studies. In the interim, to validate our modeling approach we performed benchtop experiments. Specifically, we built a thermal prototype of the CWU and measured its temperature under different power consumption levels. We then designed a COMSOL model of the thermal prototype (benchtop model), simulated its thermal behavior, and compared these results to those obtained experimentally.

2.2 Methods

In this section, we first present the details of our computational bio-heat model, including its geometry and mathematical description. We also present a sensitivity analysis of the bio-heat model and a benchtop validation of our computational approach.

2.2.1 Bio-heat Model

Geometry

The simulated geometry represents a rectangular region (150 × 150 × 72 mm) of the thoracic cavity (see Fig. 2.1). The skin was assumed to be in direct contact with the air. We further assumed that the CWU is placed below the clavicle (pre-pectoral implantation), under the skin and fat tissues, but above the pectoral muscle, similar to implantable pulse generators (IPGs) for pacemakers [78] and DBS [175]. This model also included the ribs, surrounded by intercostal muscle, and lung tissue. Each tissue's thickness was taken from literature with specific values listed in Table 2.1.

Table 2.1: The average thickness of the relevant tissue layers

Tissue	Thickness, l (mm)	Reference
Skin	2.5	[114]
Fat	4.7	[194]
Muscle	8.4	[25]
Ribs	6.0	[145]

The CWU was modeled as a rectangular prism (59 × 50 × 12 mm) made out of a 1 mm-thick titanium (Ti) shell. We envision the CWU to contain a battery and an electronics layer consisting of a printed circuit board (PCB) with the necessary electronic components. We modeled the battery and electronics as adjacent 8 mm-thick blocks of equal size, surrounded by 1 mm air gap on top and bottom. The overall volume of these layers is comparable to the interior volumes of commonly used IPGs [175, 183].

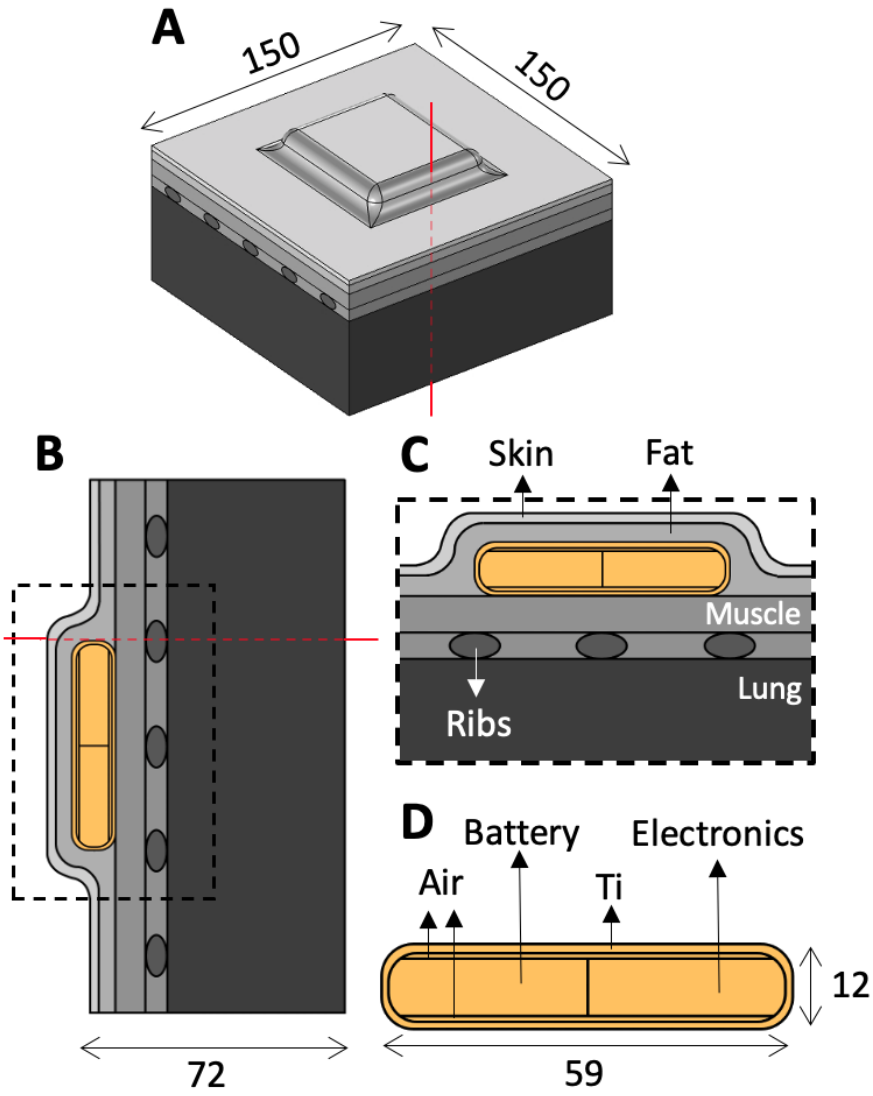


Figure 2.1: Geometric model of the thoracic area and CWU from different views, dimensions in mm. (A) 3D view. The red line indicates the axis where the thermal impact due to the CWU is highest, see Section 2.3.1 for details. (B) Central cross-section of the volume in (A). (C) A zoomed-in view of the inset in (B). (D) Different layers of the CWU.

Bio-heat equation

Heat transfer through biological tissues is typically described by Penne's bio-heat equation [162]:

$$\rho\, C \frac{\partial T}{\partial t} = k\nabla^2 T - \rho_\mathrm{b} C_\mathrm{b}\, \omega (T - T_\mathrm{b}) + Q_\mathrm{m} + Q_\mathrm{ext} \tag{2.1}$$

where ρ (kg/m^3) and C (J/(kg K)) are the tissue's mass density and specific heat capacity, respectively, and T (K) is the temperature at a position (x, y, z) and time t. The first term on the right-hand side is the heat conduction, where k (W/(m K)) is the tissue's thermal conductivity. The second term models the effect of blood perfusion, where ω ((ml/s)/ml) is the volumetric flow rate of the perfusing blood per unit volume and the subscript, b, refers to arterial blood. Finally, the term Q_{m} (W/m^3) is the metabolic heat produced by the tissue, and Q_{ext} (W/m^3) is the heat produced by external sources (e.g., the CWU). Note that $Q_{\mathrm{ext}} = 0$ for all layers except for the electronics layer. It is defined as $Q_{\mathrm{ext}} = P_{\mathrm{CWU}}/V_{\mathrm{elec}}$, where P_{CWU} (W) is the CWU's power consumption and V_{elec} (m^3) is the volume of the electronics layer. The software applied the partial differential equation (PDE) given by Eq. (2.1) to all tissue layers and CWU components, setting to 0 those terms that do not apply and enforcing temperature continuity at the layer interfaces.

The thermal parameters for each tissue layer are given in Table 2.2. The tissue's thermal conductivity can vary by as much as 50%, therefore we took the average values as reported in [51]. Similarly, we computed the tissues' metabolic heat as the average of the values found in [72] and [215]. Since the tissues' blood perfusion significantly depends on physical activity, we used the values corresponding to light exercise or slow walking (1 mph, 80 bpm). Specifically, the fat and ribs' blood perfusion values were estimated from [82] and [81], respectively. For the muscle's blood perfusion, we first estimated the oxygen consumption corresponding to light exercise (0.4 L/min) [222], and then used this information to estimate the blood perfusion from [74], which provides a link between oxygen consumption and blood perfusion. Likewise, for the lungs' blood perfusion, we first estimated the mean pulmonary artery pressure associated with light exercise (17 mmHg) [109], and then used this value to estimate blood perfusion from [4], which gives the relationship between blood perfusion and pulmonary artery pressure. Finally, we estimated that during light exercise the skin's blood perfusion increases 9% with respect to resting state [119], and we computed the blood perfusion at rest as the average of the values found in [119, 76, 11, 137, 34, 218, 142].

The thermal conductivities of the Ti shell and air were 19 W/(m K) [167] and 0.03 W/(m K) [12], respectively. Due to its internal multi-layer structure, the battery has a highly anisotropic thermal conductivity, with $k_{xy} = 15$ and $k_z = 1$ (W/(m K)) [75]. For the electronics layer, we assumed that its thermal properties are similar to those of the PCB. Similar to the battery, the PCB's thermal conductivity is also anisotropic and depends on the number of layers. For a six-layer PCB, as used in our preliminary benchtop CWU prototype [205], we estimated the thermal conductivity as $k_{xy} = 28.15$ and $k_z = 0.31$ (W/(m K)), based on formulas provided in [155].

We applied the following boundary conditions to the boundary value problem (2.1). Consistent with [103] and [160], we assumed that heat transfer occurred through free convection at the skin-air interface:

$$\mathbf{n} \cdot (k \nabla T) = h(T_{ext} - T) \tag{2.2}$$

where $\mathbf{n}$ is the outward normal vector, h (W/m^2 K) is the convection heat transfer coefficient and T_{ext} (K) is the room temperature. For this model, we used $h = 5$ W/(m^3 K), which corresponds to free airflow in the environment [108], and $T_{ext} = 20°$C. Consistent with other studies, we omitted the effect of radiation from the skin surface to the outside air [103]. For the innermost boundary, we assumed the temperature to be equal to the body core temperature [103, 54], with $T = 37°$C [41]. Finally, we assumed that there was no heat transfer across the lateral boundary:

$$\mathbf{n} \cdot (k \nabla T) = 0 \tag{2.3}$$

This assumption is justified given the relatively large distance between the lateral boundary and the CWU heat source. Therefore, the temperature gradients at the lateral boundary are negligible. We will refer to the parameters described here and Section 2.2.1 as the nominal

parameters.

To estimate the maximum power consumption of the CWU that guarantees thermal safety, we first computed the steady-state solution ($\partial T/\partial t = 0$) of Eq. (2.1) by iterating over values of P_{CWU} within our range of interest (defined below). Based on ISO 14708-1 (the FDA-recognized standard), which states that active implants must not increase surrounding tissues' temperature by more than 2°C, we then defined $P_{\mathrm{CWU}}^{\max}$ as the maximum value of P_{CWU} that satisfies this condition. Specifically, to find $P_{\mathrm{CWU}}^{\max}$, we first ran the simulation model assuming $P_{\mathrm{CWU}} = 0$ (i.e., inactive implant) and stored the resulting temperature field, $T(0)$, for all tissues. Then, we ran the simulation by iteratively increasing the values of P_{CWU} (up to 500 mW, with a step size of 100 mW). For each simulation result, $T(P_{\mathrm{CWU}})$, we defined the temperature increase as $\Delta T(P_{\mathrm{CWU}}) = T(P_{\mathrm{CWU}}) - T(0)$. For the first value of P_{CWU} whose ΔT violated the 2°C constraint, we decreased and locally refined P_{CWU} with a step size of 1 mW. Finally, $P_{\mathrm{CWU}}^{\max}$ was defined as the maximum value that guaranteed $\Delta T(P_{\mathrm{CWU}}) \leq 2°\mathrm{C}$:

$$P_{\mathrm{CWU}}^{\max} = \underset{P_{\mathrm{CWU}} \in [0,600]}{\arg\max}\ \Delta T(P_{\mathrm{CWU}}) : \Delta T(P_{\mathrm{CWU}}) \leq 2°\mathrm{C} \tag{2.4}$$

Table 2.2: The average values of tissues' thermal parameters: thermal conductivity, k, metabolic heat, Q_{m}, and blood perfusion, $\rho_b C_b \omega$

	k W/(m K)	Q_{m} W/m^3	$\rho_{\mathrm{b}} C_{\mathrm{b}} \omega$ W/(m^3 K)	References
Skin	0.36	1004	5192	[51, 72, 119]
Fat	0.24	180	1504	[51, 215, 82]
Muscle	0.50	661	3580	[51, 215, 74]
Ribs	0.43	0	1232	[51, 72, 81]
Lungs	0.44	370	222589	[51, 72, 4]

2.2.2 Sensitivity Analysis

We performed a sensitivity analysis to ensure the robustness of our prediction against the natural variations of physiological and environmental parameters. To this end, the nominal parameters introduced in the previous section were perturbed in both directions based on their physiological and environmental variance. Specifically, we considered the effect of perturbing the following 21 parameters: all those in Tables 2.1 and 2.2, T_{ext}, T_{core} and h. We omitted perturbing the parameters pertaining to the geometry and materials of CWU, given that the CWU's design is fixed.

Table 2.3 lists these parameters with their nominal and perturbed values. The upper and lower values for the tissues' thickness, l, were taken from [114, 194, 25, 145]. For the thermal conductivity, k, the negative and positive perturbation values were estimated from [51]. For the metabolic heat, Q_{m}, the perturbation bounds for the fat and muscle tissues were taken from [215]. Since physiological ranges for the skin and lungs were not available, we estimated their variance at $\pm 10\%$ (the average perturbation from fat and muscle). On the other hand, the lower bounds of blood perfusion were estimated from values at rest, while the upper bounds were estimated from values at double the nominal walking speed (2 mph, 90 bpm). The skin's blood perfusion at rest was estimated as the average of the values from [76, 11, 137, 34, 218, 142, 119]. Similarly, the fat's blood perfusion value at rest was estimated from [137, 34, 218, 142, 82], and the muscle's blood perfusion at rest was estimated from [76, 11, 137, 34, 218, 142, 16]. The ribs' resting blood perfusion was taken from [142], and the lungs' blood perfusion value at rest was taken from [4]. The upper bound values for blood perfusion for the skin, fat, muscle, ribs and lungs were estimated from [119, 82, 74, 81, 4], respectively. Additionally, the range for the heat transfer coefficient, h, was taken from [108]. Finally, we approximated the natural variations of the temperatures T_{b} and T_{ext}.

Our sensitivity analysis was based on calculating the sensitivity coefficient, S_i, defined as

the relative change of $\Delta T(P_{\text{CWU}})$ over the relative change of the parameter θ_i [49]:

$$S_i = \frac{\big(\Delta T(P_{\text{CWU}}^{\max}, \Theta_i^*) - \Delta T(P_{\text{CWU}}^{\max}, \Theta^0)\big)/\Delta T(P_{\text{CWU}}^{\max}, \Theta^0)}{\big(\theta_i^* - \theta_i^0\big)/\theta_i^0}, \qquad i = 1, 2, \cdots, 21 \tag{2.5}$$

In other words, S_i quantifies the impact that the variation of the parameter θ_i has on the tissue's temperature increase in our bio-heat model. In Eq. (2.5), $\Delta T(P_{\text{CWU}}^{\max}, \Theta^0)$ is the maximum temperature increase across all tissues corresponding to $P_{\text{CWU}}^{\max}$ and Θ^0, where $\Theta^0 = [\theta_1^0, \theta_2^0, \cdots, \theta_{21}^0]$ is the vector of perturbed nominal parameters as shown in Table 2.3. Likewise, $\Delta T(P_{\text{CWU}}^{\max}, \Theta_i^*)$ is the maximum temperature increase across all tissues corresponding to $P_{\text{CWU}}^{\max}$ and Θ_i^*, where $\Theta_i^* = [\theta_1^0, \cdots, \theta_i^*, \cdots, \theta_{21}^0]$ and θ_i^* is the perturbed value of the ith parameter. To quantify sensitivity in both directions, for each parameter θ_i, we calculated S_i^+, corresponding to $\theta_i^* = \theta_i^+$ (positive perturbation), and S_i^-, corresponding to $\theta_i^* = \theta_i^-$ (negative perturbation), as shown in Table 2.3.

Based on these sensitivity coefficients, we defined critical parameters as those whose perturbations considerably affected the bio-heat model, i.e., $|S_i| > 10^{-4}$. In other words, the parameters whose relative change of 1% resulted in a relative change of $\Delta T \leq 10^{-4}\%$ were considered non-critical. Since Eq. (2.5) considers the perturbation of a single parameter at a time, we also sought to investigate the effects of perturbing multiple parameters simultaneously. This is necessary to account for the interactions between parameters, and to get a more realistic idea of the potential variations that the bio-heat model could experience. For this reason, we re-estimated $P_{\text{CWU}}^{\max}$ while simultaneously perturbing all the critical parameters. Specifically, we ran simulations for the worst-case scenario (WCS) and best-case scenario (BCS). In the WCS, we perturbed the critical parameters in the direction that would lead to an increase in ΔT, which, in turn, would reduce the CWU's power budget. On the other hand, for the BCS, we perturbed the critical parameters in the direction that would lead

to a decrease in ΔT, which would result in a higher power budget. In both scenarios the non-critical parameters were held at their nominal values. We will refer to the re-estimated power budgets for each scenario as $P_{\text{CWU}}^{\text{WCS}}$ and $P_{\text{CWU}}^{\text{BCS}}$.

Table 2.3: The nominal parameters, θ_i^0 , and their negatively and positively perturbed values, θ_i^- and θ_i^+, respectively.

θ_i	θ_i^0	θ_i^-	θ_i^+
$\theta_1 = l^{\text{skin}}$	2.50	2.24	2.88
$\theta_2 = l^{\text{fat}}$	4.70	1.98	7.90
$\theta_3 = l^{\text{muscle}}$	8.40	7.78	9.02
$\theta_4 = l^{\text{rib}}$	6.00	4.00	8.00
$\theta_5 = \omega^{\text{skin}}$	5192.00	4751.00	6413.00
$\theta_6 = \omega^{\text{fat}}$	1504.00	1331.00	1909.00
$\theta_7 = \omega^{\text{muscle}}$	3580.00	1896.00	5897.00
$\theta_8 = \omega^{\text{rib}}$	1232.00	847.00	1617.00
$\theta_9 = \omega^{\text{lung}}$	222589.00	133173.00	317713.00
$\theta_{10} = Q_{\text{m}}^{\text{skin}}$	1004.00	904.00	1104.00
$\theta_{11} = Q_{\text{m}}^{\text{fat}}$	198.00	169.00	214.00
$\theta_{12} = Q_{\text{m}}^{\text{muscle}}$	694.00	640.00	759.00
$\theta_{13} = Q_{\text{m}}^{\text{lung}}$	370.00	333.00	407.00
$\theta_{14} = k^{\text{skin}}$	0.36	0.25	0.47
$\theta_{15} = k^{\text{fat}}$	0.24	0.22	0.26
$\theta_{16} = k^{\text{muscle}}$	0.50	0.49	0.51
$\theta_{17} = k^{\text{rib}}$	0.43	0.34	0.52
$\theta_{18} = k^{\text{lung}}$	0.44	0.42	0.46
$\theta_{19} = T_{\text{b}}$	37.00	36.50	39.50
$\theta_{20} = h$	5.00	2.50	25.00
$\theta_{21} = T_{\text{ext}}$	20.00	5.00	35.00

2.2.3 Benchtop Validation

We used benchtop open-air experiments to validate our modeling approach. Ultimately, our power budget predictions will be confirmed using *in vivo* testing and will be pursued in our future studies (see Section 2.4). An alternative approach would have been to perform *in vitro* experiments using phantom tissues. For example, we made skin, fat and muscle phantom tissues to test the wireless communication capabilities of our CWU prototype [118]. Unlike

electrical conductivity and permittivity, which we could easily manipulate in phantom tissues, metabolic heat production and blood perfusion effects cannot be easily replicated [116]. Furthermore, our sensitivity analysis shows that blood perfusion is among the most critical parameters of the bio-heat model. Thus, our bio-heat model could not be accurately reproduced *in vitro*, and as an alternative, we chose to validate our modeling approach using benchtop open-air experiments. To this end, we built a thermal replica of the CWU with a Ti enclosure whose dimensions and power consumption levels match those of the bio-heat model. We then measured the surface temperature of this thermal prototype in an open-air experiment and compared these experimental results to those obtained via simulations.

Specifically, we fabricated the thermal prototype as a rectangular-shaped prism (59 × 50 × 12 mm), assembled from two clamshell Ti alloy (ASTM B265 Grade 2) parts, which were laser-welded in a hermetic fashion. This alloy is a commonly used material for medical implants due to its biocompatibility [224]. The Ti case (1 mm-thick shell) encloses a circuit of resistors and a battery connected to external switches (see Figs. 2.2A and 2.2B). With these switches, the prototype could be powered and set to operate at one of four power consumption levels (300, 400, 500, and 600 mW). The prototype also had a connector to enable the battery to be charged externally. Note that the thermal prototype dimensions, enclosure material, wall thickness and power consumption levels closely match those of the bio-heat model described in Section 2.2.1.

For each power consumption level, we conducted an open-air experiment, as described below. We placed the thermal prototype on a laminate wood benchtop, turned the prototype on with a certain power consumption configuration, and waited for one hour for heat to reach a quasi-steady state. Next, we measured the prototype's top surface temperature using both a thermocouple, $T_{\mathrm{p,t}}$, and a thermal camera (FLIR C2, Teledyne FLIR, Wilsonville, OR), $T_{\mathrm{p,c}}(x, y)$. To minimize reflection and accommodate more accurate temperature measurements with the thermal camera, we painted the top surface of the prototype black. We

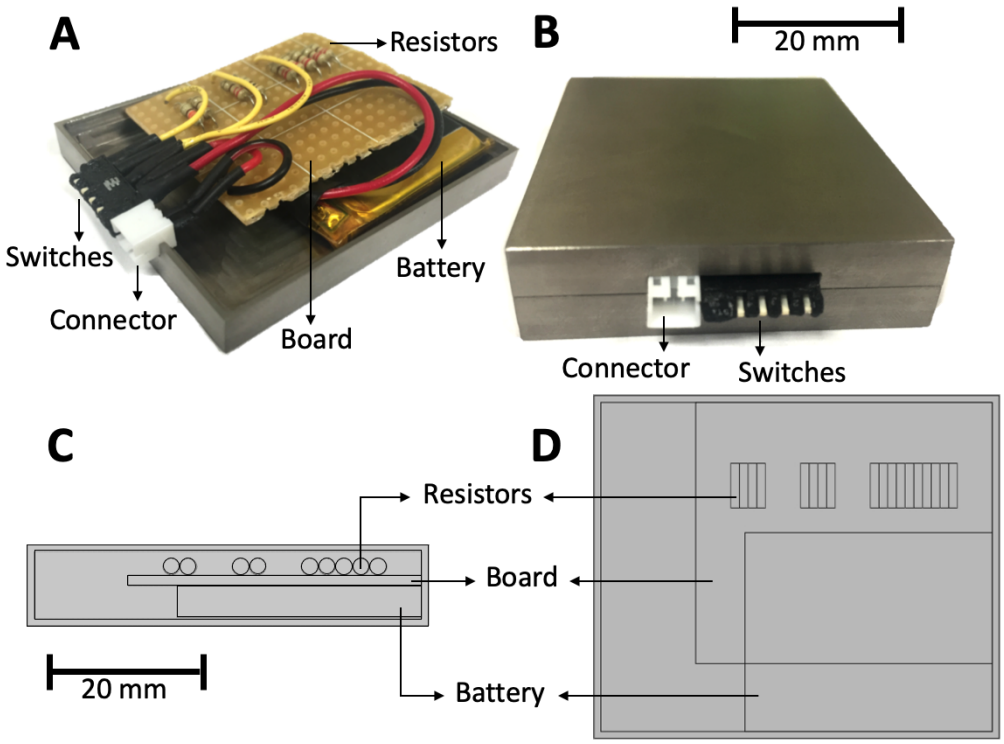


Figure 2.2: Different views of our custom-designed CWU thermal prototype and its COMSOL model. (A) View of the prototype's interior prior to laser-welding the two clamshells. Different switch positions engage different combinations of resistors for the prototype to operate at different powers. (B) A front view of the laser-welded prototype. (C) Cross-section of the prototype's COMSOL model (lateral view). (D) Cross-section of the prototype's model (top view).

also took periodic measurements of the room temperature, T_{ext}, the battery's voltage, V_{b}, and its current, I_{b}, since these variables changed over time, thus affecting the prototype's surface temperature. Specifically, the room temperature measurements were taken with a thermocouple in close proximity to the air surrounding the prototype and repeated every 10 minutes for about an hour. Moreover, we measured the battery's voltage and current every 10 minutes from the moment the prototype was powered until the end of the experiment. These measurements were taken using a digital multimeter (Tenma 72-8400, Tenma Test Equipment, Springboro, OH). Note that as the battery discharges over time, V_{b} decreases, which, in turn, lowers the prototype's instantaneous power consumption.

We then created a COMSOL model of the CWU thermal prototype in an open-air envi-

ronment, which we refer to as the benchtop model. Its dimensions precisely matched those of the thermal prototype, including the 1 mm Ti shell, battery (36 × 29 × 4.7 mm), resistors (2.5 mm diameter, 6.5 mm length), and board (43 × 38 × 1.6 mm), as shown in Figs. 2.2C and 2.2D. The prototype was modeled sitting on top of a rectangular laminate wood benchtop (600 × 600 × 30 mm).

We modeled heat transfer using the same approach as in the bio-heat model (see Section 2.2.1). Given that metabolic heat and blood perfusion do not apply to the benchtop model, we set Q_{m} and ω from Eq. (2.1) to 0. Analogous to the bio-heat model, the software applied this PDE to each component of the benchtop model, and computed its steady-state solution. To do so, we first chose the parameters of the benchtop model as follows. We set the thermal conductivity, k, of Ti (ASTM B265 Grade 2) and the benchtop's laminated wood to be 21.8 W/(m K) [23] and 0.12 W/(m K) [179], respectively. We also set the thermal conductivity of the resistors and board to be 1.88 W/(m K) [158] and 0.29 W/(m K) [196], respectively. Additionally, we kept the thermal conductivity of the battery and air the same as in the bio-heat model (see Section 2.2.1). Finally, we defined the heat source as $Q_{\mathrm{ext}} = P_{\mathrm{b}}/V_{\mathrm{R}}$, where P_{b} is the battery's power usage and V_{R} is the overall volume of the selected resistors, as determined by the combination of switches. The battery's power was estimated as $P_{\mathrm{b}} = V_{\mathrm{b}} \times I_{\mathrm{b}}$, where V_{b} and I_{b} were measured throughout the benchtop experiments, as described above.

For this boundary problem, we enforced temperature continuity at the benchtop-prototype interface and all other internal interfaces. We also assumed that the heat transfer occurred through free convection on all external boundaries, similar to the skin-air boundary of the bio-heat model, Eq. (2.2). In this equation, we estimated the room temperature, T_{ext}, as the time average of the temperature measurements taken throughout the benchtop experiment. Another critical parameter of this equation is the heat transfer coefficient, h, which is sensitive to local air flow and temperature, and can vary greatly across environments [108].

Therefore, we estimated h experimentally using Newton's law of cooling. Specifically, a 306 $\times$ 52 $\times$ 10 mm Ti (ASTM B265 Grade 2) bar was placed in the oven and heated to at least 40°C above the room temperature. Then, the bar was removed from the oven and placed on the same benchtop as the thermal prototype to let it cool. The bar's temperature was recorded every 30 seconds for about an hour. These measurements were then used to fit a linear regression to the logarithmic form of the cooling equation:

$$\ln \frac{\Delta T(t)}{\Delta T(0)} = -\frac{hA}{mc}t \tag{2.6}$$

where $\Delta T(t) = T_{\text{bar}}(t) - T_{\text{r}}$, and $T_{\text{bar}}(t)$ is the time dependent temperature of the bar and T_{r} is the room air temperature, respectively. The parameters A, m, and c are the area (m^2), mass (kg), and heat capacity ($\text{J}/(\text{kg}\,\text{K})$) of the Ti bar, respectively.

For each of the four experiments, we simulated the COMSOL benchtop model twice and compared these results to the experimental measurements. This was necessary to reconcile a constant power consumption assumed by the steady-state solution of Eq. (2.1) and a decreasing power consumption observed experimentally due to battery draining over the course of each experiment. Specifically, we simulated the model while assuming two extreme power consumptions, $P_{\text{b}}^{\text{max}}$ and $P_{\text{b}}^{\text{min}}$, which were derived from the battery voltage and current measurements taken at the beginning and end of each benchtop experiment. For each case, we computed the average temperature of the modeled prototype's top surface, $T_{\text{m}}(P_{\text{b}}^{\text{max}})$ and $T_{\text{m}}(P_{\text{b}}^{\text{min}})$, respectively. These values were then compared to the experimentally derived temperature T_{p}, where T_{p} is the average of the thermal image measurements, $T_{\text{p,c}}$ (averaged over space), and the thermocouple measurements, $T_{\text{p,t}}$. The value T_{p} was calculated every 10 minutes and compared to the simulated range $[T_{\text{m}}(P_{\text{b}}^{\text{min}}), T_{\text{m}}(P_{\text{b}}^{\text{max}})]$.

2.3 Results

2.3.1 Bio-heat Model

We simulated the bio-heat model in Eq. (2.1) using the FEM in COMSOL. To determine the appropriate mesh size, we used an adaptive physics-controlled mesh algorithm. Specifically, we solved Eq. (2.1) using the following predefined COMSOL mesh sizes: *coarser, coarse, normal, fine, finer* and *extra fine*. The difference in the resulting temperature going from *coarser* to *extra fine* mesh size kept decreasing, with the difference between the *finer* and *extra fine* mesh size being < 0.001°C. This suggested that the simulation had converged with respect to the mesh size [103]. Therefore, we chose the *finer* mesh size in our bio-heat model to balance accuracy and computational cost. We ran the simulations using the geometric parameters shown in Table 2.1 and Section 2.2.1, and the thermal parameters from Table 2.2 and Section 2.2.1.

We found $P_{\text{CWU}}^{\max}$ by the iterative procedure described in Section 2.2.1. To simplify the interpretation of volumetric temperature data, we focused on the worst-case scenario line segment (marked by the red dashed line in Fig. 2.1A), where the thermal impact due to the CWU, judged by $\Delta T(P_{\text{CWU}})$, is highest. Fig. 2.3 shows the simulated $\Delta T(P_{\text{CWU}})$ along this segment for different values of P_{CWU} within our range of interest. For all power consumption levels, we observed the highest temperature increase in the fat layer, followed by the muscle, skin, ribs, and lungs. We also observed that ΔT peaked at the same depth, $d^* \approx 12.2$ mm, for all power levels. This depth corresponds to the point where the worst-case scenario line is tangential to the implant. This figure also shows that $\Delta T(500)$ violated the 2°C threshold in the fat tissue layer. Therefore, we iterated the value of P_{CWU} below 500 mW with a precision of 1 mW, and we found the maximum power consumption to be $P_{\text{CWU}}^{\max} = 458$ mW. Fig. 2.3 confirms that $\Delta T(458) \leq 2$°C for all tissue layers.

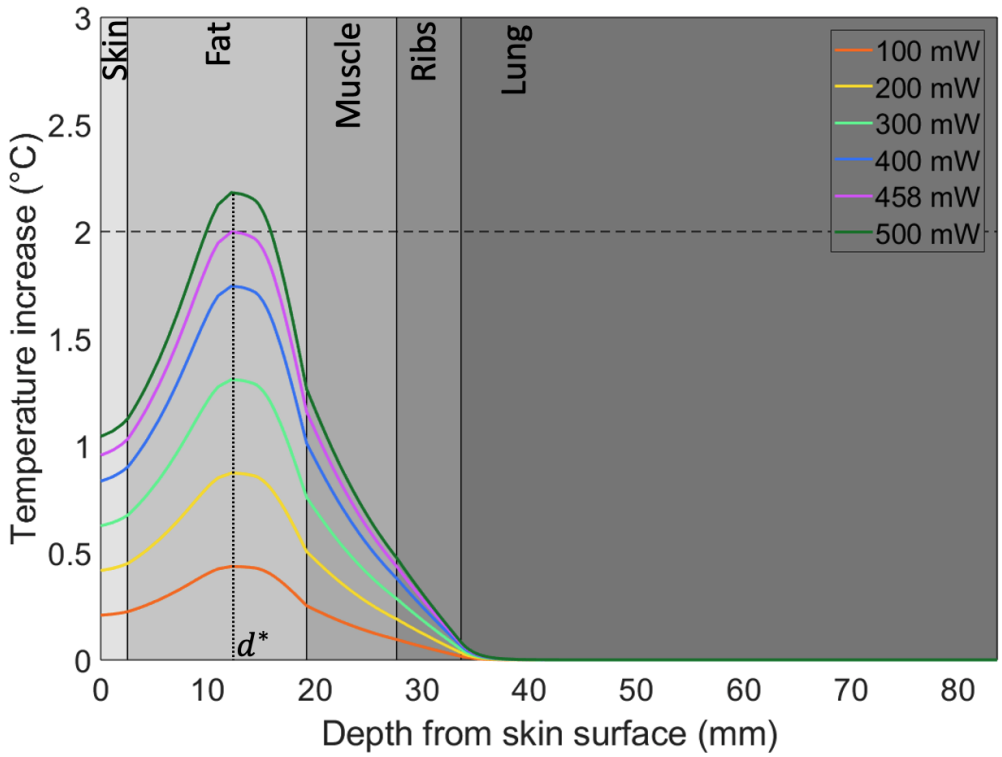


Figure 2.3: Temperature increase, $\Delta T(P_{\mathrm{CWU}})$, for different values of P_{CWU}, calculated along the axis of the CWU with the tissues' highest ΔT. This region undergoes the highest thermal impact within the overall geometry. The solid vertical lines mark the boundaries of each layer, which are colored in different shades of gray and labeled at the top. The dashed horizontal line marks the 2°C thermal safety threshold. The dotted vertical line marks the depth, d^*, at which ΔT is highest for all power levels.

Fig. 2.4 shows the 2D distribution of ΔT corresponding to the maximum power consumption, $P_{\mathrm{CWU}}^{\mathrm{max}} = 458$ mW, over the central cross-section. Consistent with Fig. 2.3, the highest tissue temperature increase occurred in the fat tissue. Note that ΔT exceeded the 2°C thermal safety threshold in the interior of CWU (parts of the electronics layer and Ti shell). However, only the biological tissues are subjected to the thermal safety threshold.

2.3.2 Sensitivity Analysis

To quantify the robustness of the bio-heat model with respect to the nominal parameter values, we computed the sensitivity coefficient, S_i, for all the parameters, θ_i $(i = 1, 2, \cdots, 21)$.

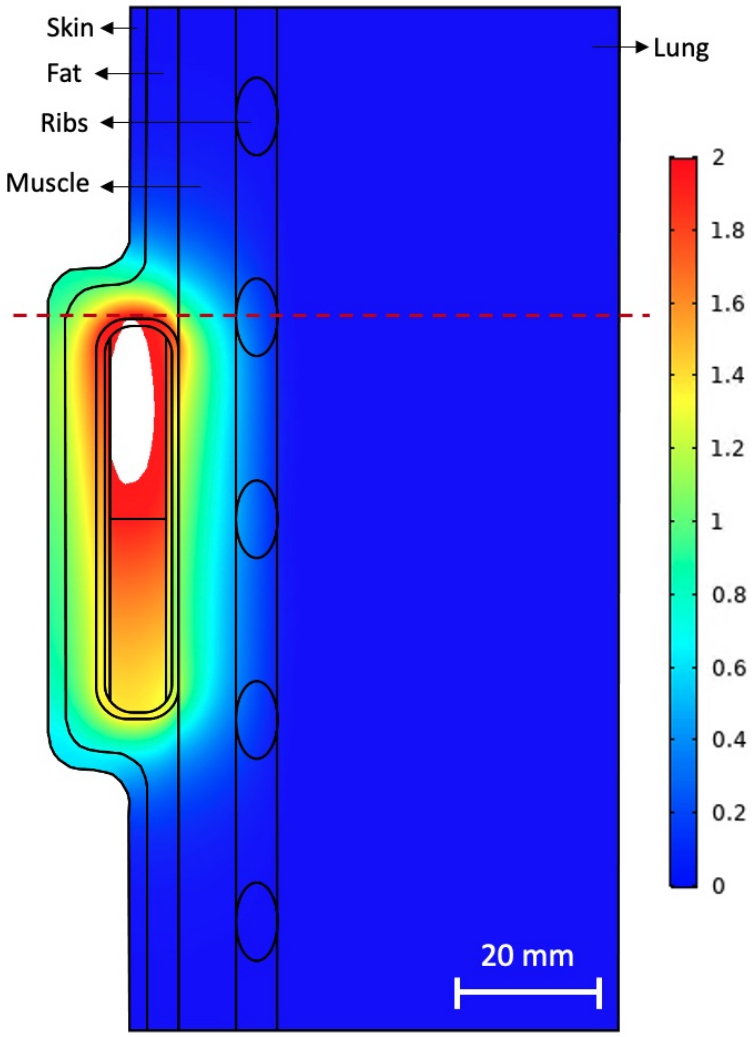


Figure 2.4: $\Delta T(458)$ in °C over the central 2D cross-section from Fig. 2.1B. Areas where $\Delta T > 2$°C were not assigned a color to visually preserve the temperature resolution. The red dashed line indicates the axis with the tissues' highest ΔT.

Table 2.4 shows the values of S_i for the positive and negative perturbations shown in Table 2.3. Based on the criteria $|S_i| > 10^{-4}$, the simulation results were sensitive to 15 critical parameters. The perturbations of the remaining 6 non-critical parameters did not significantly alter the simulation results.

Finally, we modeled the combined effect of all the critical parameters. We perturbed the 15 critical parameters simultaneously (while keeping the nominal values of the non-critical parameters) to simulate a worst and best-case scenario. We then re-estimated the maximum

power consumption for each case, namely $P_{\text{CWU}}^{\text{WCS}}$ and $P_{\text{CWU}}^{\text{BCS}}$, and found the power budget range to be between 378 mW and 538 mW.

Table 2.4: The sensitivity coefficients, S_i^- and S_i^+, for the respective perturbation of each parameter, as indicated in Table 2.3. The critical parameters are highlighted in grey.

θ_i	S_i^-	S_i^+
$\theta_1 = l^{\text{skin}}$	$-9.43 \cdot 10^{-2}$	$-8.28 \cdot 10^{-2}$
$\theta_2 = l^{\text{fat}}$	$-3.64 \cdot 10^{-2}$	$-1.39 \cdot 10^{-2}$
$\theta_3 = l^{\text{muscle}}$	$4.42 \cdot 10^{-2}$	$3.88 \cdot 10^{-2}$
$\theta_4 = l^{\text{rib}}$	$4.27 \cdot 10^{-2}$	$2.99 \cdot 10^{-2}$
$\theta_5 = \omega^{\text{skin}}$	$-8.21 \cdot 10^{-2}$	$-7.34 \cdot 10^{-2}$
$\theta_6 = \omega^{\text{fat}}$	$-8.31 \cdot 10^{-2}$	$-7.89 \cdot 10^{-2}$
$\theta_7 = \omega^{\text{muscle}}$	$-1.01 \cdot 10^{-1}$	$-7.55 \cdot 10^{-2}$
$\theta_8 = \omega^{\text{rib}}$	$-7.34 \cdot 10^{-4}$	$-7.25 \cdot 10^{-4}$
$\theta_9 = \omega^{\text{lung}}$	$-6.49 \cdot 10^{-3}$	$-3.60 \cdot 10^{-3}$
$\theta_{10} = Q_{\text{m}}^{\text{skin}}$	$2.34 \cdot 10^{-8}$	$2.34 \cdot 10^{-8}$
$\theta_{11} = Q_{\text{m}}^{\text{fat}}$	$1.19 \cdot 10^{-8}$	$1.19 \cdot 10^{-8}$
$\theta_{12} = Q_{\text{m}}^{\text{muscle}}$	$7.05 \cdot 10^{-10}$	$7.07 \cdot 10^{-10}$
$\theta_{13} = Q_{\text{m}}^{\text{lung}}$	$-4.21 \cdot 10^{-10}$	$-4.15 \cdot 10^{-12}$
$\theta_{14} = k^{\text{skin}}$	$-3.45 \cdot 10^{-2}$	$-1.20 \cdot 10^{-2}$
$\theta_{15} = k^{\text{fat}}$	$-2.48 \cdot 10^{-1}$	$-2.22 \cdot 10^{-1}$
$\theta_{16} = k^{\text{muscle}}$	$-2.32 \cdot 10^{-1}$	$-2.27 \cdot 10^{-1}$
$\theta_{17} = k^{\text{rib}}$	$-1.53 \cdot 10^{-2}$	$-1.24 \cdot 10^{-2}$
$\theta_{18} = k^{\text{lung}}$	$-4.77 \cdot 10^{-3}$	$-4.48 \cdot 10^{-3}$
$\theta_{19} = T_{\text{b}}$	$-1.09 \cdot 10^{-6}$	$-1.42 \cdot 10^{-6}$
$\theta_{20} = h$	$-2.29 \cdot 10^{-2}$	$-1.45 \cdot 10^{-2}$
$\theta_{21} = T_{\text{ext}}$	$1.00 \cdot 10^{-5}$	$8.78 \cdot 10^{-5}$

2.3.3 Benchtop Validation

The benchtop experiments were performed in a dedicated room with minimal disturbance from external factors. As explained in Section 2.2.3, we placed the CWU thermal prototype on the benchtop, turned the power on, and waited for one hour before taking temperature measurements from the device's surface. We also periodically measured the room temperature, as well as the battery's voltage and current throughout the experiment. We repeated the experiment for the nominal power consumption levels of 300, 400, 500, and 600 mW.

Fig. 2.5A shows a representative example of the prototype's quasi-steady state surface temperature for the 500 mW set-up.

We then simulated these experiments in COMSOL, using our benchtop computational model (see Section 2.2.3). Consistent with the bio-heat model, we used the predefined *finer* mesh setting for these simulations. The model used the parameters specified in Section 2.2.3, except for the heat transfer coefficient, h. As explained earlier, this parameter critically depends on the environment and, therefore, had to be determined experimentally in the same dedicated room as above. To this end, we used the Ti bar temperature decay experiment to fit a linear regression based on Eq. (2.6) with $A = 0.016$ m^2, $m = 0.718$ kg, and $c = 523$ J/(kg K) [43]. This resulted in a heat transfer coefficient estimate $h = 13$ W/(m^3 K). Fig. 2.6 shows the temperature decay measured experimentally, as well as the prediction based on this value of h. Note that the goodness-of-fit measure, R^2=0.995, suggests a high concordance between experimental data and model prediction. Once h was found, we simulated the benchtop model at the four nominal power consumption levels. Fig. 2.5B shows an example of the simulated prototype's surface temperature distribution for the 500 mW power consumption.

From experimental data, we calculated the thermal prototype's average surface temperature, T_{p}, every 10 minutes, and compared these values to the simulated range $[T_{\mathrm{m}}(P_{\mathrm{b}}^{\mathrm{min}}), T_{\mathrm{m}}(P_{\mathrm{b}}^{\mathrm{max}})]$ (see Section 2.2.3). Fig. 2.7 shows the results at the four nominal power consumption levels. For each power level, there is an overlap between the values of T_{p} and the range $[T_{\mathrm{m}}(P_{\mathrm{b}}^{\mathrm{min}}), T_{\mathrm{m}}(P_{\mathrm{b}}^{\mathrm{max}})]$. As expected, higher power consumption levels led to a wider gap between the prototype's surface temperature and the room temperature, and this was consistently observed in both experimental and simulated data. Also note that higher power configurations drained the battery's voltage faster, which, in turn, widened the range of T_{m}. Finally, we quantified the agreement between the experimental and simulation results by calculating the correlation coefficient between T_{p} and T_{m}. Specifically, for each power level, we correlated the first and last value of T_{p} with $T_{\mathrm{m}}(P_{\mathrm{b}}^{\mathrm{min}})$ and $T_{\mathrm{m}}(P_{\mathrm{b}}^{\mathrm{max}})$, respectively, and

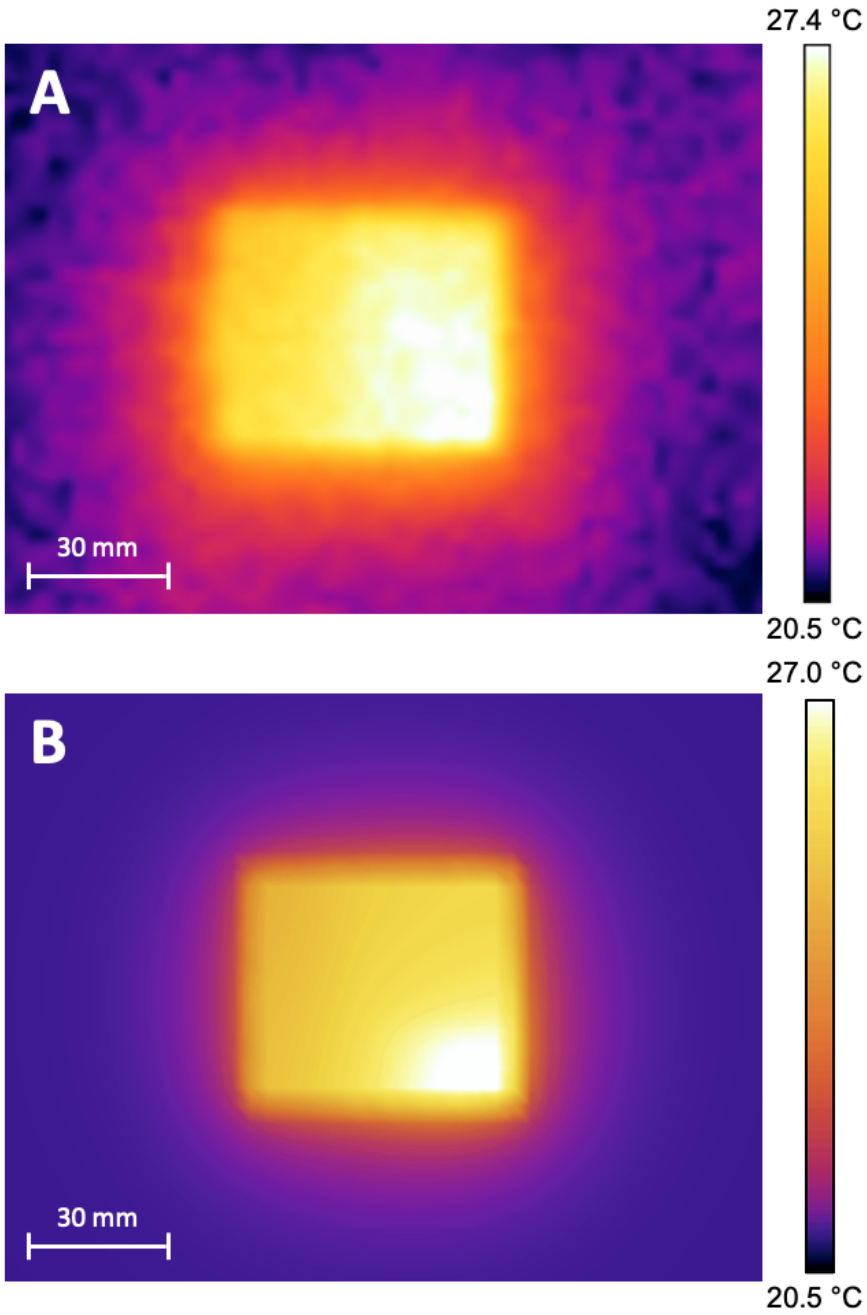


Figure 2.5: 2D temperature maps of the CWU thermal prototype and its benchtop COMSOL model for the 500 mW configuration. The bright spot in the lower right corner overlaps with the position of the resistors. (A) Thermal camera image of the prototype placed on the benchtop. (B) An equivalent map produced by the benchtop computational model with $T_{\text{ext}} = 22.9°\text{C}$.

obtained the correlation coefficient of 0.86 (p-value = 0.006).

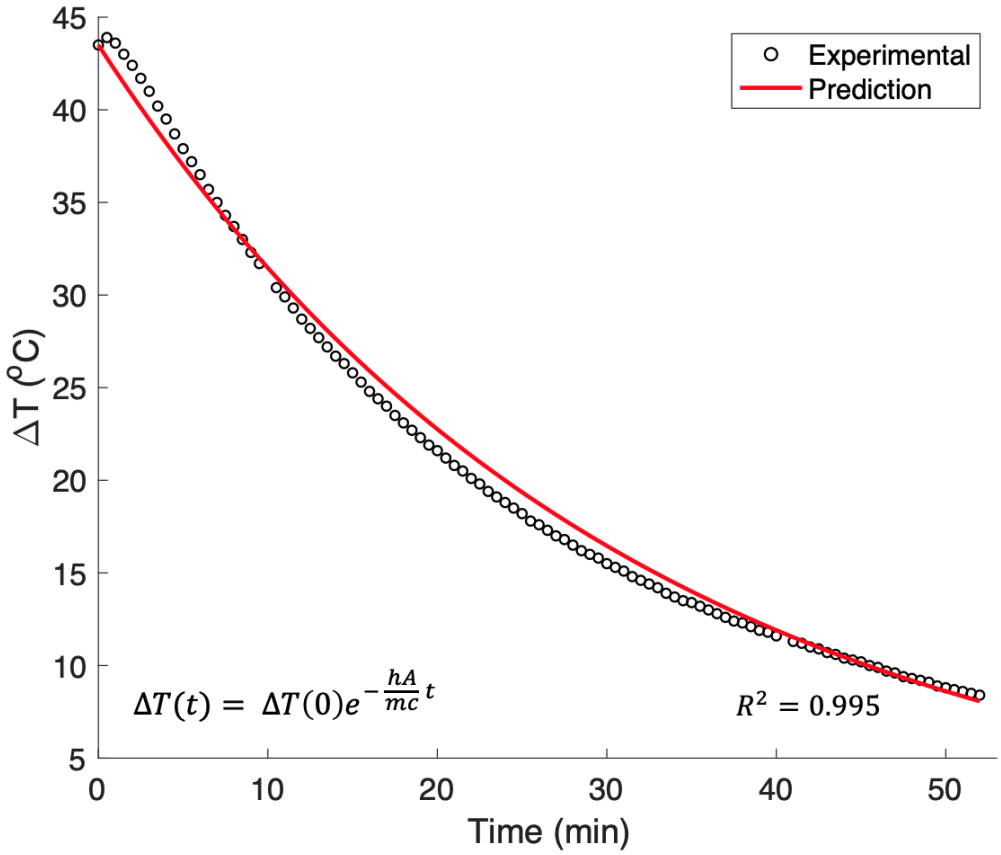


Figure 2.6: Cooling profile of a Ti bar in an open-air benchtop environment. The black dots show the temperature decay measured experimentally, while the red line is an exponential model derived from Eq. (2.6), with the best linear fit, $h = 13$.

2.4 Discussion

The thermal impact of fully implantable BCI systems remains an underresearched topic [220]. Our CWU design in particular, and implantable BCI in general (Fig. 1.6), bear some resemblance with commercially available IPGs. However, with an estimated range between 200 and 1600 μW [38], IPGs' power consumption is about two orders of magnitude lower than that of implantable BCIs. This power gap is expected to be even larger for BD-BCIs. For this reason, we cannot assume that the thermal behavior of commercially available IPGs generalizes to fully implantable BCIs.

To the best of our knowledge, this is the first thermal impact study of a CWU, envisioned

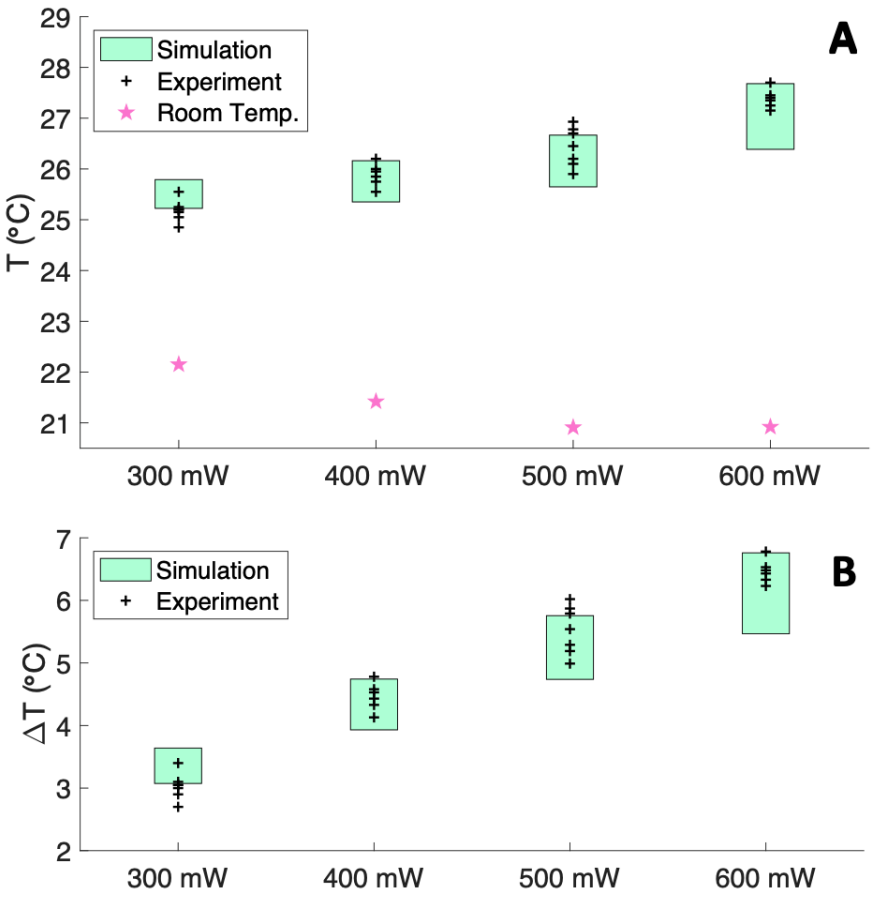


Figure 2.7: The average top surface temperature of the thermal prototype in comparison to the simulated temperature range for different power consumption levels. (A) Actual temperature. (B) The same values expressed as a deviation from the room temperature. The black crosses are experimental temperature measurements, T_{p}, repeated at $\sim$10 minute intervals. The cyan boxes represent the simulated temperature range $[T_{\mathrm{m}}(P_{\mathrm{b}}^{\mathrm{min}}), T_{\mathrm{m}}(P_{\mathrm{b}}^{\mathrm{max}})]$. The pink stars show the average room temperature, T_{ext}.

as part of a fully-implantable BD-BCI. Based on this study, we estimated the CWU's maximum power budget that guarantees a thermally safe operation. Specifically, we simulated the bio-heat model with nominal parameters, and we predicted that the CWU's power budget cannot exceed 458 mW without violating the 2°C thermal safety threshold. When perturbing 21 nominal parameters within their natural physiological and environmental range, 6 parameters had a negligible effect on the power budget. The remaining 15 parameters were critical and their simultaneous perturbation resulted in a power budget range between 378 and 538 mW. We believe that this power budget is sufficient for the CWU to perform its

functions, such as training the decoder, online decoding, wireless communication and data transmission, and cortical stimulation. For example, our recently developed CWU benchtop prototype consumed on average 150 mW of power while performing all the BCI functions except stimulation [205]. Our newest BD-BCI benchtop prototype showed that cortical stimulation may require up to an additional 230 mW [192]. Taken together, these values suggest that the power budget range estimated based on our simulations is sufficient to power an actual CWU and likely a fully implantable BD-BCI.

Our bio-heat modeling approach makes several simplifying assumptions. However, most of these assumptions favored a more conservative power budget estimate, as described below. For example, we neglected the effects of radiative heat transfer. Since human skin is generally warmer than external room temperature, radiation would take heat away from the human body, and even more so when the CWU is powered. Therefore, the net effect of radiative heat transfer would be an even greater power budget. Another simplification of our approach is that we computed ΔT by comparing the temperature resulting from the active CWU simulation to a model where the CWU is inactive. An alternative way to define ΔT would be to compare the active simulation to a model where the CWU is not implanted. However, after comparing the two approaches, we conclude that the results presented here lead to a more conservative power budget estimate. Namely, in the absence of an implant, the fat and skin layers are closer to the body core and so their temperature is higher. This would, in turn, result in a lower value of ΔT and, therefore, would yield an even higher power budget. Furthermore, our model neglected external clothing. However, our worst-case scenario simulations assumed a 2 cm-thick wool layer and showed the effect of clothing on the power budget estimation to be minimal (< 2 mW). Additionally, we assumed a uniform electronics layer with thermal properties based on those of the PCB. Instead, a more detailed approach would be to split the electronics layer into the PCB and its electronic components (microcontroller core, H-bridge, current source, RAM module, NAND storage module, and radio TRX) [205, 192]. Given that the exact composition and arrangement

of these components are currently unknown, we opted for a simpler approach. Once this information is known, such a detailed model could be used to rearrange the internal CWU components and further optimize the power budget. We also omitted a polymeric connection header that usually houses connectors and telemetry antenna in contemporary IPGs [175, 195]. However, since none of the elements in the header generate heat, we do not expect it to affect our power budget predictions. Finally, the long-term heating of tissues can trigger adaptation mechanisms such as angiogenesis, which increases blood perfusion and, in turn, reduces temperature. However, this process is poorly understood [39] and therefore could not be easily incorporated into our model.

Table 2.4 shows that the thermal conductivity of fat and muscle, as well as the muscle blood perfusion, were the three most critical parameters of our bio-heat model, followed by the skin thickness, and the fat and skin blood perfusion. This conclusion is consistent with the findings reported by *in vivo* animal studies [159]. Table 2.4 also shows that the perturbation of the same parameter across multiple tissues may or may not have the same effect on ΔT. For example, the increase of the fat's thickness led to a decrease in ΔT, while the increase of the muscle's thickness led to an increase in ΔT. (Note that from Eq. (2.5) it follows that both $S_i^+ > 0$ and $S_i^- < 0$ correspond to an increase in ΔT). For other parameters (e.g., blood perfusion), the perturbations in the same direction led to the same behavior across all tissues.

The main limitation of our study is the lack of *in vivo* validation. Nonetheless, FEM simulations are widely accepted in predicting active implants' behavior [54, 138, 201, 226, 161]. This is especially true for preliminary studies, where it would be both unethical and cost ineffective to perform animal testing. Once an active implant prototype has been finalized, animal studies are appropriate to test both its function and safety. These include long-term functional tests and FDA safety requirements such as thermal impact, biocompatibility, and current leakage (ISO 14708-1).

In the absence of animal testing, we used a benchtop model to validate the general FEM approach presented here. For this model, the simulation results overlapped with the experimental results for all power configurations (see Fig. 2.7), and therefore we conclude that the FEM reliably predicts experimental thermal behavior. The differences between the experimental and simulation results can be attributed to the model's simplifying assumptions. First, the model assumed constant parameters, like T_{ext} and h. However, these parameters could have changed during the course of experiments due to sudden fluctuations in room temperature and air flow, caused by external factors (door opening/closing, A/C turning on/off). Additionally, the benchtop simulation omitted smaller components like the cables, switches and connector; however, we do not expect these elements to have a great influence on the heat distribution. Lastly, observational errors from the experimental measurements could also have been a source of discrepancy.

Our estimated power budget range (378 to 538 mW) provides an informative constraint for the future design of a fully implantable CWU and a BD-BCI system, as outlined in Fig. 1.6. This study focuses on the thermal analysis of the CWU because it is the most power-hungry component of the BD-BCI system. Other heat-dissipating components include the skull unit (SU) and sensory (stimulating) electrodes. Our preliminary power budget estimates for the SU are provided in [181], and efforts to incorporate the stimulating electrodes into this model are currently under way. Nevertheless, to ultimately validate the thermal safety of these components, *in vivo* animal testing must be done. However, animal testing is out of the scope of this work and will be pursued in our future studies, where the CWU and other components of the BD-BCI system will be implanted in a large animal model. Specifically for the CWU, a temperature sensor (e.g., thermistor) can be integrated within the implant to continuously measure its surface temperature at the hottest region. Note that this temperature is equal to the temperature of the adjacent tissues due to temperature continuity (see Fig. 2.4). The CWU's wireless communication system could be exploited to obtain periodic measurements of the CWU's surface temperature. To validate the thermal

safety of the device, its thermal impact can be assessed under different power consumption levels (generated by different operation modalities), and ensure that the 2°C threshold is not violated under any circumstances.

2.5 Conclusion

To the best of our knowledge, this is the first thermal impact study of a CWU, envisioned as part of a fully-implantable BD-BCI. Based on this study, we estimated the CWU's maximum power consumption that guarantees a thermally safe operation. Specifically, we found that a nominal power consumption of 458 mW would not lead to an increase of the surrounding tissues' temperature by more than 2°C (ISO 14708-1). Furthermore, we performed a sensitivity analysis to identify physiological and environmental parameters that are critical for the power budget estimate. We then varied these parameters over their natural range, and found the power budget estimate to range between 378 and 538 mW. These power budget estimates provide an important specification for the design of our fully implantable BD-BCI system. Additionally, we designed a benchtop experiment to confirm that our simulation approach (FEM implemented in COMSOL) can faithfully model the thermal behavior of a CWU-like implant. Next, we will estimate the power budget for the remaining implantable components of the BD-BCI (see Chapter 3). Finally, in the future, our research efforts will be directed toward performing *in vivo* animal studies to validate these power budget predictions.

Chapter 3

Power Budget of the Skull Unit

3.1 Motivation

After estimating the thermally safe power budget of the CWU in Chapter 2, the next step to complete the thermal assessment of the BD-BCI is to estimate the thermally safe power budget of the SU. Previous studies have demonstrated the predictive value of numerical bio-heat transfer models for different types of active head implants, including active microelectrode arrays (MEA) [103], deep brain stimulators [54], an MEA-based cortical implant [184], and a retinal prosthesis [116]. However, due to the unique features of our SU implant, including its ability to simultaneously record and stimulate, the findings from these previous studies do not generalize to our SU design. For example, the power consumption of active head implants ranges from 40 μW [9] to 3 mW [136], which is at least one order of magnitude smaller than what might be needed to power an SU in a fully-implantable BD-BCI system. To address this question, we developed a numerical model to simulate the combined thermal effects of the heat dissipated by the SU and the heat caused by cortical stimulation. We used this model to determine the SU's maximum power consumption that guarantees thermal safety,

as defined by the FDA. Similar to Chapter 2, we performed a sensitivity analysis to assess the robustness of the thermal model against the natural variations of the physiological and environmental parameters and estimate a thermally safe SU power budget range. This work builds upon our previous work [181], where we used a simpler model to provide a preliminary estimate of the SU's power budget. Furthermore, the current study complements Chapter 2 on predicting the power budget of the CWU—the most power-hungry component of the BD-BCI system. Therefore, this chapter completes the thermal assessment of the envisioned fully-implantable BD-BCI system.

3.2 Materials & Methods

We simulated the thermal behavior of the SU and sensory ECoG grid using the Finite Element Method (FEM), implemented in COMSOL. We also performed a sensitivity analysis of our model against the natural variations of physiological and environmental parameters. Some of the methodology presented here is similar to Chapter 2.

3.2.1 Geometric Model

Our model represents a cylindrical cut-out of the human head with multiple tissue layers and implanted components (see Fig. 3.1). We assumed the scalp (the outermost layer) to be in direct contact with the air while omitting the effect of hair. Our analysis (see Section 3.4) showed that hair had little influence on the power budget. We estimated the thickness of the scalp, skull, dura mater, and subarachnoid space (SS) layers from anatomical data (see Table 3.1). This table also lists the thickness of the implantable components. We modeled the brain as a 50-mm thick cylindrical volume with a 50-mm radius. This volume is sufficiently large to ensure its inner-most surface is at the brain's core temperature [103] and its lateral

surfaces are thermally insulated. We envision the SU to be implanted underneath the scalp, fixed on the exterior aspect of the skull after a full-thickness craniectomy, similar to the RNS system [153]. With the depth of the SU being smaller than the thickness of a typical human skull, it is likely that after a full-thickness craniectomy the dura mater will thicken and serous fluid will fill the remaining gap between the SU and the dura mater [126]. Since this process is not completely understood, we assumed this gap to be filled with fluid whose thermal and electrical properties are similar to those of a physiological saline solution (0.9%). An alternative approach would be to perform a partial-thickness craniectomy; however, this could trigger bone remodeling beneath the SU, which over time could extrude the implant. We also envision the electrode grid to be implanted subdurally, above the SS [185]. Note that the SS was assumed to primarily contain cerebrospinal fluid (CSF). Also, note that in this model we omitted thinner head tissues like the pia mater.

Table 3.1: The average thickness of tissue layers and implantable components.

Tissue layer	Thickness (mm)	Reference	Component	Thickness (mm)
Scalp	3.35	[87]	SU shell	1.00
Skull	7.80	[134]	SU flange	2.00
Dura Mater	0.89	[112]	Electronics	2.00
SS	1.43	[66]	Air gap	1.00
Brain	50.00		Substrate (Si)	0.60
			Electrodes (Pt)	0.20

We envision the SU as a cylindrical titanium (Ti) shell, with an outer radius of 6 mm. Within the implant, there is a centered electronics layer surrounded by air gaps on both sides. We modeled the electronics layer as a 2-mm thick printed circuit board (PCB). The SU is covered with a solid Ti flange (10 mm radius, 2 mm thick) that allows fixation onto the skull. On the other hand, we modeled the ECoG grid as a 32 $\times$ 16 mm silicone (Si) substrate embedded with a 4 $\times$ 8 array of electrodes. The electrodes were modeled as platinum (Pt) cylinders with a 1.25 mm radius and 4 mm pitch (corresponding to high-density ECoG grid dimensions). We envision using high-density ECoG grids because they offer a higher spatial

resolution than standard grids [206]. To simulate the worst-case scenario, we assumed the grid is placed such that the stimulating electrodes (shown in red and green in Fig. 3.1) are aligned with the center of the SU.

3.2.2 Mathematical model

To model the physics of our problem, we simultaneously used two modules from COMSOL. Specifically, we used the *heat transfer in solids* module to simulate heat transfer through the different tissues and implantable components, and the *electric currents* module to simulate the heat generated by cortical stimulation currents.

Heat transfer

We used Pennes' equation [162] to model the bio-heat transfer:

$$\rho C \frac{\partial T}{\partial t} = k\nabla^2 T - \rho_{\mathrm{b}} C_{\mathrm{b}} \omega (T - T_{\mathrm{b}}) + Q_{\mathrm{m}} + Q_{\mathrm{ext}} \tag{3.1}$$

where ρ (kg/m^3) and C (J/(kg K)) are the material's mass density and specific heat capacity, respectively. The variable T (K) is the temperature at a position (x, y, z) and time t. On the right-hand side, the first term accounts for heat conduction, where k (W/(m K)) is the material's thermal conductivity. The second term models the effect of blood perfusion, where ω ((ml/s)/ml) is the volumetric flow rate of the perfusing blood per unit volume of tissue, and the subscript, b, refers to arterial blood. We set the blood temperature to the body's core temperature, $T_{\mathrm{b}} = 37°\mathrm{C}$ [41]. Finally, Q_{m} (W/m^3) is the metabolic heat produced by the tissue, and Q_{ext} (W/m^3) is the heat produced by external sources.

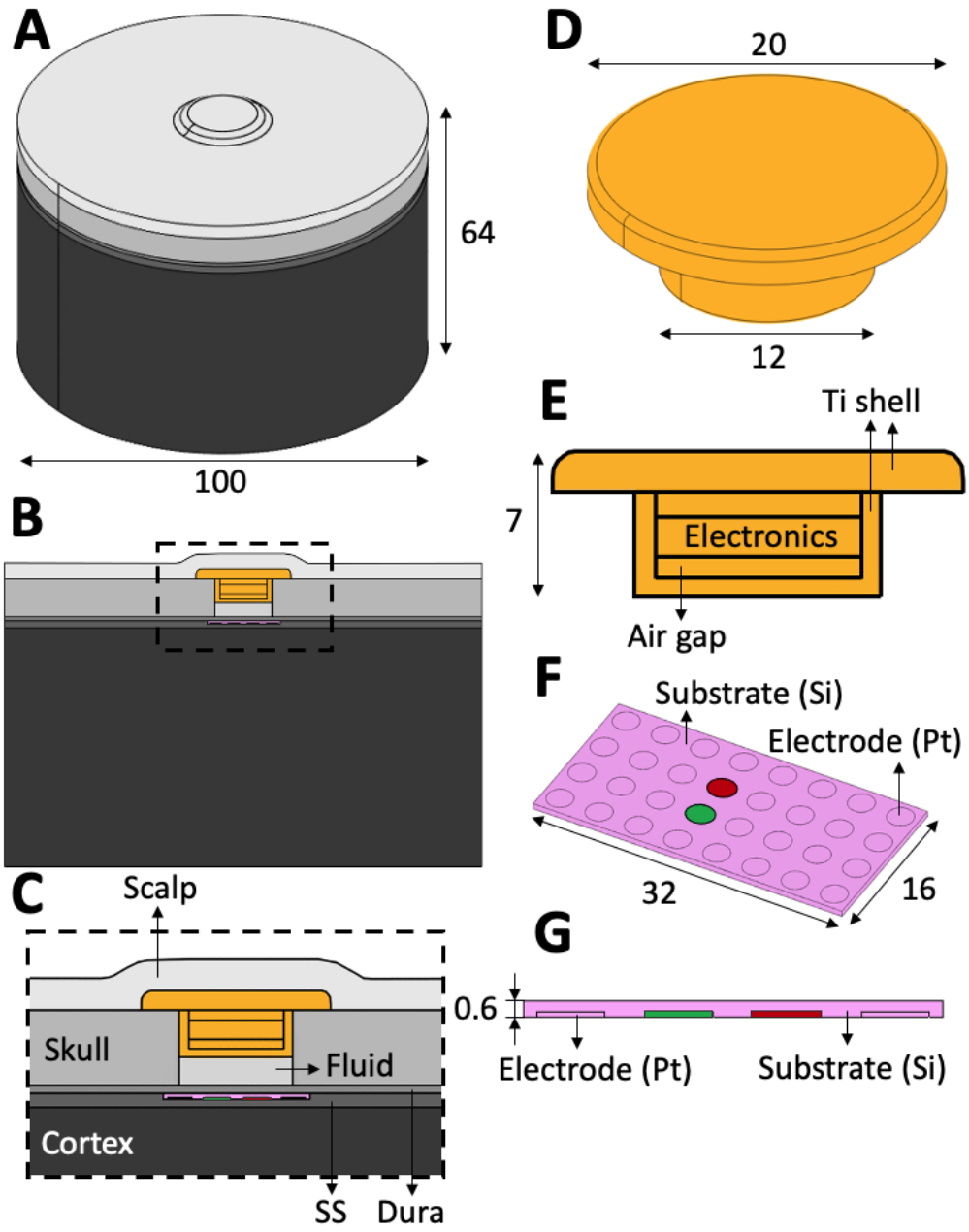


Figure 3.1: Model of the human head, with relevant tissues and implanted components. The dimensions are in mm (cf. Table 3.1 for the thickness of each tissue layer and component). (A) 3D view of the model geometry. (B) Central cross-section of the view in (A). (C) Zoomed-in view of the inset in (B). (D) 3D view of the SU. (E) Central cross-section of the SU. (F) 3D view of the electrode grid. The green and red electrodes indicate the positive and negative stimulating electrodes, respectively. (G) Zoomed-in view of the cross-section of the electrode grid.

Specifically, $Q_{\text{ext}} = Q_{\text{SU}} + Q_{\text{stim}}$, where Q_{SU} is the heat generated by the power dissipation in the SU, and Q_{stim} (W/m^3) is the heat generated by cortical stimulation. Note that

$Q_{\mathrm{SU}} = 0$ everywhere except for the electronics layer, where it is defined as $Q_{\mathrm{SU}} = P_{\mathrm{SU}}/V_{\mathrm{E}}$, where P_{SU} is the SU's power consumption (W) and V_{E} is the electronics layer's volume (m^3). On the other hand, Q_{stim} is proportional to the gradient of the voltage due to electrical stimulation and is calculated using the *electric currents* module (see Section 3.2.2). The software found the steady-state solution of Eq. (3.1) ($\partial T/\partial t = 0$) for each tissue layer and implanted component, with extraneous terms set to 0 and temperature continuity enforced at every layer interface. The thermal parameters for the tissues and implantable components were taken from literature and are shown in Table 3.2. We estimated the scalp, skull, and dura blood perfusion from [218, 57], and [97], respectively. Given that the brain's blood perfusion is highly dependent on activity levels, we used values corresponding to slow walking conditions (80 bpm, 1 mph) [97]. Moreover, we used the tissues' blood perfusion coefficients to derive their metabolic heat values, as described in [142]. For the thermal conductivity of the tissues, we computed the average of the values found in [142, 51, 60, 80, 169]. Similarly, we computed the thermal conductivity of the implantable components as the average of the values found in [167, 12, 107, 190]. Finally, given that the layout of the electronics layer is currently unknown, we assumed its thermal conductivity to be the same as that of the PCB. Note that PCB's multilayered structure causes its thermal conductivity to be anisotropic. Based on our benchtop BCI prototypes [205, 192], we assumed a two-layer PCB and applied the formulas in [155] to obtain $k_{\mathrm{xy}} = 14.2$ W/(m K) and $k_z = 0.3$ W/(m K).

To solve the boundary value problem (3.1), the following boundary conditions were applied. Consistent with [103], we assumed heat to be transferred through free convection at the scalp-air interface:

$$\mathbf{n} \cdot (k \nabla T) = h(T_{\mathrm{ext}} - T) \tag{3.2}$$

Table 3.2: Thermal properties of the tissues and implanted components

	k (W/(m K))	$\rho_b C_b \omega$ (W/(m^3 K))	Q_m (W/m^3)	References
Scalp	0.342	7596	1100	[51, 218]
Skull	0.680	2848	26	[60, 218]
Dura mater	0.440	27253	-	[142, 57]
SS (CSF)	0.570	-	-	[80]
Brain	0.528	37219	10383	[51, 97]
Fluid (Saline)	0.600	-	-	[169]
SU Shell (Ti)	19.000	-	-	[167]
Air gaps	0.030	-	-	[12]
Substrate (Si)	0.200	-	-	[107]
Electrodes (Pt)	71.000	-	-	[190]

where $\mathbf{n}$ is the outward normal vector, h is the heat transfer coefficient (W/(m^2 K)) and T_{ext} is the external air temperature (K). We set $h = 5$ W/(m^2 K) [103], which corresponds to free air flow conditions [108], and $T_{\text{ext}} = 20$°C. For the brain's bottom boundary, we assumed the temperature to be equal to brain core temperature [103, 54], which is usually 0.5°C higher than body core temperature [204] (i.e., $T = 37.5$°C). Finally, the brain's lateral surfaces were assumed to be thermally insulated:

$$\mathbf{n} \cdot (k \nabla T) = 0 \tag{3.3}$$

This assumption is justified given that the distance between this boundary and the SU is sufficiently large so that the thermal effect of the SU's heat sources is negligible.

Electrical Stimulation

To calculate the heat generated from the cortical stimulation, Q_{stim}, we used the Joule heating equation from the *electric currents* COMSOL module:

$$Q_{\text{stim}} = \sigma \| \nabla V \|^2 \tag{3.4}$$

where σ (S/m) is the material's electric conductivity and V (V) is the electric potential at position (x, y, z). To calculate V, COMSOL solves the Laplace equation, $\nabla \cdot (\sigma \nabla V) = 0$, for every tissue layer and implanted component, while enforcing continuity across all layer interfaces. The values of σ for each tissue and component were taken as the averages of the values found in literature and are shown in Table 3.3.

Table 3.3: Electrical conductivity of the tissues and components.

Tissue	σ (S/m)	Ref	Component	σ (S/m)	Ref
Scalp	0.410	[139]	SU shell (Ti)	6.0×10^7	[132]
Skull	0.020	[139]	Air gaps	10^{-14}	[83]
Dura mater	0.461	[139]	Substrate (Si)	10^{-13}	[28]
SS (CSF)	1.710	[139]	Electrodes (Pt)	9.1×10^6	[182]
Brain	0.370	[139]	Electronics (PCB)	10^{-13}	[202]
Fluid (Saline)	3.000	[31]			

To solve the electrical boundary problem (3.4), we used the following boundary conditions. First, to model bipolar cortical stimulation, we set the top boundary, Si-Pt [see Fig. 3.1(G)], of the positive and negative stimulating electrodes to:

$$\begin{aligned} V_{\text{A}} &= V_{\text{stim}} \\ V_{\text{C}} &= -V_{\text{stim}} \end{aligned} \tag{3.5}$$

where the subscripts A and C indicate anode and cathode, respectively. We found $V_{\text{stim}} = 1.1$ V by assuming a worst-case cortical stimulation in terms of heat, with a current amplitude of 3.5 mA, a phase width of 400 μs, and a frequency of 500 Hz. The reasoning behind this

parameter choice and their evaluation can be found in Section 3.2.2. We also assumed all exterior boundaries [see Fig. 3.1(A)] to be electrically insulated:

$$\mathbf{n} \cdot J = 0 \tag{3.6}$$

where J (A/m^2) is the electric current density. This implies that the current density at these boundaries is negligible. This assumption is justified given that most of the current flow is localized to the stimulating electrodes, whose relative distance is much smaller than the distance between these electrodes and the exterior boundaries [54]. Finally, at the electrode-SS boundary, we modeled the contact impedance as:

$$\mathbf{n} \cdot J = \frac{1}{\rho_s} \Delta V \tag{3.7}$$

where ρ_s (Ω m^2) is the boundary's surface resistivity and ΔV (V) is the voltage across the boundary. To determine the value of ρ_s, we first note that the magnitude of the electrode-to-electrode path impedance, Z, after long-term subdural implantation is $\sim$1 kΩ [186]. By exploiting the connection between ρ_s and Z we determined $\rho_s = 2.1 \times 10^{-3}$ Ωm^2. Note that the voltage between the stimulating electrodes of 2.2 V and the impedance $|Z| = 1$ kΩ correspond to a stimulating current of 2.2 mA. A more detailed description of this procedure can be found in Section 3.2.2.

Stimulation Parameters

To model bipolar electrocortical stimulation, we set the electric potential at the top of the anode to $V = V_{\text{stim}}$, and we set the top of the cathode to $V = -V_{\text{stim}}$. Thus, the potential difference between the two electrodes is $\Delta V_{\text{elec}} = 2V_{\text{stim}}$. From Ohm's law, $\Delta V_{\text{elec}} = I|Z|$, where I (A) is the current flowing between the two electrodes, and Z (Ω) is the broadband electrode-to-electrode path impedance. Typically, in cortical stimulation, I is a train of biphasic square pulses (see Fig. 3.2). However, given the stationary nature of our model (see Section 3.2.2), we replaced the effect of I_{stim} (see Fig. 3.2) by its root-mean-square (RMS) value, as is common in similar studies [54]:

$$I = I_{\text{RMS}} \triangleq \sqrt{\frac{1}{T_{\text{p}}} \int_0^{T_{\text{p}}} I_{\text{stim}}^2(t)\, dt} = I_{\text{amp}} \sqrt{2\, f\, W} \tag{3.8}$$

where T_{p} (s) is the period of the pulse train, I_{amp} (A) is the pulse amplitude, $f = 1/T_{\text{p}}$ (Hz) is the pulse train frequency, and W (s) is the phase width of a pulse.

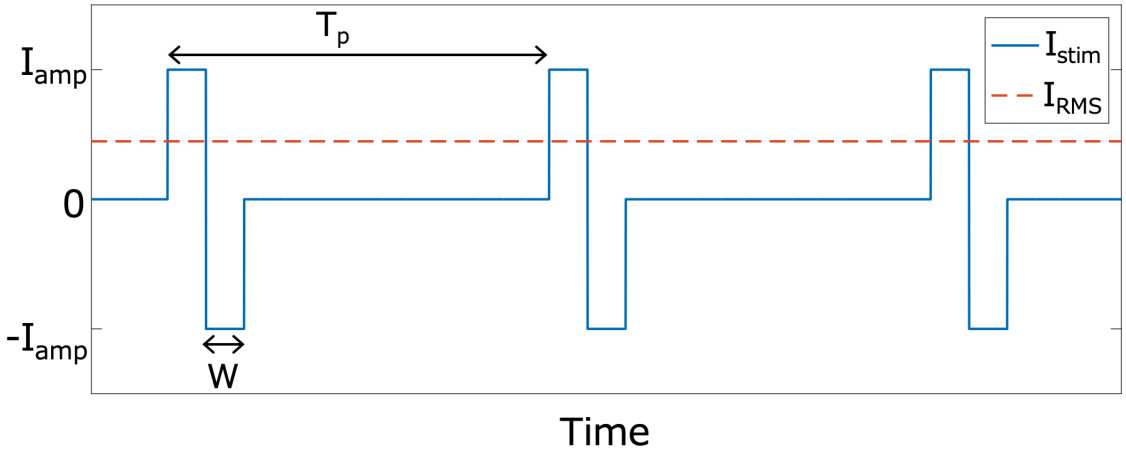


Figure 3.2: Plot of I_{stim}, a biphasic square pulse stimulating current, and I_{RMS}, its corresponding RMS value. T_{p} is the signal's time period and W is the phase width.

Given the high variability of cortical stimulation parameters [84], we selected those that

resulted in the worst-case scenario in terms of heat generation, i.e., the highest value of I_{RMS}. After extensive literature review [125, 117, 105, 27, 1, 37, 84], we found that artificial sensation could be elicited by subdural electrostimulation with activation thresholds ranging from 35 to 700 μC·Hz. To achieve the worst-case scenario of 700 μC·Hz, the study in [84] used $f = 500$ Hz, $I_{\mathrm{amp}} = 3.5$ mA, and $W = 400$ μs. Based on Eq. (3.8), these parameters resulted in $I_{\mathrm{RMS}} = 2.2$ mA (see Table 3.4).

Table 3.4: Combinations of stimulation parameters that result in the same I_{RMS} and in turn the same heat effect.

f (Hz)	I_{amp} (mA)	W (μs)	Activation Threshold† (μC·Hz)	Charge Density‡ (μC/cm^2/phase)	I_{RMS} (mA)
500	3.5	400	700	28.5	2.2
250	7	200	350	28.5	2.2
170	10	140	238	28.5	2.2

†Activation Threshold $= f \times I_{\mathrm{amp}} \times W$.
‡ Charge Density $= I_{\mathrm{amp}} \times W/A$, where A (cm^2) is the exposed electrode area, in our model $A = 4.91 \times 10^{-2}$ cm^2.

Table 3.4 also shows other combinations of stimulation parameters that result in the same value of I_{RMS}, and would, therefore, produce the same heating effect. Note that these parameters are well within the range of values reported in the literature [125, 117, 105, 27, 1, 37, 84]. Also, note that all the combinations of parameters comply with the FDA's charge density safety limit of $\leq$30 μC/cm^2/phase. Finally, to estimate ΔV_{elec}, we assumed that the electrode-to-electrode path impedance is $|Z| = 1$ kΩ. This value is consistent with the range of impedances reported in long-term subdural ECoG studies [186]. Taking $I = 2.2$ mA and $|Z| = 1$ kΩ, we found $\Delta V_{\mathrm{elec}} = 2.2$ V and $V_{\mathrm{stim}} = 1.1$ V.

Contact Impedance

To determine the surface resistivity ρ_s, we iteratively changed its value in COMSOL until the electrode-to-electrode path impedance reached the value of 1 kΩ. Given the value of $\Delta V_{\text{elec}} = 2.2$ V, this condition is equivalent to $I = 2.2$ mA. From Fig. 3.3, we deduce that ρ_s affects the path impedance, i.e., $Z(\rho_s) = f(Z_{\text{E}}, Z_{\text{C}}(\rho_s), Z_{\text{T}})$. However, this function is not explicitly known given the complexity of the multiple current paths. Instead, for a given value of ρ_s, we simulated the model (3.4) with the corresponding boundary conditions (3.5), (3.6), (3.7), and we calculated the total current, $I(\rho_s)$, by integrating the current density over the top surface of either the anode or cathode (they are the same due to current conservation). This process was iteratively repeated until $I(\rho_s^*) = 2.2$ mA, which yielded $\rho_s^* = 2.1{\cdot}10^{-3}$ Ωm^2.

Power Budget Estimation

According to ISO 14708-3 (an FDA's recognized standard), active head implants must not increase the surrounding tissues' temperature beyond 39°C. Assuming a brain core temperature of 37.5°C [41, 204], we conservatively defined the power consumption to be thermally safe if it causes a temperature increase $\leq$1°C in the surrounding tissues. We defined the SU's power budget, $P_{\text{SU}}^{\max}$, as the maximum value of P_{SU} that is thermally safe. To estimate $P_{\text{SU}}^{\max}$, we ran the simulation by computing the steady state solutions of Eqs. (3.1) and (3.4) with the parameters defined in the previous sections. Specifically, we first simulated the effect of an inactive implant, i.e., we ran the simulation with $P_{\text{SU}} = 0$ and $V_{\text{stim}} = 0$, and stored the resulting temperature, $T(0, 0)$, for all tissues. Then, we ran the model with $V_{\text{stim}} = 1.1$ V while iteratively increasing the values of P_{SU} up to 90 mW, with a step size of 10 mW. For each iteration, we used the resulting temperature, $T(P_{\text{SU}}, 1.1)$, to define the temperature increase as $\Delta T(P_{\text{SU}}) = T(P_{\text{SU}}, 1.1) - T(0, 0)$. For the first value of P_{SU} whose ΔT violated the 1°C constraint, we decreased and locally refined P_{SU} with a step size of 1 mW. Finally,

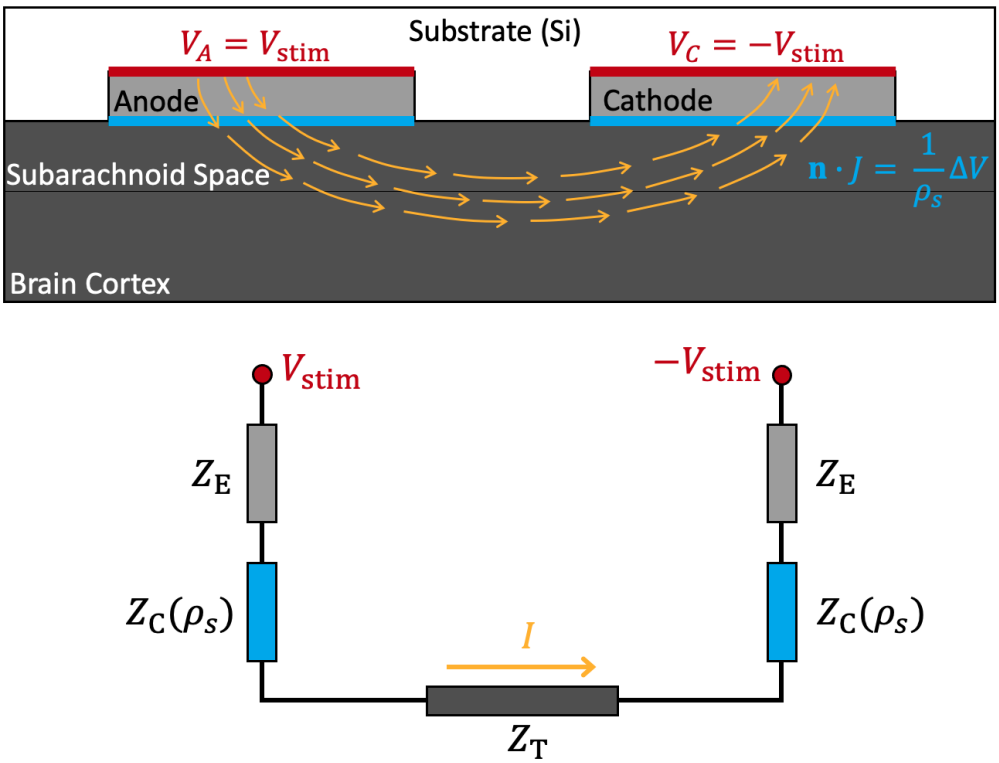


Figure 3.3: (Top) Sketch showing the location of the stimulating electrodes in contact with tissues. The electrodes are represented as light gray boxes with their top and bottom boundaries outlined in red and light blue, respectively. The corresponding boundary conditions are also shown and appropriately color coded. The yellow arrows show hypothetical current paths between the top boundaries of the anode and cathode. (Bottom) Simplified (lumped) circuit model of the above system, where Z_{E} is the electrode impedance, $Z_{\text{C}}(\rho_s)$ is the contact impedance, and Z_{T} is the equivalent impedance of tissues.

we defined $P_{\text{SU}}^{\max}$ as the maximum value that guaranteed $\Delta T(P_{\text{SU}}) \leq 1°\text{C}$, that is:

$$P_{\text{SU}}^{\max} = \underset{P_{\text{SU}} \in [0,90]}{\arg\max} \Delta T(P_{\text{SU}}) : \Delta T(P_{\text{SU}}) \leq 1°\text{C} \tag{3.9}$$

For this model, we refer to all the geometric, thermal, and electrical parameters as nominal parameters.

3.2.3 Sensitivity Analysis

Given that physiological and environmental parameters in our model vary naturally, we performed a sensitivity analysis to test the robustness of our model against these variations. Specifically, we perturbed these parameters within their natural range and quantified the impact of these perturbations on our power budget predictions. It should be noted that we did not perturb the parameters pertaining to the SU (e.g., the thickness of the Ti shell, air gaps and electronics layer), since we assumed its design to be fixed. While optimizing these parameters for power budget purposes is an important problem, it is beyond the scope of this study.

We performed an extensive literature review to determine the range of variation for all the physiological and environmental parameters in our model. We estimated the thickness range for the scalp, skull, dura mater, and SS from [87, 134, 112] and [66], respectively. The thermal conductivity lower and upper bounds for the scalp and brain were estimated from [51], and those of the skull and SS were estimated from [60] and [80], respectively. Since we were unable to find any data on the variation of the dura's thermal conductivity, we estimated its range to be between 90% and 110% of its nominal value, which is based on the average variation of the scalp, skull, SS and brain thermal conductivity. The thermal conductivity range of saline was estimated from [169]. Additionally, we estimated the variation of blood perfusion of the scalp and skull from [218], and that of the dura mater from [57]. The brain's blood perfusion lower bound was estimated from resting values, while the upper bound was estimated from values at double the nominal walking speed (90 bpm, 2 mph) [97]. Analogous to Section 3.2.2, we derived the metabolic heat range of each tissue from its corresponding blood perfusion range. We also estimated the range of T_{ext} and T_{b} from their natural variations. Furthermore, we adopted the range of h for free airflow conditions from [108]. Finally, we estimated the variation of the electrical conductivity of the scalp, skull, SS and brain from [139], and that of saline from [31]. Given the lack of data on the range of the dura's electrical conductivity,

we approximated its relative variation as the average variation of the scalp, skull, SS and brain electrical conductivity.

To quantify the effect of the variation of these parameters on our model, we computed the sensitivity coefficient, S_i [49]. This coefficient quantifies the impact that the perturbation of the parameter θ_i has on the tissues' temperature increase, ΔT:

$$S_i = \frac{\big(\Delta T(P_{\text{SU}}^{\max}, \Theta_i^*) - \Delta T(P_{\text{SU}}^{\max}, \Theta^0)\big)/\Delta T(P_{\text{SU}}^{\max}, \Theta^0)}{\big(\theta_i^* - \theta_i^0\big)/\theta_i^0}, \qquad i = 1, 2, \cdots, 27 \tag{3.10}$$

In this equation, S_i is the ratio of the relative change in temperature and the relative change in the ith parameter. Specifically, $\Delta T(P_{\text{SU}}^{\max}, \Theta^0)$ is the maximum temperature increase across all tissues corresponding to $P_{\text{SU}}^{\max}$ and Θ^0, where $\Theta^0 = [\theta_1^0, \theta_2^0, \cdots, \theta_{27}^0]$ is the vector of the nominal parameters, as shown in Table 3.5. Similarly, $\Delta T(P_{\text{SU}}^{\max}, \Theta_i^*)$ is the maximum temperature increase across all tissues corresponding to $P_{\text{SU}}^{\max}$ and Θ_i^*, where $\Theta_i^* = [\theta_1^0, \cdots, \theta_i^*, \cdots, \theta_{27}^0]$ and θ_i^* is the perturbed value of the ith parameter. Our sensitivity analysis considered both positive ($\theta_i^* = \theta_i^+$) and negative ($\theta_i^* = \theta_i^-$) perturbations, quantified correspondingly by the sensitivity coefficients S_i^+ and S_i^-.

We then labeled as critical those parameters whose perturbation led to $|S_i| \geq 10^{-3}$. In other words, only parameters whose perturbation of 100% would result in $|\Delta T(P_{\text{SU}}^{\max}, \Theta_i^*) - \Delta T(P_{\text{SU}}^{\max}, \Theta^0)| \geq 0.001°\text{C}$ (the model's temperature resolution) were deemed critical. Given that Eq. (3.10) only considers the perturbation of one parameter at a time, we also evaluated the effect of perturbing multiple parameters. Specifically, we simultaneously perturbed all critical parameters and re-estimated the SU's power budget. For the worst-case scenario, we perturbed all critical parameters in the direction that caused an increase in ΔT and, in turn, a decrease in the power budget. Conversely, for the best-case scenario, we perturbed

all critical parameters in the direction that caused a decrease in ΔT and, in turn, an increase in the power budget. Finally, we defined the power budget range as $[P_{\mathrm{SU}}^{\mathrm{WCS}}, P_{\mathrm{SU}}^{\mathrm{BCS}}]$, where $P_{\mathrm{SU}}^{\mathrm{WCS}}$ and $P_{\mathrm{SU}}^{\mathrm{BCS}}$ are the re-estimated power budgets corresponding to the worst-case and best-case scenarios, respectively.

Table 3.5: The nominal values of the physiological and environmental parameters, θ_i^0 , and their negatively and positively perturbed values, θ_i^- and θ_i^+, respectively. l – thickness (mm), k – thermal conductivity (W/(m K)), Q_{m} – metabolic heat (W/m^3), ω – blood flow rate ((ml/s)/ml), T – temperature (°C), h – heat transfer coefficient (W/(m^2 K)), σ – electrical conductivity (S/m).

θ_i	θ_i^0	θ_i^-	θ_i^+
$\theta_1 = l^{\mathrm{scalp}}$	3.35	2.44	4.26
$\theta_2 = l^{\mathrm{skull}}$	7.80	6.22	9.38
$\theta_3 = l^{\mathrm{dura}}$	0.89	0.82	0.96
$\theta_4 = l^{\mathrm{SS}}$	1.43	0.71	2.15
$\theta_5 = k^{\mathrm{scalp}}$	0.36	0.25	0.47
$\theta_6 = k^{\mathrm{skull}}$	0.68	0.67	0.69
$\theta_7 = k^{\mathrm{dura}}$	0.44	0.32	0.56
$\theta_8 = k^{\mathrm{SS}}$	0.57	0.51	0.63
$\theta_9 = k^{\mathrm{brain}}$	0.53	0.51	0.55
$\theta_{10} = k^{\mathrm{fluid}}$	0.60	0.59	0.61
$\theta_{11} = Q_{\mathrm{m}}^{\mathrm{scalp}}$	10039.37	259.84	1125.99
$\theta_{12} = Q_{\mathrm{m}}^{\mathrm{skull}}$	886.12	0.00	1476.87
$\theta_{13} = Q_{\mathrm{m}}^{\mathrm{dura}}$	5997.57	5270.59	6724.55
$\theta_{14} = Q_{\mathrm{m}}^{\mathrm{brain}}$	13275.54	12140.31	14033.77
$\theta_{15} = \omega^{\mathrm{scalp}}$	8431.65	2107.91	91334.29
$\theta_{16} = \omega^{\mathrm{skull}}$	3626.60	0.00	6044.33
$\theta_{17} = \omega^{\mathrm{dura}}$	24546.07	21570.79	27521.35
$\theta_{18} = \omega^{\mathrm{brain}}$	41307.49	37775.18	43666.78
$\theta_{19} = T_{\mathrm{ext}}$	20.00	5.00	35.00
$\theta_{20} = h$	5.00	2.50	25.00
$\theta_{21} = T_{\mathrm{b}}$	37.00	36.50	39.50
$\theta_{22} = \sigma^{\mathrm{scalp}}$	0.41	0.23	0.59
$\theta_{23} = \sigma^{\mathrm{skull}}$	0.02	0.00	0.04
$\theta_{24} = \sigma^{\mathrm{dura}}$	0.46	0.23	0.69
$\theta_{25} = \sigma^{\mathrm{SS}}$	1.71	1.41	2.01
$\theta_{26} = \sigma^{\mathrm{brain}}$	0.37	0.24	0.50
$\theta_{27} = \sigma^{\mathrm{fluid}}$	3.00	1.68	4.32

3.3 Results

3.3.1 Nominal Model

We first found the steady-state solutions of Eqs. (3.1) and (3.4) for an inactive implant ($P_{\mathrm{SU}} = 0$, $V_{\mathrm{stim}} = 0$) using the following COMSOL-defined adaptive mesh sizes: *coarse*, *normal*, *fine*, *finer*, *extra fine*, and *extremely fine*. Simulations at the *coarse* mesh size generally overestimated the temperature, and as we refined the mesh, this temperature bias decreased. The difference in temperature values between the *extra fine* and *extremely fine* mesh sizes was <0.001°C, suggesting that the resulting temperature values had converged. Thus, we selected the *extra fine* mesh for all simulations to balance the model accuracy and computational load. Fig. 3.4 shows the distribution of temperature for the inactive implant scenario. We subsequently simulated the temperature distribution with cortical electrostimulation and different power consumption levels, and estimated the nominal power budget as explained in Section 3.2.2.

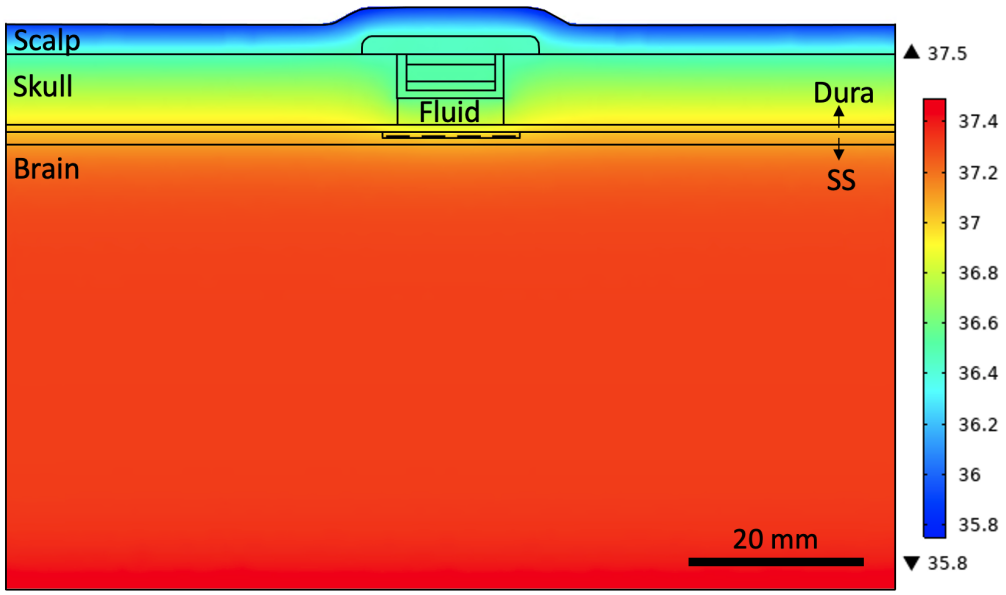


Figure 3.4: The distribution of T (°C) across the central cross-section of the nominal model for an inactive implant ($P_{\mathrm{SU}} = 0$, $V_{\mathrm{stim}} = 0$) calculated using COMSOL-defined *extra fine* mesh size.

Figure 3.5 shows the spatial distribution of simulated ΔT for different power consumption levels. To help in interpreting 3D temperature data, we only show ΔT across the central cross-section of the model [Fig. 3.1(B)], which exhibited the highest temperature increase. As the power consumption increased, the area where $\Delta T > 1$°C (marked by red color) expanded and eventually encroached on the surrounding tissues [Fig 3.5(D)]. Through the iterative procedure described in Section 3.2.2, we found $P_{\mathrm{SU}}^{\mathrm{max}} = 70$ mW, i.e., at this power consumption level all tissues exhibited $\Delta T \leq 1$°C. Figure 3.6 shows the spatial map of $\Delta T(70)$ across the same worst-case cross-section as in Fig. 3.5. We observed that $\Delta T > 1$°C occurred only within the SU. Outside of the SU, the highest local temperature increase occurred in the skull, scalp, and fluid layers. On the other hand, ΔT decreased with the axial distance from the SU, with the dura, SS, and brain tissues exhibiting progressively lower temperature increases. The subtle “hot spots" near the stimulating electrodes are due to the superposition of the heat generated by the SU and cortical electrostimulation. Nonetheless, the nearby brain tissue only experienced a $\Delta T = 0.5$°C, which is comparable to the temperature increases predicted by the FEM models of thermal impact due to DBS [54, 53]. Our analysis also showed that the contribution of electrostimulation alone with the worst-case stimulation parameters (see Section 3.2.2) was $\Delta T \approx 0.4$°C. As expected, this temperature increase was localized to the SS, in the immediate vicinity of the stimulating electrodes.

Figure 3.7 shows the spatial distribution of the electric potentials due to cortical electrostimulation. It also displays the electric current density, which shows the current flowing from the anode to the cathode. As expected, the potential field exhibits dipole-like properties [125], with most of the space being electrically neutral, except in the immediate vicinity of the stimulating electrodes. Note that the current flow is also restricted to this area, with the current density reaching the highest magnitude at the anode and cathode surfaces.

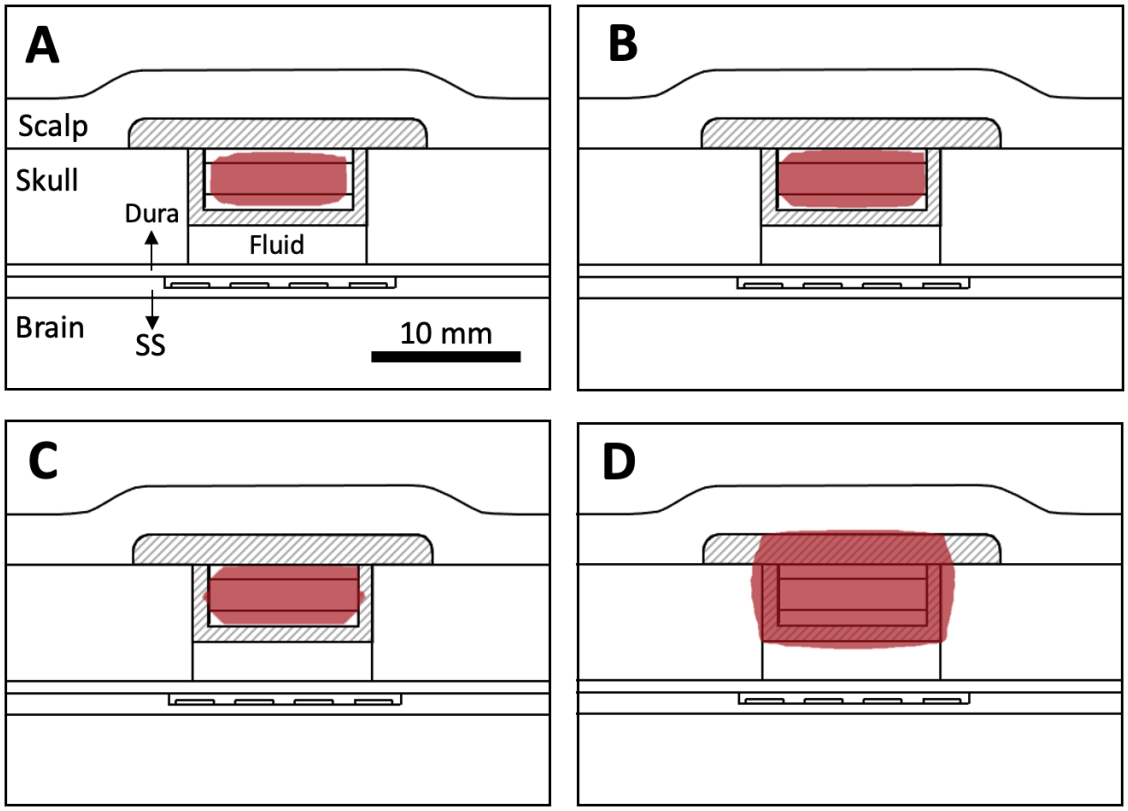


Figure 3.5: The distribution of $\Delta T(P_{\mathrm{SU}})$ across the central cross-section of the model for different P_{SU} levels. The areas where $\Delta T > 1°\mathrm{C}$ are colored in red (for all other areas $\Delta T \leq 1°\mathrm{C}$). The SU's Ti shell is shaded in a striped pattern for visualization purposes. (A) 50 mW (B) 60 mW (C) 70 mW (D) 80 mW.

3.3.2 Sensitivity Analysis

We individually perturbed the 27 physiological and environmental parameters within their natural range (see Table 3.5). We calculated the sensitivity coefficients, S_i, according to Eq. (3.10), and their values are shown in Table 3.6. According to the criteria $|S_i| > 10^{-3}$, we identified 17 critical parameters. They include the thickness of most tissues, all the thermal conductivity and blood perfusion parameters, the heat transfer coefficient, h, and the electrical conductivity of the SS and brain. On the other hand, the perturbation of the remaining 10 non-critical parameters did not have a significant impact on simulated temperatures. To further quantify the impact of the parameters' variations, we perturbed all 17 critical parameters simultaneously. As explained in Section 3.2.3, we then defined a

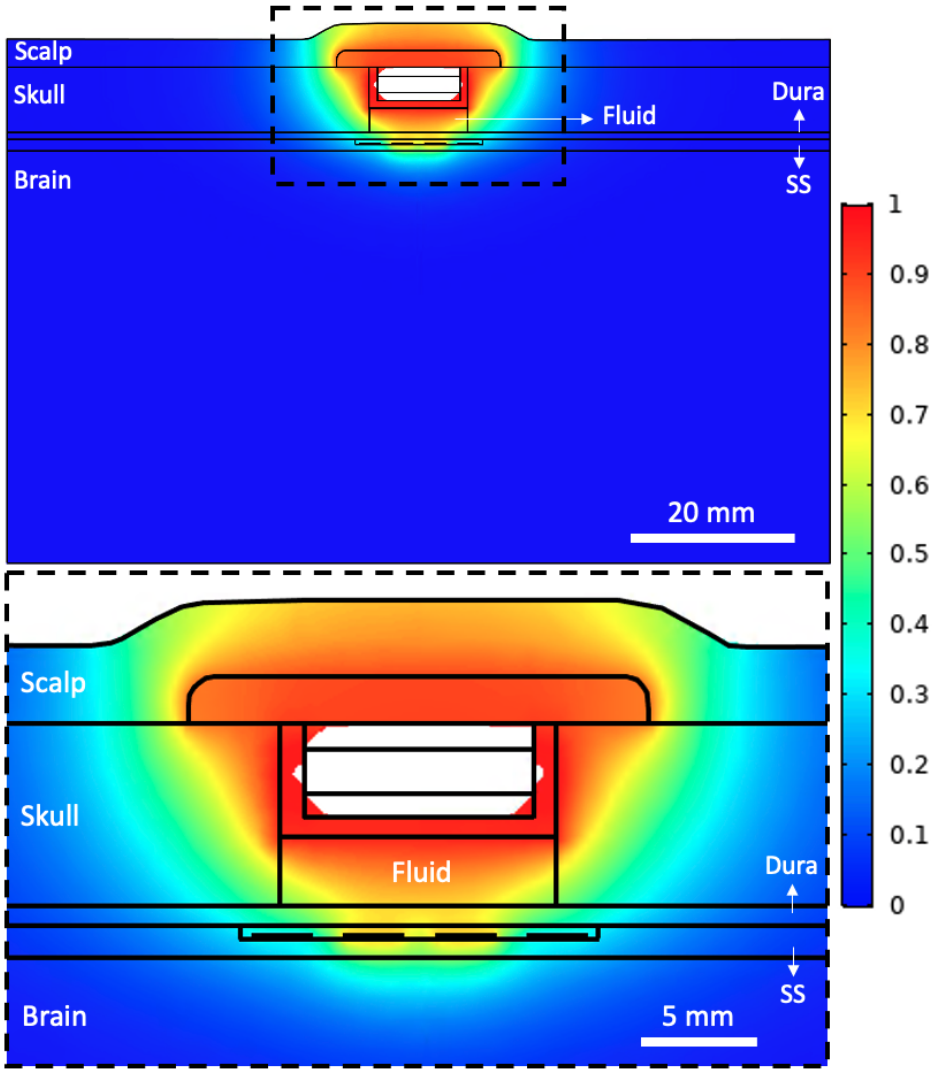


Figure 3.6: $\Delta T(70\text{ mW})$ in °C across the central (worst-case) cross-section of the model. For a better color resolution, we limited the color to $0°\text{C} \leq \Delta T \leq 1°\text{C}$. (Top) View of the overall 2D cross-section. (Bottom) Zoom-in of the top inset.

power budget range, $[P_{\text{SU}}^{\text{WCS}}, P_{\text{SU}}^{\text{BCS}}]$, based on the worst- and best-case scenarios. Specifically, we found that the power budget ranged from 47 to 81 mW.

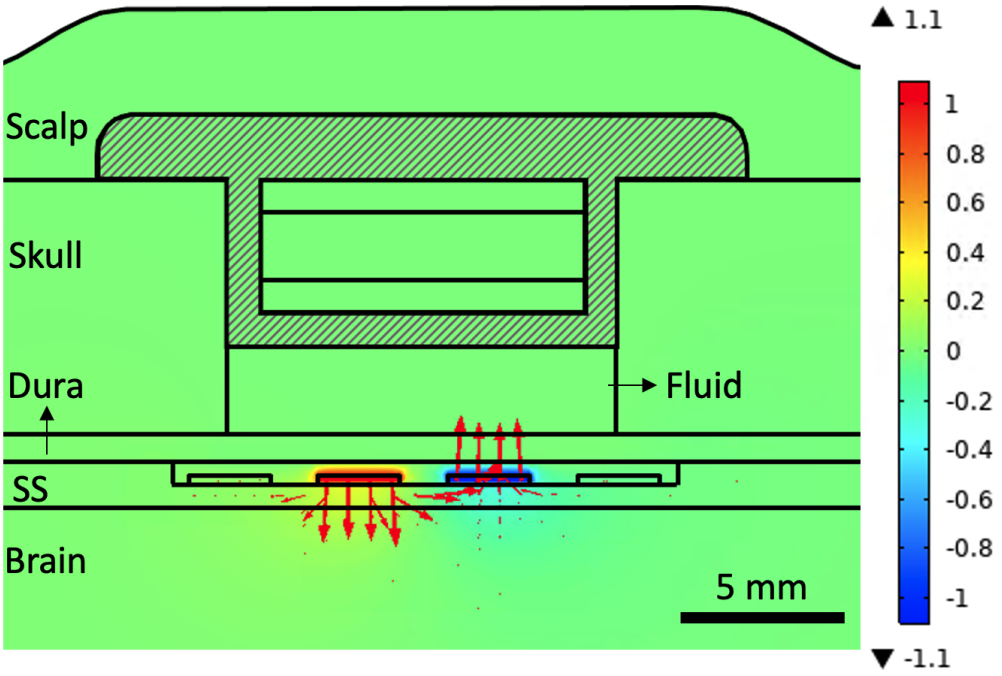


Figure 3.7: The spatial distribution of the electric potential (V) across the central cross-section of the model in response to $V_{\mathrm{A}} = V_{\mathrm{stim}}$ and $V_{\mathrm{C}} = -V_{\mathrm{stim}}$ ($V_{\mathrm{stim}} = 1.1$ V). Arrows represent the electric current density, with the length proportional to the current density magnitude. When integrated over the anode or cathode surface, the total current is 2.2 mA (see Section 3.2.2). The SU's Ti shell is shaded in a striped pattern for visualization purposes.

3.4 Discussion

Based on our simulations, we predicted that the SU could nominally consume up to 70 mW of power without increasing the surrounding tissues' temperature by more than 1°C. When considering the natural variations of the physiological and environmental parameters, the power budget estimate ranged between 47 and 81 mW. This result is consistent with our preliminary study [181], which estimated the nominal SU power budget at 75 mW. Note that this preliminary model lacked cortical stimulation, which in turn lowers the overall heat and overestimates the power budget. Also, unlike the current model, it lacked the dura mater, assumed a partial-thickness craniectomy, and did not consider the natural variations of the physiological and environmental parameters. Even in the worst-case scenario, the estimated power budget of 47 mW should be sufficient to sustain all the envisioned functionalities of the

Table 3.6: The nominal values of parameters, θ_i, and the sensitivity coefficients associated with their positive and negative perturbations, S_i^+ and S_i^-, respectively. The critical parameters are highlighted in grey. l – thickness, k – thermal conductivity, Q_{m} – metabolic heat, ω – blood flow rate, T – temperature, h – heat transfer coefficient, σ – electrical conductivity.

θ_i	S_i^-	S_i^+
$\theta_1 = l^{\mathrm{scalp}}$	$-1.82 \cdot 10^{-1}$	$-1.32 \cdot 10^{-2}$
$\theta_2 = l^{\mathrm{skull}}$	$6.74 \cdot 10^{-2}$	$5.18 \cdot 10^{-2}$
$\theta_3 = l^{\mathrm{dura}}$	$-9.32 \cdot 10^{-3}$	$-9.01 \cdot 10^{-3}$
$\theta_4 = l^{\mathrm{SS}}$	$3.42 \cdot 10^{-2}$	$2.28 \cdot 10^{-2}$
$\theta_5 = k^{\mathrm{scalp}}$	$-1.35 \cdot 10^{-1}$	$-1.08 \cdot 10^{-1}$
$\theta_6 = k^{\mathrm{skull}}$	$-3.82 \cdot 10^{-1}$	$-3.77 \cdot 10^{-1}$
$\theta_7 = k^{\mathrm{dura}}$	$-8.64 \cdot 10^{-2}$	$-5.72 \cdot 10^{-2}$
$\theta_8 = k^{\mathrm{SS}}$	$-2.43 \cdot 10^{-2}$	$-2.07 \cdot 10^{-2}$
$\theta_9 = k^{\mathrm{brain}}$	$-3.63 \cdot 10^{-2}$	$-3.48 \cdot 10^{-2}$
$\theta_{10} = k^{\mathrm{fluid}}$	$-5.07 \cdot 10^{-2}$	$-4.99 \cdot 10^{-2}$
$\theta_{11} = Q_{\mathrm{m}}^{\mathrm{scalp}}$	$-1.33 \cdot 10^{-8}$	$-1.37 \cdot 10^{-8}$
$\theta_{12} = Q_{\mathrm{m}}^{\mathrm{skull}}$	$-2.67 \cdot 10^{-8}$	$-3.15 \cdot 10^{-8}$
$\theta_{13} = Q_{\mathrm{m}}^{\mathrm{dura}}$	$-8.72 \cdot 10^{-9}$	$-9.02 \cdot 10^{-9}$
$\theta_{14} = Q_{\mathrm{m}}^{\mathrm{brain}}$	$-5.53 \cdot 10^{-7}$	$-5.75 \cdot 10^{-7}$
$\theta_{15} = \omega^{\mathrm{scalp}}$	$-1.51 \cdot 10^{-1}$	$-1.19 \cdot 10^{-1}$
$\theta_{16} = \omega^{\mathrm{skull}}$	$-7.23 \cdot 10^{-2}$	$-5.86 \cdot 10^{-2}$
$\theta_{17} = \omega^{\mathrm{dura}}$	$-2.64 \cdot 10^{-2}$	$-2.57 \cdot 10^{-2}$
$\theta_{18} = \omega^{\mathrm{brain}}$	$-2.99 \cdot 10^{-2}$	$-2.77 \cdot 10^{-2}$
$\theta_{19} = T_{\mathrm{ext}}$	$3.07 \cdot 10^{-8}$	$3.65 \cdot 10^{-7}$
$\theta_{20} = h$	$-1.88 \cdot 10^{-2}$	$-1.41 \cdot 10^{-2}$
$\theta_{21} = T_{\mathrm{b}}$	$-2.84 \cdot 10^{-5}$	$-1.46 \cdot 10^{-5}$
$\theta_{22} = \sigma^{\mathrm{scalp}}$	$1.16 \cdot 10^{-6}$	$-6.34 \cdot 10^{-9}$
$\theta_{23} = \sigma^{\mathrm{skull}}$	$5.19 \cdot 10^{-6}$	$3.80 \cdot 10^{-6}$
$\theta_{24} = \sigma^{\mathrm{dura}}$	$2.43 \cdot 10^{-5}$	$1.77 \cdot 10^{-5}$
$\theta_{25} = \sigma^{\mathrm{SS}}$	$5.63 \cdot 10^{-3}$	$4.51 \cdot 10^{-3}$
$\theta_{26} = \sigma^{\mathrm{brain}}$	$1.06 \cdot 10^{-3}$	$8.88 \cdot 10^{-4}$
$\theta_{27} = \sigma^{\mathrm{fluid}}$	$1.65 \cdot 10^{-6}$	$-2.05 \cdot 10^{-7}$

SU including amplification, serialization, and A/D conversion of the neural signals, as well as control of cortical stimulation. For example, based on our fully-implantable BCI prototypes [205, 192], that use off-the-shelf ICs, we can estimate that amplification, serialization, and A/D conversion (the most power-hungry operations) consume at most 37.3 mW [92].

Our model makes several simplifying assumptions. First, we did not model the effect of the

arachnoid and pia mater. Note these tissues are typically excluded from bio-heat models [103, 90, 102] because they are very thin and do not have a significant thermal impact. Also, we did not separate white and grey matter; instead, we modeled the brain as a homogeneous layer. Note however that this is not critical, given that the hottest region in the cortex is well below the 1°C threshold (see Fig. 3.6). Similarly, we did not model the effect of hair due to its geometric complexity and high variability. Instead, we simulated our nominal model with the addition of a 1-cm thick wool layer on top of the scalp, similar to a hat or wig. We found these results to be indistinguishable from those corresponding to the nominal model, suggesting that the effect of hair is negligible. Note that because the wool thermal conductivity [225] is lower than that of hair [127], wool creates a less favorable condition in terms of heat accumulation and is, therefore, an appropriate surrogate for hair. Additionally, we assumed the thermal properties of the electronics layer to be the same as those of the PCB. A more detailed approach would be to separate the electronics layer into the PCB and supporting ICs, e.g., amplifier array, stimulator array, impedance monitor, and charge monitor [192]. Instead, we accounted for the size of these ICs and the PCB by adjusting the overall volume of the electronics layer, V_{E}. Moreover, the IC components mostly consist of epoxy composites with similar thermal and electrical properties to those of the PCB [149]. This further justifies modeling the electronic components of the SU as a single anisotropic layer. While our envisioned BD-BCI system (Fig. 1.6) will include both a recording and stimulating grid, we only included the latter in our model. Since the recording grid does not produce any appreciable heat, its effect on our power budget predictions is negligible. We also omitted the cables connecting the grids to the SU. This assumption is justified given their high electrical conductivity and negligible heat loss. Also, we did not simulate the potential perfusion effect of CSF since we could not find any data on the volumetric flow rate of CSF in the SS. Note, however, that perfusion would help further reduce the temperature increase, and, thus, increase the power budget. Therefore, our assumption results in a more conservative power budget estimate. Similar to other COMSOL-based bio-

heat studies [103, 54, 116], we omitted radiative heat transfer because its effect is considered insignificant [2].

Our results represent a conservative estimate of the SU power budget. Specifically, with our safety threshold of $\Delta T \leq 1$°C with respect to an inactive implant, the SU surface temperature reached at most 37.5°C at the nominal power consumption level of 70 mW. This is significantly lower than the FDA guidelines that limit the surface temperature of neural implants to 39°C. Note however, that the temperature of the skull and scalp in contact with the unpowered SU ranges from 36.4°C to 36.6°C (see Fig. 3.4). Therefore, heating the SU surface to the FDA limit would cause a local temperature rise in excess of 2°C. While not necessarily necrotic, temperature increases above 1°C could have a negative physiological impact [54], especially for the brain tissue [67, 106]. Moreover, our model assumed the SU implanted directly above the stimulating electrodes. This configuration results in a worst-case scenario due to the superposition of the heat generated by the SU and stimulating electrodes. In practice, the SU could be implanted further away from the grid, although the exact location of both components will depend on the individual's head anatomy. Additionally, we chose the cortical stimulation parameters to simulate the worst-case scenario in terms of generated heat (see Section 3.2.2). In practice, it is likely that a combination of parameters will be used that produces a lower stimulation current than the value used in this study, $I_{\mathrm{RMS}} = 2.2$ mA. For example, based on the stimulation parameters in [125, 117, 105, 27, 1, 37] we estimate that I_{RMS} ranges from 0.5 mA to 1.6 mA. This would, in turn, result in less heat generation due to cortical stimulation and would free up additional power to be expended by the SU. Finally, exposing tissues to long-term heat can trigger adaptation mechanisms such as angiogenesis [39], which increases blood perfusion and, in turn, takes heat away. However, we did not incorporate this phenomenon into our model.

Our FEM approach to modeling the thermal effect of active implants was validated in our

ongoing study [180]. There we showed that the simulated thermal behavior of the CWU closely matched experimental measurements collected from a CWU benchtop prototype. Nevertheless, to ultimately ensure the thermal safety of any active implant, including the SU in this study, long-term *in vivo* testing must be performed. Thus, our future work will focus on the completion of the BD-BCI design and fabrication of the implantable CWU and SU prototypes, followed by their surgical implantation and *in vivo* validation in a large animal model. Specifically, upon implantation, the CWU and SU will be set to execute the expected BD-BCI functions, while their surface temperatures will be measured by a thermocouple. The temperature measurements could be monitored over time by exploiting the wireless communication capabilities of our CWU prototypes [205, 192].

Our simulation approach and sensitivity analysis are also applicable to other active head implants, not only in the BCI domain, but also for other applications. Importantly, our approach is reproducible and the same steps can be followed in simulating the thermal impact of active implants to estimate their safe power budget.

3.5 Conclusion

To the best of our knowledge, this study, together with the CWU study in Chapter 2, is the first thermal impact analysis of a fully-implantable BD-BCI. In this chapter, we estimated the SU's maximum power budget that guarantees a thermally safe operation. Specifically, we found that a nominal power consumption of 70 mW would not lead to an increase of the surrounding tissues' temperature by more than 1°C, which satisfies the FDA guidelines (ISO 14708-3). Furthermore, we performed a sensitivity analysis to identify physiological and environmental parameters that are critical for the power budget estimation. We then varied these parameters over their natural range, and found the power budget estimate to range between 47 and 81 mW. These power budget estimates provide an important specification

for the design of our fully implantable BD-BCI system. Finally, our future research efforts will be directed toward performing *in vivo* animal studies to validate our power budget predictions for the SU and CWU.

Chapter 4

ECoG-based Step Decoder

4.1 Motivation

When designing our BD-BCI prototype, we repurposed an existing EEG-based decoder [210] and implemented it as an ECoG-based decoder in our BD-BCI system. This decoder distinguished between idle and move states during walking with a very high accuracy. However, because EEG signals only contain frequencies < 40 Hz, this decoder did not exploit the motor information present in the higher frequencies of ECoG recordings. Thus, this decoder could not be used to decode any walking information other than the overall state. For this reason, we saw the design of the CWU and SU implantable prototypes as an opportunity to improve upon the existing decoder.

Our group previously characterized the electrophysiological activity of the leg motor areas of human subjects performing various gait-related tasks [140]. Specifically, we used high-density subdural ECoG grids [206], implanted unilaterally over the paracentral lobule to measure the activity of the primary and supplementary leg motor areas. In response to treadmill walking, these cortical areas exhibited generalized γ-band synchronization and γ-

band power bursts that were phase-locked with each stride. These findings were then used to design a frequency-domain decoder capable of predicting both the walking states and step rates [209]. While it achieved unprecedented offline accuracy, this decoder imposed a significant lag on the decoded parameters which limits its real-time deployment.

In this study, we seek to develop an ECoG-based decoder for individual walking steps that conforms to low-power and real-time implementation requirements. To that end, we designed a decoding framework based on a Fokker-Planck-based Bayesian filter. We also validated the performance of this decoder using ECoG signals recorded from the motor cortices of two human subjects as they performed multiple walking tasks on a treadmill.

4.2 Methods

4.2.1 Data Collection

A detailed account of the experimental procedures was previously provided in [140]. Briefly, the study was approved by the Institutional Review Boards of the University of California, Irvine and the Rancho Los Amigos National Rehabilitation Center. Participants were recruited from a pool of able-bodied individuals who were implanted with subdural ECoG grids for epilepsy surgery evaluation. We only recruited subjects who had the coverage of the leg motor areas. To minimize the risks of seizures, the experiments (summarized below) were performed after the subjects had resumed taking their antiepileptic medications.

To determine the location the ECoG grids, we first generated a 3D rendering of the T1 post-implantation magnetic resonance imaging (MRI) sequence. We then used the prominent electrode artifacts in the MRI to annotate individual electrodes [79]. Finally, we used anatomical landmarks such as the central sulcus, precentral sulcus and cingulate sulcus to

delineate the primary motor cortex (M1) and the supplementary motor area (SMA).

Subject were placed on a treadmill and instructed to perform different walking tasks while we simultaneously recorded their ECoG and kinematics data (see Fig. 4.1). For the ECoG data, we recorded up to 32 channels using NeXus-32 bioamplifier (Mind Media, Herten, Netherlands) at 2048 Hz, and with a built-in 553 Hz low-pass filter. For the kinematics data, we recorded movement trajectories using L3GD20 gyroscopes (STMicroelectronics, Geneva, Switzerland) mounted on the subjects' distal femur and distal tibia. The gyroscopes measured hip and knee trajectories on the side contralateral to the ECoG grid. We acquired trajectory data at 256 Hz with an integrated Arduino microcontroller (Arduino, Turin, Italy). The ECoG and trajectory data were synchronized using a common pulse train sent to the bioamplifier and microcontroller systems.

The participants performed two different walking tasks on a treadmill with a 0% weight-support harness to prevent falls (Fig. 4.1). In the first task, subjects alternated between idling (6 intervals, $\sim$ 30 s) and walking at a constant casual speed (5 intervals, $\sim$ 30 s). The casual speed was empirically selected for each participant to maximize comfort. We refer to this task as the constant-speed task (Fig. 4.1). In the second task, subjects walked at the following speeds (30 s intervals each): casual, fast, casual, slow, casual, fast, casual, slow, casual. The slow and fast speeds were 50% and 150% of the casual speed, respectively. The subjects stood idle for $\sim$ 30 s before the first, and after the last, walking intervals. We refer to this as the variable-speed task (Fig. 4.1). Further details on the study and experimental design are presented in [140].

4.2.2 Decoder Overview

We developed an algorithm to decode individual steps from recorded ECoG signals. Only signals from the electrodes located in the primary motor cortex (M1) or supplementary



Figure 4.1: (Top) Overview of the experimental setup.Participants walked on a treadmill while being placed in a 0% weight-support harness to prevent falls. Their ECoG signals were recorded with a bio-amplifier system and their leg trajectories were measured using gyroscopes mounted on the distal femur (not visible) and distal tibia. (Bottom) Treadmill walking speed during the two experimental tasks.In the constant-speed task, the participants alternated between epochs of idling and walking at casual speed. The variable-speed task consisted of walking epochs at three speeds (slow, casual, fast), and the initial and final idling epochs. Each epoch lasted ∼30 s with the overall task duration of ∼5.5 min.

motor area (SMA) were used to train the decoder. Overall, the decoder includes two main steps, a feature extraction step, based on logistic regressions, followed by a Fokker-Planck-based Bayesian filter step (Fig. 4.2). In the feature extraction, multi-channel ECoG data is transformed into a single feature that represents the probability of a step occurring. Ideally, during a step (leg swing), the extracted feature should approach 1, and in the off-cycle (no swing), the feature should fall back to 0. In reality, the extracted feature is more ambiguous and, thus, a filtering step is required.

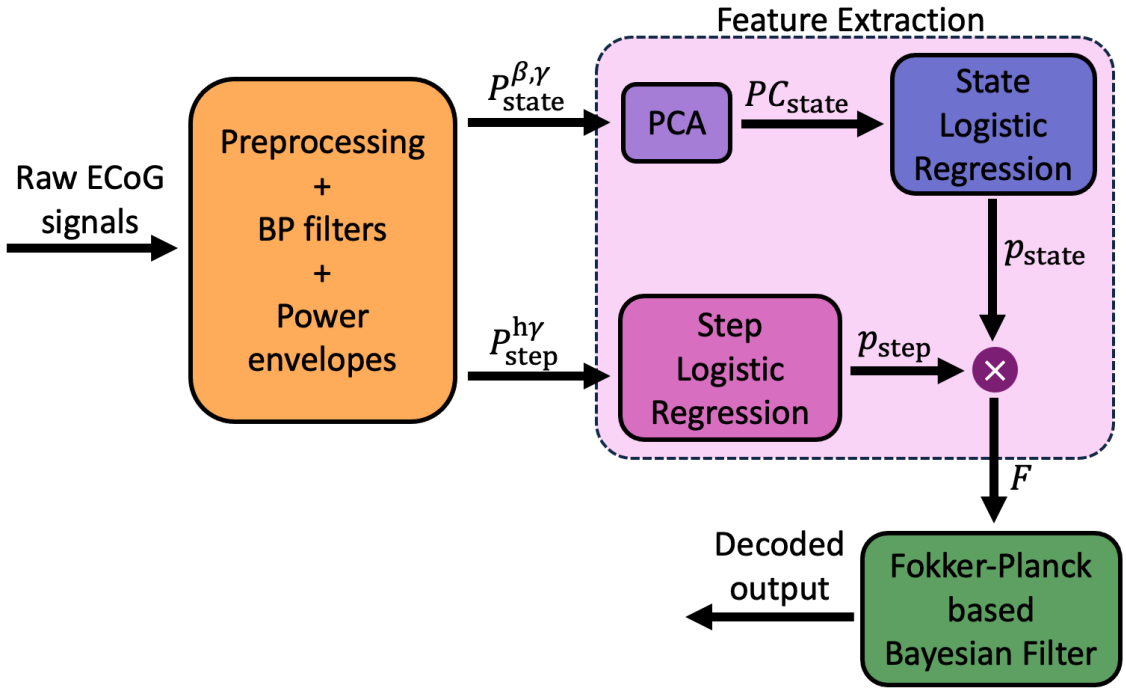


Figure 4.2: Pipeline of the proposed decoder. Raw ECoG signals are preprocessed and band-pass filtered. The resulting signals input into a logistic regression-based feature extraction algorithm. For the state signal, principal component analysis (PCA) is implemented before the logistic regression. The state and step logistic regression outputs are multiplied to create the extracted feature, f. The final step is a Fokker-Planck-based Bayesian filter, whose input is f and output is the decoded walking steps.

The decoder uses ECoG data from frequency bands that contain physiological modulation. Previous EEG studies have found event-related desynchronization (ERD) in the β band (20-40 Hz) during walking tasks [217]. Additionally, in our ECoG studies, we found event-related synchronization (ERS) in the γ band (40-160 Hz) during walking [140]. Therefore,

we implemented a state logistic regression using data from the β and γ to differentiate between walking states (idle/move). Specifically, this state logistic regression estimates the probability of the move state. Additionally, researchers have shown that bursts in M1 γ band activity were time-locked to individual steps (step cycle) [140]. We have found that this is further accentuated for high-γ (80 - 160 Hz). Thus, we implemented a logistic regression using high-γ data to decode individual steps. Specifically, this step logistic regression estimates the probability of an individual step occurring. Finally, the decoder's extracted feature is the product of the two logistic regression outputs (state and step). Note that this hybrid decoding approach, in our case using two separate logistic regressions, is a commonly used technique that can improve the decoding accuracy [223, 88].

To train and test our decoder, we defined the *ground truth* using the tibial gyroscope signals. To quantify the overall performance of our decoder, we trained and tested the decoder in a leave-one-out cross-validation fashion. Specifically, we initially defined the first 5 s of the experimental data as testing data and the remaining data as training data. Next, we trained and tested the decoder using these split data sets, and we stored the decoded output (5-s binary time series representing step/no step). We iteratively repeated this process using the next 5 s as testing data and redefining the training data accordingly, until all data had been tested. We concatenated all decoded output segments and compared it against the ground truth data (gyroscope).

4.2.3 Decoder Training

Preprocessing

For the ECoG data, we first applied a high-pass filter (0.05 Hz cutoff) to remove the DC component and slow frequency drifts. We also applied two stopband filters (57–63 Hz and 117–123 Hz) to remove line noise and its first harmonic.

For the tibial gyroscope data, we first applied a bandpass filter (0.15 - 1.5 Hz) to suppress artifacts unrelated to stepping. Note that this range of stride frequencies corresponds to 0.3 to 3 steps/s. Assuming an average step length of 0.728 m [178], this translates into a wide range of walking speeds from 0.2 to 2.2 m/s. Subsequently, we isolated leg swings by setting to 0 all the samples corresponding to negative (angular) velocities (see Fig. 4.3). Next, we normalized the leg swing time series by dividing each leg swing cycle by its maximum value. We then binarized these data to obtain the ground truth signal for individual steps, namely $G_{\text{step}} \in \mathbb{R}^{1\times n}$, where n is the length of the gyroscope time series. Since $G_{\text{step}} = 1$ during leg swings and 0 otherwise, this time series can be interpreted as a probability of leg swing. We similarly defined the ground truth signal for walking states, $G_{\text{state}} \in \mathbb{R}^{1\times n}$, with $G_{\text{state}} = 0$ corresponding to idle states (treadmill speed = 0) and $G_{\text{state}} = 1$ corresponding to move states.

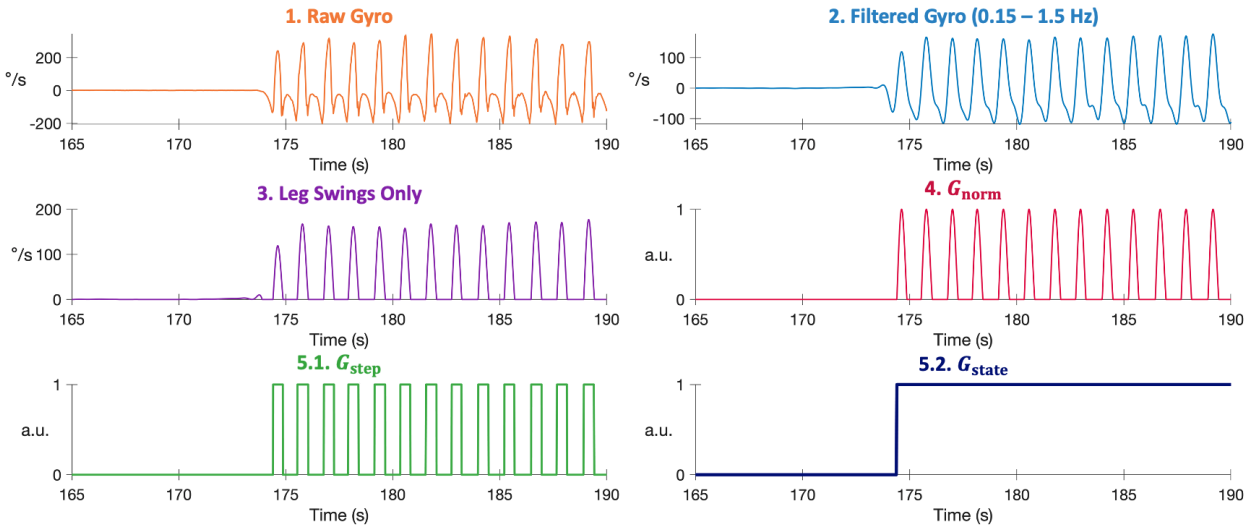


Figure 4.3: Example of the preprocessing steps for a tibial gyroscope signal. The raw signal was bandpass filtered to retain only frequencies related to the stepping rate. We set to 0 all negative values, thus retaining leg swings only. Then, to compute G_{norm} we normalized each peak (i.e., swing) by dividing its magnitude by its height. Then, we computed G_{step} as a binary signal that is 1 during leg swings (when $G_{\text{norm}} > 0$) and 0 otherwise (when $G_{\text{norm}} < 0$). Similarly, G_{state} is a binary signals that is 0 during idling and 1 during walking.

Power Envelopes

To extract motor-modulated signals from the preprocessed ECoG data, we applied bandpass filters corresponding to the following physiological frequency bands: β (20-40 Hz), γ (40-160 Hz), and hγ (80-160 Hz). Then, we squared the data to get the instantaneous power (see Fig. 4.4). Next, we computed the power envelope matrices $P_\beta, P_\gamma, P_{\mathrm{h}\gamma} \in \mathbb{R}^{m \times N}$, where N is the time length of the ECoG data at 2048 Hz, and m is the number of ECoG channels used. Specifically, to compute P_β and P_γ, we used a low-pass filter (0.12 Hz cutoff), and to compute $P_{\mathrm{h}\gamma}$, we used a bandpass filter (0.15-1.5 Hz) that rejected frequencies outside the stepping rate range. Then, we used an anti-aliasing filter to down-sample the power envelopes to 256 Hz, so that they matched the gyroscope's sampling frequency, i.e., $P'_\beta, P'_\gamma, P'_{\mathrm{h}\gamma} \in \mathbb{R}^{m \times n}$, where $n = N \times 256/2048$.

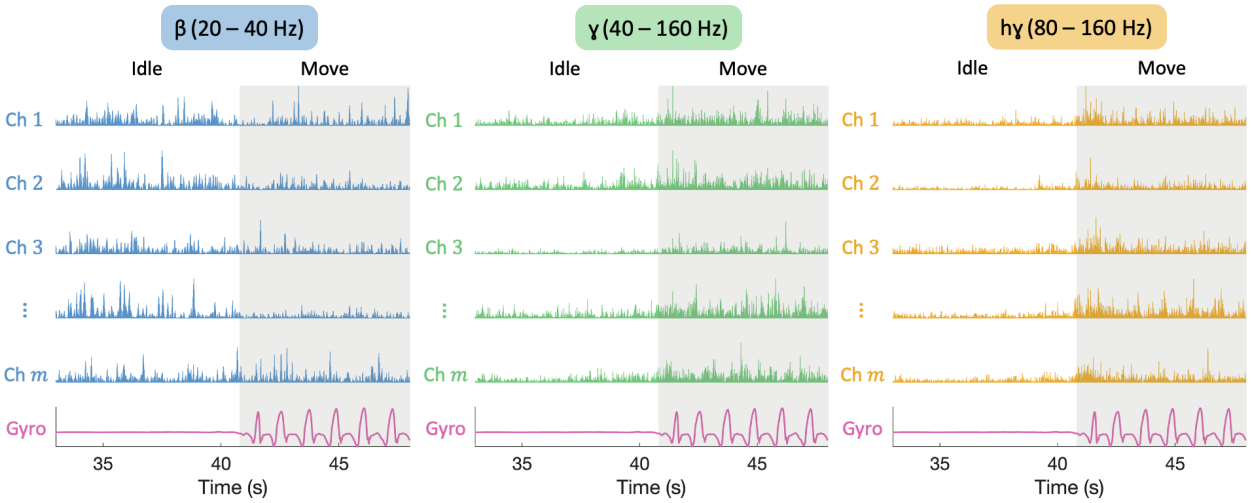


Figure 4.4: Plot of the instantaneous power of different frequency bands from multi-channel ECoG signals during an idle-move transition. The instantaneous power signals were obtained by bandpassing raw ECoG data to the specified frequency bands and then squaring it. The bottom red signal is raw gyroscope data from the contralateral tibia. The white and green background represent idle and move states, respectively.

Feature Extraction

For state decoding, we used the power envelopes $P_{\text{state}} = [P'_{\beta}, P'_{\gamma}] \in \mathbb{R}^{2m \times n}$. On the other hand, for step decoding, we used the power envelopes $P_{\text{step}} = P_{\text{h}\gamma} \in \mathbb{R}^{m \times n}$. Before implementing logistic regressions, we had to ensure that there was no multicollinearity among the independent variables (i.e., P_{state} and P_{step}). To quantify multicollinearity in our data, we computed the Variance Inflation Factor (VIF) for each power envelope in P_{state} and P_{step}. Given m independent variables, $X = [X_1, X_2, \ldots, X_i, \ldots, X_m] \in \mathbb{R}^{m \times n}$, to compute VIF_i we first have to perform the regression $X_i = b_0 + b_1 X_1 + b_2 X_2 + \ldots + b_m X_m + e$. Then, we compute VIF_i as:

$$\text{VIF}_i = \frac{1}{1 - R_i^2} \tag{4.1}$$

where $R_i \in \mathbb{R}^{1 \times 1}$ is the coefficient of determination of the regression. This computation is repeated for all the independent variables in X. The VIF cutoff value is usually considered to be between 5 and 10 [193]. VIF values above this cutoff indicate high multicollinearity in the data, which can lead to unstable estimates in a logistic regression. We computed the VIF for each envelope in P_{state} and found that, on average, $\text{VIF}_i > 10$, thus, indiciating high multicollinearity in the data. We also computed the VIF for each envelope in P_{step} and found that, on average, $\text{VIF}_i < 3$, thus indicating low multicollinearity. One of the reasons why P_{state} has high multicollinearity is because it includes power envelopes of the β frequency band, whose presence in the cerebral cortex is more widespread than γ activity. Additionally, P_{state} comprises twice as many power envelopes as P_{step}. Finally, the power envelopes from P_{state} were computed using a low pass filter, and thus, smoothing the signals and increasing the correlation between them. So, to reduce multicollinearity in P_{state}, we used principal component analysis (PCA). We retained only those principal components that

explained at least 3% of the variance in the data, judged by the eigenvalues of the covariance matrix. We refer to the resulting principal components as $PC_{\text{state}} \in \mathbb{R}^{k \times n}$, where k is the number of retained principal components. We also stored the matrix of principal component coefficients, $pc \in \mathbb{R}^{k \times 2m}$.

Once we had reduced multicollinearity in the data, we performed separate state and step logistic regressions. A logistic regression models the probability of an event occurring, p, as a function of t explanatory variables, $y = [y_1, y_2, ..., y_t] \in \mathbb{R}^{t \times 1}$, and $t + 1$ coefficients, $c = [c_0, c_1, ..., c_t] \in \mathbb{R}^{1 \times (t+1)}$:

$$p = \frac{1}{1 - e^{-(c_0 + \Sigma_{i=1}^{t} c_i y_i)}} \tag{4.2}$$

We trained the coefficients c of our state and step logistic regression using maximum likelihood estimation. For the state logistic regression, we trained the model with $y = PC_{\text{state}}$ and $p = G_{\text{state}}$, and stored the trained coefficients as $c_{\text{state}} \in \mathbb{R}^{1 \times k+1}$. Similarly, to train our step logistic regression, we used $y = P_{\text{step}}$ and $p = G_{\text{step}}$, and stored the resulting coefficients as $c_{\text{step}} \in \mathbb{R}^{1 \times m+1}$. Finally, we defined the extracted feature $f = p_{\text{state}} \cdot p_{\text{step}} \in \mathbb{R}^{1 \times n}$, where $p_{\text{state}} \in \mathbb{R}^{1 \times n}$ is computed using Eq. (4.2) with $y = PC_{\text{state}}$ and $c = c_{\text{state}}$, and similarly, $p_{\text{step}} \in \mathbb{R}^{1 \times n}$ is found using $y = P_{\text{step}}$ and $c = c_{\text{step}}$.

Fokker-Planck Bayesian Filter Training

The last step in the algorithm is a Fokker-Planck-based Bayesian filter to enhance the extracted feature, f, and transform it into a binary signal (step/no step). Specifically, this recursive filter estimates the probability of a step, $p(x)$, based on the extracted feature f, as follows [174]:

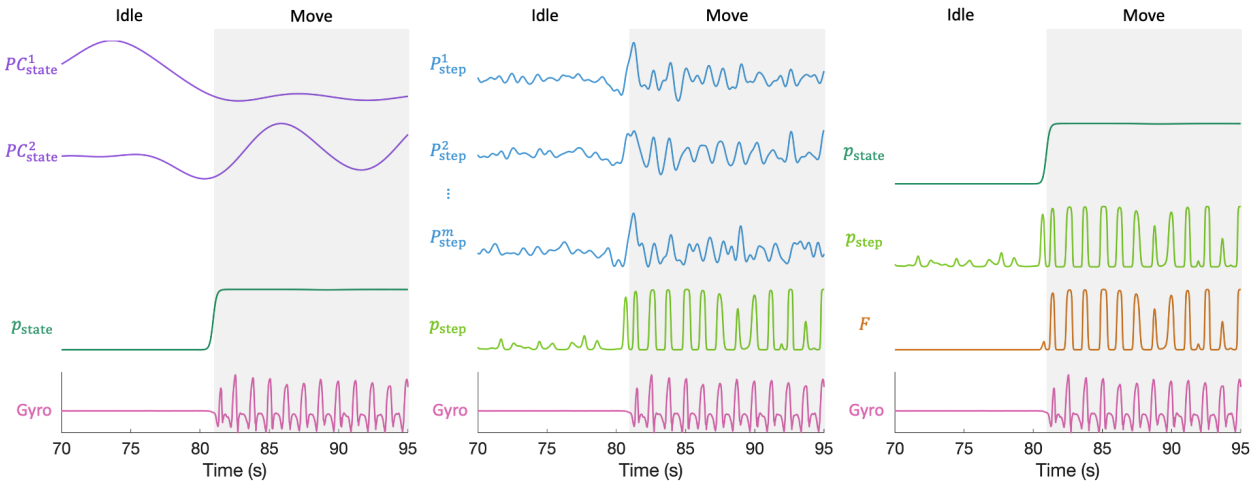


Figure 4.5: Time series of representative extracted signals during an idle/move transition (move segment is shaded in gray). Gyroscope data is used to determine idle (static signal) and move (changes in signal indicate leg swings) periods. (Left) Plot of signals used to decode the state: two principal components, PC_{state} ($k = 2$), and the state logistic regression feature, p_{state}. (Middle) Plot of signals used to decode steps: hγ power envelopes, P_{step}, and the step logistic regression feature, p_{step}. (Right) Plot of the state and step logistic regression features (p_{state} and p_{step}), and their product, the extracted feature f.

$$p(x,t) = \frac{p(f|x)p(x,t_-)}{C} \tag{4.3}$$

where $p(x,t)$ is the probability density of x at time t. This probability depends on the measurement model, $p(f|x)$, and on $p(x,t_-)$, which is the probability density immediately before the measurement f is taken. These variables are described in further detail below. Lastly, C is a constant that ensures $\int_{-\infty}^{\infty} p(x,t)dx = 1$.

To compute $p(x,t_-)$, we propagated in time the prior probability density, $p(x,t-1)$, using a Fokker-Planck equation. First, we assumed that the dynamics of the model (stepping) followed this stochastic differential equation:

$$dx = A(dW) + (U - x)dN_B \tag{4.4}$$

where A is the diffusion coefficient, dW is the differential of standard Brownian motion, and dN_B is the differential of a counting process where B is the rate of jumps per unit time. Also, U is a random variable uniformly distributed on [0,1]. Assuming these dynamics, the Fokker-Planck equation for the time evolution of $p(x,t)$ is:

$$\frac{\partial p(x,t)}{\partial t} = \frac{A^2}{2}\frac{\partial^2 p(x,t)}{\partial x^2} + B[1 - p(x,t)] \tag{4.5}$$

If we enforce $x(t)$ to remain within the interval [0,1], a closed-form solution of this equation does not exist. Thus, we used the finite difference method to compute the numerical solution of Eq. (4.5) and estimate $p(x, t_-)$ as:

$$\begin{aligned} p(x,t_-) = \frac{A^2\Delta t}{2\epsilon^2}p(x-\epsilon,t-1) - \frac{A^2\Delta t}{\epsilon^2}p(x,t-1) \\ + \frac{A^2\Delta t}{2\epsilon^2}p(x+\epsilon,t-1) + B\Delta t + (1 - B\Delta t)p(x,t-1) \end{aligned} \tag{4.6}$$

where x is discretized into bins of width ϵ. To train the parameters A and B we used gyroscope data (*ground truth*). Specifically, we estimated A^2 as the variance in dG_{norm} and B as the average rate of $0 \to 1$ and $1 \to 0$ jumps per second in G_{step}.

On the other hand, to define the measurement model $p(f|x)$ [Eq. (4.3)], we first assumed the reverse conditional probability function, $p(x|f)$, to be a combination of exponential

distributions as follows:

$$p(x|f) = 1 - \mu(f)\lambda e^{-\lambda x} + \mu(f)\lambda e^{\lambda x} e^{-\lambda} \tag{4.7}$$

$$\mu(f) = \frac{1}{1 + e^{-s(f-f_0)}} \tag{4.8}$$

We used the logistic function $\mu(f)$ to get $p(x|f < f_0) = \lambda e^{-\lambda x}$ and $p(x|f > f_0) = \lambda e^{\lambda x} e^{-\lambda}$. We defined the slope of the logistic function $\mu(f)$ as $s = 1/\epsilon$. We estimated λ as the inverse of the expected value of $p(G_{\text{norm}}|F = 0)$ and $p(-G_{\text{norm}} + 1|F = 1)$ (flip left to right). We also estimated f_0 as the minimum value of F for which $p(G_{\text{step}} = 0|F = f_0) < p(G_{\text{step}} = 1|F = f_0)$. Next, we computed $p(f|x)$ using Baye's rule:

$$p(f|x) = \frac{p(x|f)p(f)}{p(x)} \tag{4.9}$$

where we estimated $p(f)$ and $p(x)$ as $p(F)$ and $p(G_{\text{norm}})$, respectively. Finally, we normalized $p(f|x)$ such that $\int_{-\infty}^{\infty} p(f|x)df = 1$.

4.2.4 Decoder Testing

To test the decoder we used a 5-s ECoG segment at a time. First, we preprocessed the ECoG signals as described in Section 4.2.3. Then, we computed the power envelopes P^*_β, P^*_γ and $P^*_{\text{h}\gamma}$

following the methodology described in Section 4.2.3. Then, we computed the state principal components as $PC^*_{\text{state}} = pc \times P^*_{\text{state}}$, where $P^*_{\text{state}} = [P^*_\beta,\ P^*_\gamma]$. Note that pc was obtained during the training process. Next, we implemented the state logistic regression, Eq. (4.2), with $y = PC^*_{\text{state}}$ and $c = c_{\text{state}}$, and stored the output as p^*_{state}. Similarly, we extracted the step feature, p^*_{step}, by performing a logistic regression with $y = P^*_{\text{h}\gamma}$ and $c = c_{\text{step}}$ Then, we computed the extracted feature as $f^* = p^*_{\text{state}} \cdot p^*_{\text{step}}$.

Next, we implemented the Fokker-Planck-based Bayesian filter to clean up and binarize the extracted feature. To implement the recursive algorithm, we used the trained parameters A, B, λ, f_0, ϵ, and s, and followed the steps below:

1. Initialize $p(x, 0)$ as a uniform distribution
2. Forward propagate $p(x, t)$ using Eq. (4.6)
3. Take a measurement, f, from feature F^*
4. Compute the probability distribution $p(x, t)$ using Eqs. (4.3), (4.7), (4.8) and (4.9)
5. Output the decoder estimate as $\text{argmax}(p(x, t))$
6. Repeat from step 2

Finally, after we tested each 5-s segment, we concatenated all the decoded segments and compared it against the ground truth data. Specifically, we compared the steps identified by the algorithm against the G_{step} and quantified the amount of true positives (TP), false positives (FP) and false negatives (FN). For each experiment, we evaluated the performance of the decoder using two metrics: sensitivity, $TP/(TP+FN)$, and precision, $TP/(TP+FP)$.

We envision the real-time implementation of this decoder to operate at 20 Hz. This way, the decoder's latency would be 50 ms, which is within the accepted latency for real-time decoders

($<$ 100 ms). However, the decoder can only be implemented at 20 Hz if a 50 ms signal can be decoded in less than 50 ms. To ensure that this is possible, we counted the number of instructions and clock cycles necessary to implement each decoding operation. We estimated the time necessary to decode 50 ms of data based on the estimated number of necessary and the microprocessor's clock rate. Furthermore, we estimated the power consumption of the decoder based on the microprocessor's technical specifications.

4.3 Results

4.3.1 Subjects

Two subjects, SJ1 (F, 32 y.o.) and SJ2 (F, 38 y.o.), gave their informed consent to participate in the study. They had been implanted with an 8×4 high-density (HD) array of platinum-iridium ECoG electrodes (Integra LifeSciences, Irvine, CA) with a 2-mm diameter and a 4-mm pitch. Note that these HD electrode grids have better spatial resolution and signal quality than standard ECoG grids [207]. Figure 4.6 shows the electrode locations, determined by MRI, for each participant. SJ1 had 26 electrodes in the pre-motor and M1 cortices, while SJ2 had 29 electrodes in the M1 area. Also, the casual speed for SJ1 was 2 mph, and 1 mph for SJ2. SJ1 completed two runs of each task, while SJ2 only completed each task once.

4.3.2 Feature Extraction

To train the feature extraction algorithm, the decoder learned the PCA coefficients, pc, and the state and step logistic regression coefficients, c_{state} and c_{step}, respectively. To do so, we used multi-channel ECoG data, as explained in Section 4.2.3. Figure 4.7 shows the magnitude of these trained coefficients corresponding to electrode, for one of SJ1's walking tasks.

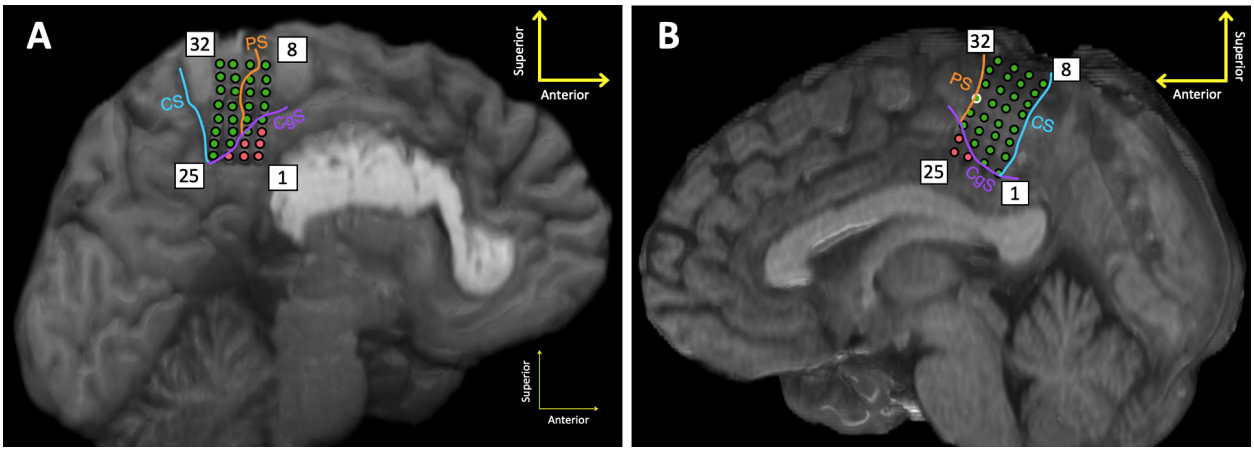


Figure 4.6: Location of the interhemispheric ECoG grid electrodes, determined by MRI, for SJ1 (A) and SJ2 (B). The approximate location of anatomical features are shown as colored lines. CS: Central Sulcus, PS: Precentral Sulcus, and CgS: Cingulate Sulcus. Green electrodes are located in M1 and pre-motor cortex areas, whereas red electrodes are located outside the motor areas. We only decoded data from the green electrodes. For SJ2, data from electrode 29 (outlined in white) was not available during the constant-speed task.

Namely, it shows which electrodes contained the most relevant information for the feature extraction step, with warmer electrode colors indicating a higher contribution (weight) to the extracted feature f. When comparing the contribution of β and γ information for state decoding, we found that, overall, for SJ1 β signals were more relevant than γ signals. Conversely, for SJ2, we found that, in general, γ information contributed equally or more into p_{state} than β information. Figure 4.8 shows a representative segment of an extracted feature, f, in red, compared to the ground truth data, in green.

4.3.3 Fokker-Planck-based Bayesian Filter

To train the filter algorithm and learn the filter's parameters, the decoder used the extracted feature f and gyroscope data. First, we used G_{norm} to train the parameters A and Bwhich describe the dynamics of the model, based on Eq. (4.4). Also, for Eq. (4.6) we used $\Delta t = 50 \cdot 10^{-3}$. Then, we used f, G_{norm}, and G_{state} to train λ and f_0, and defined $\epsilon = 1/33$, to describe the measurement model, $p(f|x)$. Representative examples of trained measurement

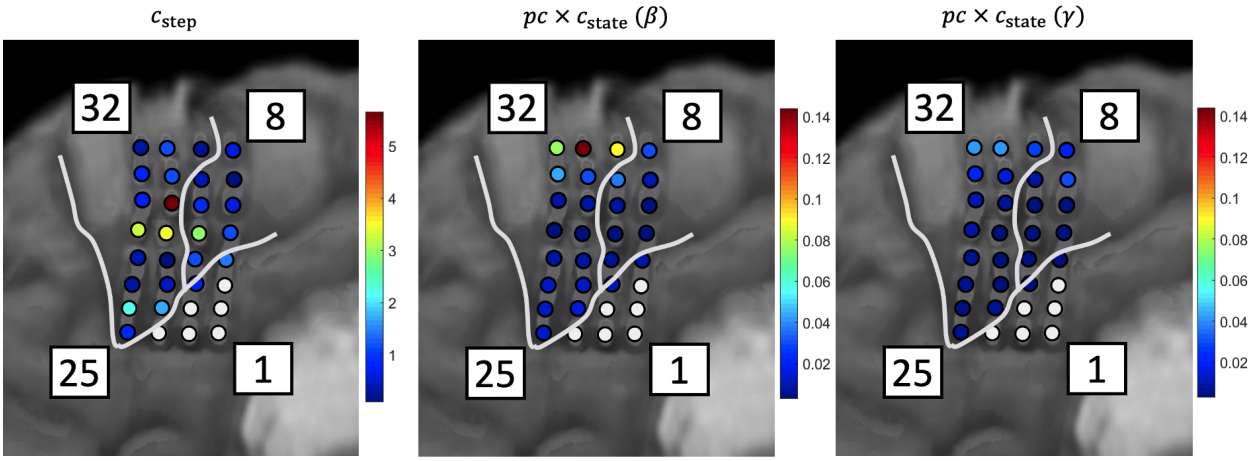


Figure 4.7: Representative feature extraction map (SJ1, variable-speed task, run 1) shown as the magnitude of the trained coefficient matrices: pc, c_{step} and c_{state}. Warmer colors indicate electrodes / frequency bands that were most informative for the principal component analysis and/or logistic regressions. White electrodes were excluded in our study, as they fall outside the cortex of interest.

models for each subject are shown in Fig. 4.9. We observed that in both models, given small (large) values of x, the probability distribution is highly skewed towards lower (higher) values of f. Fig. 4.8 shows a representative segment of the filtered output, for a given extracted feature, f, and compared against the ground truth, G_{step}. As intended, the filter set to 0 small peaks in f that did not correspond to true steps, and set to 1 small and large peaks in f that indeed corresponded to true steps.

4.3.4 Decoder Performance

After we iteratively decoded all adjacent 5-s ECoG data segments for each experiment, we reconstructed the $\sim$ 5.5-min decoded signal and compared it to the ground truth, G_{step}. For each experiment, we quantified the performance of the decoder using sensitivity and precision metrics, and the results are shown in Table 4.1. The sensitivity of the decoder was usually higher than the precision, which indicates that the decoder had more false positives than false negatives. Furthermore, for both subjects, the decoder performed better for the

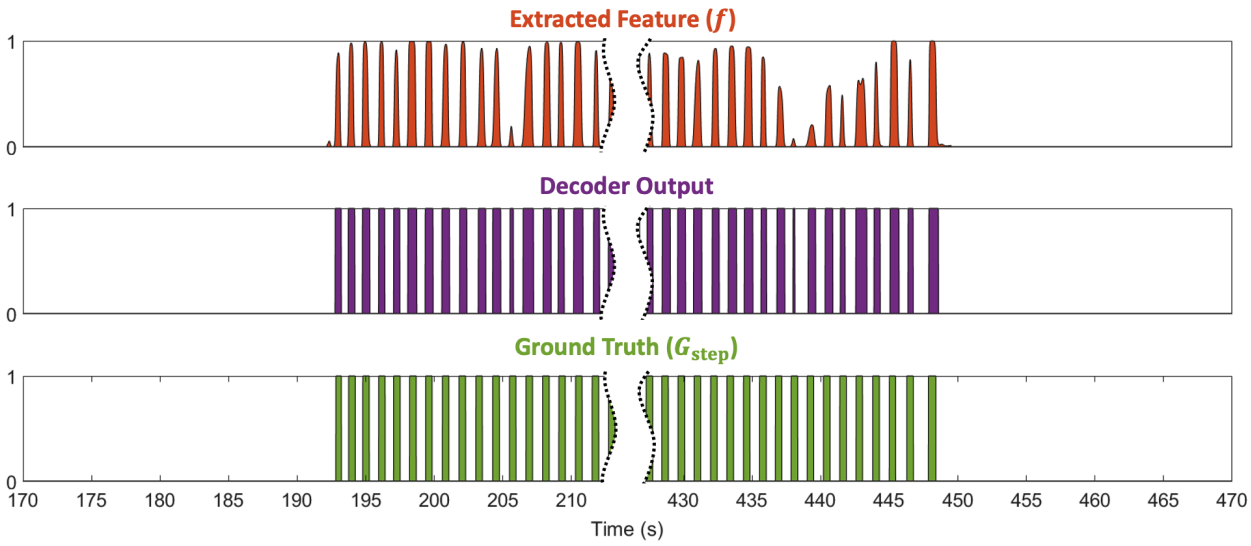


Figure 4.8: Representative segments of an extracted feature f, decoder output, and ground truth, G_{step} signals. The decoder output is obtain by implementing a Fokker-Planck-based filter on the extracted feature f. The decoder's performance is quantified by comparing the decoder output against G_{step}. These signals are part of the constant-speed task (run 2) for SJ1.

constant-speed tasks. Overall, the average sensitivity and precision were 0.99 and 0.94, respectively. Moreover, the decoder's refresh rate (response time) was 20 Hz (50 ms).

To estimate the number of clock cycles necessary to implement each decoding operation for a 50 ms signal, we first had to make some assumptions on the type of ECoG signal that would be decoded. First, we assumed that the signal would be recorded at 1024 Hz. This sampling frequency is enough to capture the highest frequency used in the decoder

Table 4.1: Sensitivity and precision values for every participant's tasks.

Participant	Task	Run	Sensitivity	Precision
1	Constant speed	1	0.99	0.96
1	Constant speed	2	1.00	0.96
1	Variable speed	1	1.00	0.94
1	Variable speed	2	1.00	0.93
2	Constant speed	1	0.99	0.94
2	Variable speed	1	0.98	0.90
		Average	0.99	0.94

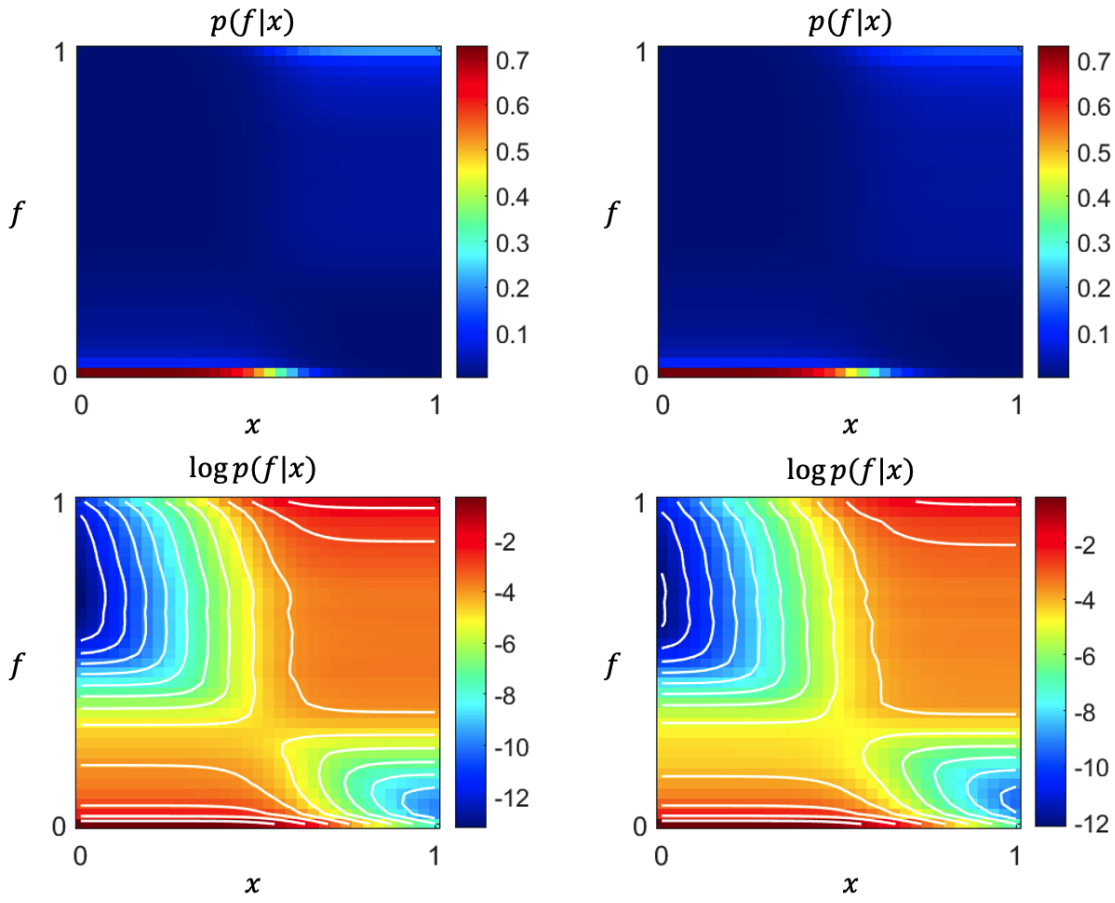


Figure 4.9: Representative measurement model examples for SJ1 (left) and SJ2 (right) for the variable-speed task (Run 1). The trained parameters that described these models were $\lambda = 0.11$, $f_0 = 0.34$ for SJ1, and $\lambda = 0.12$, $f_0 = 0.35$ for SJ2.

(160 Hz). This is a worst-case assumption in terms of computational load, and in reality we envision using a sampling frequency of 512 Hz instead. Additionally, we envisioned an ECoG signal with 32 channels, which would likely cover the entirety of the interhemispheric leg motor cortex. We also assumed that each addition and multiplication operation require 4 clock cycles, whereas each division and exponential operation require 50 and 150 cycles. With all these assumptions, we counted the approximate number of clock cycles required to implement each decoding operation and the results are shown in Table 4.2. The most computationally expensive operation is computing the power envelopes, whereas the least expensive operation is computing the extracted feature, f, from the outputs of the logistic regressions.

Table 4.2: Approximate number of clock cycles necessary to implement each decoding operation in a microprocessor for a 50 ms ECoG signal.

Operation	Clock Cycles
Power Envelope	$2.2{\cdot}10^6$
PCA	$4.7{\cdot}10^4$
State Logistic Regression	$3.4{\cdot}10^3$
Step Logistic Regression	$6.0{\cdot}10^3$
Compute F	$1.5{\cdot}10^2$
Fokker-Planck-based Bayesian filter	$1.7{\cdot}10^3$
Total	$2.2{\cdot}10^6$

We envision implementing the decoder on a microchip such as ATSAMD51J19A-AF [91] or similar, whose core processor is an ARM Cortex-M4 processor. This microprocessor has a clock rate of up to 120 MHz, however, to decode 50 ms signals with our framework a clock rate of 96 MHz is sufficient. Thus, with a clock rate of 96 MHz, we estimate that our system could decode a 50 ms signal in 23 ms. Therefore, there would still be 27 ms left in the decoding window for other necessary instructions such as memory allocation. Given that the necessary time to decode an ECoG signal is less than the decoding window time, this decoder could be implemented in real-time.

The power consumption of an ARM Cortex-M4 processor is 90 μA/MHz [44]. Assuming that the microprocessor operates at 96 MHz and that the supply voltage is 3.3 V, we estimate that the decoder's power consumption will be 28.5 mW. Since the CWU's estimated power budget ranges between 378 and 538 mW (see Chapter 2), we believe that 28.5 mW is an acceptable power consumption level for the decoder.

4.4 Discussion

We designed a recursive algorithm that used ECoG data to decode walking steps. To train this algorithm, we used gyroscope and ECoG data recorded during treadmill walking exper-

iments from two subjects. The decoder achieved high performance metrics, with an average sensitivity of 0.99, and an average precision of 0.94. Moreover, given the algorithm's low complexity, small memory requirements and small latency, we believe this decoder is suitable for real-time implementation in a fully implantable BCI. A Fokker-Planck-based Bayesian decoder for EMG signals, with a similar algorithm architecture to our decoder, was implemented in a 41-MHz ARM7 microcontroller in real-time at 30 Hz [174].

The feature extraction algorithm used concurrent state and step logistic regressions to translate multi-channel ECoG data into a single feature that closely resembles individual walking steps. Note that before the state logistic regression, we used PCA to reduce multicollinearity in the state power envelopes. The extracted feature, f, resembled ground truth data, G_{step}, since its amplitude was usually around 0 during idle periods and >0 when each step occurred. We used the coefficients from the PCA and logistic regressions to visualize which electrodes and frequency bands contained the most relevant information for this feature (Fig, 4.7). With this information, together with the electrode location determined by MRI (Fig. 4.6), we identified which areas of the brain played a role in leg motor planning and execution.

The Fokker-Planck-based Bayesian filter further improved the quality of the extracted feature by binarizing the signal. It set noisy segments to 0, and enhanced true steps by setting them to 1. We trained the filter parameters A and B based on the model's dynamics, i.e., walking kinematics. When the dynamics of the system were consistent during training and testing, such as in the constant-speed task, the decoder predicted steps more accurately. For this reason, the decoder performed better at constant-speed tasks than at variable-speed tasks (Table 4.1). Thus, when implementing this decoder, it is important to include gyroscope data from varied walking kinematics (different speeds and stride lengths) in the training data, similar to those that can be expected during testing.

One of the main sources of error in our decoder were false positives, hence why precision metrics were lower than sensitivity in Table 4.1. Many of these false detections occurred

during the idle/move transition, right before the onset of the first true step. We hypothesize that these detections correspond to motor planning behavior present in the ECoG signals. Given that the treadmill takes some time to start moving, the subject might have anticipated the upcoming step ahead of time. False detections also occurred in between two true steps. We hypothesize that this is due to ECoG data containing features related to ipsilateral leg movements [68]. The false detections usually appeared halfway between two contralateral steps, which is when ipsilateral steps are expected to occur. However, we did not record contralateral kinematic data, and thus cannot corroborate our hypothesis. Future studies should further investigate ipsilateral features in the leg M1 area.

Our decoder and its performance cannot be directly compared to the other existing ECoG-based decoders for lower extremities. For example, Benabid et al. [13] restored walking for a subject with tetraplegia. In this case, the decoder's sensitivity was 0.72, but their implementation was very different from ours. On one hand, they tested the decoder's performance online, whereas we tested ours offline. On the other hand, their system decoded walking states, whereas ours decoded individual steps. Similarly, Lorach et al. [128] restored movement of the lower limbs and walking in a subject with paraplegia. They reported that the subject was able to control each joint bilaterally in real-time with accuracy of 0.74. However, they did not quantify the decoder's performance for walking steps, since they did not use cues during walking.

While developing our decoder, we identified some actions that could potentially improve the decoder's performance. For example, we found that ERS and ERD occurred at different frequency bands for each subject. In the future, instead of using fixed frequency bands, we could use training data to determine accurate bounds of β (ERD) and γ (ERD) for each subject. Additionally, we could try using a different measurement model equation. The solution we presented here is one alternative, but it could be that other shapes are more appropriate to describe the relationship between the gyroscope data and the extracted

feature. An important limitation of our study is the limited data available. Although there is abundant ECoG data of able-body individuals performing motor task of their upper extremities, similar data for the lower extremities is scarce. Recording ECoG data of able-body individuals while walking on a treadmill requires complex experimental setup. To our knowledge, we are the first group to perform these experiments. In the future, we would like to collect more data and verify that our finding apply to other individuals. We should also collect over ground walking data, since the walking kinematics will likely be different than those of treadmill walking.

Our end goal is to implement this decoder in real-time in our fully-implantable BD-BCI prototype [205, 192]. Based on our estimations (see Table 4.2), we believe that this decoder can be implemented in real-time and provide decoded updates every 50 ms (20 Hz). Moreover, we estimate that the decoder will not consume more than 28.5 mW. This is an acceptable power consumption level for the decoder because based on the estimated CWU power budget (Chapter 2), this would leave between 349 and 509 mW for the other CWU operations (wireless data transmission and stimulation signal generation).

4.5 Conclusion

We developed a decoder to identify individual walking steps from ECoG signals. The decoder used a feature extraction module based on logistic regressions followed by a Fokker-Planck-based Bayesian filter. We tested the decoder's performance offline using ECoG data from two subjects while they walked on a treadmill. Using a leave-one-out cross-validation approach, we found that the decoder's average sensitivity and precision were 99% and 94%, respectively. We also showed that thanks to the decoder's low computational complexity, the decoder is suitable for real-time implementation. Finally, we estimated that deploying this decoder in a microprocessor in real time would require up to 28.5 mW of power. Based on our CWU

power budget estimations, we believe that this is an acceptable power consumption level for our BD-BCI decoder. To our knowledge, this is the first decoder that can estimate individual steps from ECoG signals from the leg motor cortex that is suitable for real-time implementation in a fully-implantable BCI.

Bibliography

[1] T. Allison, G. McCarthy, M. Luby, A. Puce, and D. D. Spencer. Localization of functional regions of human mesial cortex by somatosensory evoked potential recording and by cortical stimulation. *Electroencephalography and Clinical Neurophysiology/Evoked Potentials Section*, 100(2):126–140, mar 1996.

[2] A. Andreozzi, L. Brunese, M. Iasiello, C. Tucci, and G. Peter Vanoli. Bioheat transfer in a spherical biological tissue: a comparison among various models. *Journal of Physics: Conference Series*, 1224(1):012001, may 2019.

[3] K. K. Ang, K. S. G. Chua, K. S. Phua, C. Wang, Z. Y. Chin, C. W. K. Kuah, W. Low, and C. Guan. A Randomized Controlled Trial of EEG-Based Motor Imagery Brain-Computer Interface Robotic Rehabilitation for Stroke. *Clinical EEG and Neuroscience*, 46(4):310–320, oct 2015.

[4] P. Argiento, N. Chesler, M. Mule, M. D'Alto, E. Bossone, P. Unger, and R. Naeije. Exercise stress echocardiography for the study of the pulmonary circulation. *European Respiratory Journal*, 35(6):1273–1278, jun 2010.

[5] M. Armenta Salas, L. Bashford, S. Kellis, M. Jafari, H. Jo, D. Kramer, K. Shanfield, K. Pejsa, B. Lee, C. Y. Liu, and R. A. Andersen. Proprioceptive and cutaneous sensations in humans elicited by intracortical microstimulation. *eLife*, 7:e32904, apr 2018.

[6] P. Arzuaga. Cardiac pacemakers: Past, present and future. *IEEE Instrumentation and Measurement Magazine*, 17(3):21–27, 2014.

[7] E. Asano, C. Juhasz, A. Shah, O. Muzik, D. C. Chugani, J. Shah, S. Sood, and H. T. Chugani. Origin and Propagation of Epileptic Spasms Delineated on Electrocorticography. *Epilepsia*, 46(7):1086–1097, jul 2005.

[8] F. Babiloni, F. Cincotti, F. Carducci, P. M. Rossini, and C. Babiloni. Spatial enhancement of EEG data by surface Laplacian estimation: the use of magnetic resonance imaging-based head models. *Clinical Neurophysiology*, 112(5):724–727, may 2001.

[9] M. W. Baker. *A low-power cochlear implant system.* PhD thesis, Massachusetts Institute of Technology, Cambridge, MA, USA, 2007.

[10] T. Ball, M. Kern, I. Mutschler, A. Aertsen, and A. Schulze-Bonhage. Signal quality of simultaneously recorded invasive and non-invasive EEG. *NeuroImage*, 46(3):708–716, jul 2009.

[11] K. E. Barrett, S. M. Barman, J. Yuan, and H. L. Brooks. *Ganong's review of medical physiology*. McGraw-Hill Education/Medical, 26 edition, jan 2019.

[12] S. G. Beirão, A. P. Ribeiro, M. J. Lourenço, F. J. Santos, and C. A. Nieto De Castro. Thermal conductivity of humid air. *International Journal of Thermophysics*, 33(8-9):1686–1703, 2012.

[13] A. L. Benabid, T. Costecalde, A. Eliseyev, G. Charvet, A. Verney, S. Karakas, M. Foerster, A. Lambert, B. Morinière, N. Abroug, M. C. Schaeffer, A. Moly, F. Sauter-Starace, D. Ratel, C. Moro, N. Torres-Martinez, L. Langar, M. Oddoux, M. Polosan, S. Pezzani, V. Auboiroux, T. Aksenova, C. Mestais, and S. Chabardes. An exoskeleton controlled by an epidural wireless brain–machine interface in a tetraplegic patient: a proof-of-concept demonstration. *The Lancet Neurology*, 18(12):1112–1122, dec 2019.

[14] J. Bennett, J. M Das, and P. D. Emmady. *Spinal Cord Injuries*. StatPearls Publishing, Treasure Island (FL), 2022.

[15] L. Berdondini, T. Overstolz, N. F. de Rooij, M. Koudelka-Hep, M. Wany, and P. Seitz. High-density microelectrode arrays for electrophysiological activity imaging of neuronal networks. In *ICECS 2001. 8th IEEE International Conference on Electronics, Circuits and Systems (Cat. No.01EX483)*, pages 1239–1242. IEEE, 2001.

[16] C. H. Best, N. B. Taylor, and J. R. Brobeck. *Best & Taylor's physiological basis of medical practice*. Williams & Wilkins, 1979.

[17] A. Bettaieb, P. K. Wrzal, and D. A. Averill-Bates. Hyperthermia: Cancer treatment and beyond. *Cancer treatment-conventional and innovative approaches*, pages 257–283, 2013.

[18] R. Biran, D. C. Martin, and P. A. Tresco. Neuronal cell loss accompanies the brain tissue response to chronically implanted silicon microelectrode arrays. *Experimental Neurology*, 195(1):115–126, sep 2005.

[19] N. Birbaumer. Breaking the silence: Brain-computer interfaces (BCI) for communication and motor control. *Psychophysiology*, 43(6):517–532, nov 2006.

[20] B. Blankertz, G. Curio, and K. R. Müller. Classifying single trial eeg: Towards brain computer interfacing. In *Proceedings of the 14th International Conference on Neural Information Processing Systems: Natural and Synthetic*, NIPS'01, page 157–164, Cambridge, MA, USA, 2001. MIT Press.

[21] F. Boi, T. Moraitis, V. De Feo, F. Diotalevi, C. Bartolozzi, G. Indiveri, and A. Vato. A Bidirectional Brain-Machine Interface Featuring a Neuromorphic Hardware Decoder. *Frontiers in Neuroscience*, 10, dec 2016.

[22] A. T. Boye, U. Q. Kristiansen, M. Billinger, O. F. do Nascimento, and D. Farina. Identification of movement-related cortical potentials with optimized spatial filtering and principal component analysis. *Biomedical Signal Processing and Control*, 3(4):300–304, 2008.

[23] R. Boyer, G. Welsch, and E. W. Collings. *Materials Properties Handbook - Titanium Alloys*. ASM International, 1994.

[24] J. S. Brumberg, A. Nieto-Castanon, P. R. Kennedy, and F. H. Guenther. Brain–computer interfaces for speech communication. *Speech Communication*, 52(4):367–379, 2010.

[25] A. F. Bueno, F. A. Lemos, M. E. Ferrareze, W. A. M. dos Santos, F. V. Veronese, and A. S. Dias. Muscle thickness of the pectoralis major and rectus abdominis and level of physical activity in chronic hemodialysis patients. *Jornal Brasileiro de Nefrologia*, 39(4), 2017.

[26] D. T. Bundy, M. Pahwa, N. Szrama, and E. C. Leuthardt. Decoding three-dimensional reaching movements using electrocorticographic signals in humans. *Journal of Neural Engineering*, 13(2):026021, apr 2016.

[27] D. J. Caldwell, J. A. Cronin, J. Wu, K. E. Weaver, A. L. Ko, R. P. N. Rao, and J. G. Ojemann. Direct stimulation of somatosensory cortex results in slower reaction times compared to peripheral touch in humans. *Scientific Reports*, 9(1):3292, mar 2019.

[28] W. D. Callister. *Materials Science and Engineering: An Introduction*. John Wiley and Sons (WIE), 5 edition, 1999.

[29] T. Campi, S. Cruciani, V. De Santis, and M. Feliziani. EMF Safety and Thermal Aspects in a Pacemaker Equipped With a Wireless Power Transfer System Working at Low Frequency. *IEEE Transactions on Microwave Theory and Techniques*, pages 1–8, 2016.

[30] H. Cecotti. A Self-Paced and Calibration-Less SSVEP-Based Brain–Computer Interface Speller. *IEEE Transactions on Neural Systems and Rehabilitation Engineering*, 18(2):127–133, apr 2010.

[31] C. V. Chaparro, L. V. Herrera, A. M. Meléndez, and D. A. Miranda. Considerations on electrical impedance measurements of electrolyte solutions in a four-electrode cell. *Journal of Physics: Conference Series*, 687:012101, feb 2016.

[32] C. A. Chestek, V. Gilja, C. H. Blabe, B. L. Foster, K. V. Shenoy, J. Parvizi, and J. M. Henderson. Hand posture classification using electrocorticography signals in the gamma band over human sensorimotor brain areas. *Journal of Neural Engineering*, 10(2):026002, apr 2013.

[33] H. Choi, J. Lee, J. Park, B. H. Cho, K. M. Lee, and D. P. Jang. Movement state classification for bimanual bci from non-human primate's epidural ecog using three-dimensional convolutional neural network. In *2018 6th International Conference on Brain-Computer Interface (BCI)*, pages 1–3, 2018.

[34] A. L. Cowles, H. H. Borgstedt, and A. J. Gillies. Tissue Weights and Rates of Blood Flow in Man for the Prediction of Anesthetic Uptake and Distribution. *Anesthesiology*, 35(5):523–526, nov 1971.

[35] N. E. Crone, D. L. Miglioretti, B. Gordon, and R. P. Lesser. Functional mapping of human sensorimotor cortex with electrocorticographic spectral analysis. ii. event-related synchronization in the gamma band. *Brain: a journal of neurology*, 121(12):2301–2315, 1998.

[36] N. E. Crone, D. L. Miglioretti, B. Gordon, J. M. Sieracki, M. T. Wilson, S. Uematsu, and R. P. Lesser. Functional mapping of human sensorimotor cortex with electrocorticographic spectral analysis. i. alpha and beta event-related desynchronization. *Brain: a journal of neurology*, 121(12):2271–2299, 1998.

[37] J. A. Cronin, J. Wu, K. L. Collins, D. Sarma, R. P. N. Rao, J. G. Ojemann, and J. D. Olson. Task-Specific Somatosensory Feedback via Cortical Stimulation in Humans. *IEEE Transactions on Haptics*, 9(4):515–522, oct 2016.

[38] R. Cubo, M. Fahlström, E. Jiltsova, H. Andersson, and A. Medvedev. Calculating deep brain stimulation amplitudes and power consumption by constrained optimization. *Journal of Neural Engineering*, 16(1):016020, feb 2019.

[39] C. R. Davies, F. Fukumura, K. Fukamachi, K. Muramoto, S. C. Himley, A. Massiello, J.-F. Chen, and H. Harasaki. Adaptation of Tissue to a Chronic Heat Load. *ASAIO Journal*, 40(3):M514–M517, jul 1994.

[40] N. Deep, E. Dowling, D. Jethanamest, and M. Carlson. Cochlear Implantation: An Overview. *Journal of Neurological Surgery Part B: Skull Base*, 80(02):169–177, apr 2019.

[41] V. E. Del Bene. Temperature. In *Clinical Methods: The History, Physical, and Laboratory Examinations*. Butterworths, 1990.

[42] J. del R. Millan, J. Mourino, F. Babiloni, F. Cincotti, M. Varsta, and J. Heikkonen. Local neural classifier for eeg-based recognition of mental tasks. In *Proceedings of the IEEE-INNS-ENNS International Joint Conference on Neural Networks. IJCNN 2000. Neural Computing: New Challenges and Perspectives for the New Millennium*, volume 3, pages 632–636 vol.3, 2000.

[43] P. D. Desai. Thermodynamic properties of titanium. *International Journal of Thermophysics*, 8(6):781–794, 1987.

[44] E. Design. High efficiency cortex-m4 mcus consume less power. https://www.electronicdesign.com/technologies/embedded/digital-ics/processors/microcontrollers/article/21752724/high-efficiency-cortexm4-mcus-consume-less-power. Accessed: 2023-08-10.

[45] M. W. Dewhirst, B. L. Viglianti, M. Lora-Michiels, M. Hanson, and P. J. Hoopes. Basic principles of thermal dosimetry and thermal thresholds for tissue damage from hyperthermia. *International Journal of Hyperthermia*, 19(3):267–294, 2003.

[46] J. P. DiMarco. Implantable Cardioverter–Defibrillators. *New England Journal of Medicine*, 349(19):1836–1847, nov 2003.

[47] A. H. Do, P. T. Wang, C. E. King, A. Abiri, and Z. Nenadic. Brain-Computer Interface Controlled Functional Electrical Stimulation System for Ankle Movement. *Journal of NeuroEngineering and Rehabilitation*, 8(1):49, 2011.

[48] A. H. Do, P. T. Wang, C. E. King, S. N. Chun, and Z. Nenadic. Brain-computer interface controlled robotic gait orthosis. *Journal of NeuroEngineering and Rehabilitation*, 10(1):111, 2013.

[49] D. J. Downing, R. H. Gardner, and F. O. Hoffman. An Examination of Response-Surface Methodologies for Uncertainty Analysis in Assessment Models. *Technometrics*, 27(2):151–163, may 1985.

[50] A. Dubey and S. Ray. Comparison of tuning properties of gamma and high-gamma power in local field potential (LFP) versus electrocorticogram (ECoG) in visual cortex. *Scientific Reports*, 10(1):5422, 2020.

[51] F. A. Duck. Thermal Properties of Tissue. In *Physical Properties of Tissues*, pages 9–42. Elsevier, 1990.

[52] A. M. Ebied, G. J. Kemp, and S. P. Frostick. The role of cutaneous sensation in the motor function of the hand. *Journal of Orthopaedic Research*, 22(4):862–866, jul 2004.

[53] M. M. Elwassif, A. Datta, A. Rahman, and M. Bikson. Temperature control at DBS electrodes using a heat sink: experimentally validated FEM model of DBS lead architecture. *Journal of Neural Engineering*, 9(4):46009, jul 2012.

[54] M. M. Elwassif, Q. Kong, M. Vazquez, and M. Bikson. Bio-heat transfer model of deep brain stimulation-induced temperature changes. *Journal of Neural Engineering*, 3(4), 2006.

[55] A. Ermis, Y.-P. Lai, X. Pan, R. Chai, and Y. Zhang. Recursive subspace identification for online thermal management of implantable devices. In *2019 57th Annual Allerton Conference on Communication, Control, and Computing (Allerton)*, pages 944–949, 2019.

[56] N. Even-Chen, D. G. Muratore, S. D. Stavisky, L. R. Hochberg, J. M. Henderson, B. Murmann, and K. V. Shenoy. Power-saving design opportunities for wireless intracortical brain–computer interfaces. *Nature Biomedical Engineering*, 4(10):984–996, 2020.

[57] F. M. Faraci, K. A. Kadel, and D. D. Heistad. Vascular responses of dura mater. *American Journal of Physiology-Heart and Circulatory Physiology*, 257(1):H157–H161, jul 1989.

[58] L. A. Farwell and E. Donchin. Talking off the top of your head: toward a mental prosthesis utilizing event-related brain potentials. *Electroencephalography and Clinical Neurophysiology*, 70(6):510–523, dec 1988.

[59] R. Fazel-Rezai, B. Z. Allison, C. Guger, E. W. Sellers, S. C. Kleih, and A. Kübler. P300 brain computer interface: current challenges and emerging trends. *Frontiers in Neuroengineering*, 5, 2012.

[60] A. Feldmann, P. Wili, G. Maquer, and P. Zysset. The thermal conductivity of cortical and cancellous bone. *European Cells and Materials*, 35:25–33, jan 2018.

[61] E. Fernandez, B. Greger, P. A. House, I. Aranda, C. Botella, J. Albisua, C. Soto-Sanchez, A. Alfaro, and R. A. Normann. Acute human brain responses to intracortical microelectrode arrays: challenges and future prospects. *Frontiers in Neuroengineering*, 7, jul 2014.

[62] M. S. Fifer, D. P. McMullen, T. M. Thomas, L. E. Osborn, R. W. Nickl, D. N. Candrea, E. A. Pohlmeyer, M. C. Thompson, M. Anaya, W. Schellekens, N. F. Ramsey, S. J. Bensmaia, W. S. Anderson, B. A. Wester, N. E. Crone, P. A. Celnik, G. L. Cantarero, and F. V. Tenore. Intracortical Microstimulation Elicits Human Fingertip Sensations. *medRxiv*, 2020.

[63] B. Fisch. *Fisch and Spehlmann's EEG primer: Basic Principles of Digital and Analog EEG*. Elsevier Health Sciences, London, England, 3 edition, Dec. 1999.

[64] S. Flesher, J. Downey, J. Collinger, S. Foldes, J. Weiss, E. Tyler-Kabara, S. Bensmaia, A. Schwartz, M. Boninger, and R. Gaunt. Intracortical Microstimulation as a Feedback Source for Brain-Computer Interface Users. In C. Guger, B. Allison, and M. Lebedev, editors, *Brain-Computer Interface Research: A State-of-the-Art Summary 6*, pages 43–54. Springer International Publishing, Cham, 2017.

[65] Food and Drug Administration. Electrocardiograph electrodes - class ii special controls guidance for industry and food and drug administration staff. `https://www.fda.gov/medical-devices/guidance-documents-medical-devices-and-radiation-emitting-products/electrocardiograph-electrodes-class-ii-special-controls-guidance-industry-and-food-and-drug#3`, 2007. Accessed: 2023-06-12.

[66] A. F. Frydrychowski, A. Szarmach, B. Czaplewski, and P. J. Winklewski. Subarachnoid Space: New Tricks by an Old Dog. *PLoS ONE*, 7(5):e37529, may 2012.

[67] S. Fujii, H. Sasaki, K. Ito, K. Kaneko, and H. Kato. Temperature Dependence of Synaptic Responses in Guinea Pig Hippocampal CA1 Neurons in Vitro. *Cellular and Molecular Neurobiology*, 22(4):379–391, 2002.

[68] K. Ganguly, L. Secundo, G. Ranade, A. Orsborn, E. F. Chang, D. F. Dimitrov, J. D. Wallis, N. M. Barbaro, R. T. Knight, and J. M. Carmena. Cortical Representation of Ipsilateral Arm Movements in Monkey and Man. *The Journal of Neuroscience*, 29(41):12948–12956, oct 2009.

[69] M. S. George, H. A. Sackeim, A. J. Rush, L. B. Marangell, Z. Nahas, M. M. Husain, S. Lisanby, T. Burt, J. Goldman, and J. C. Ballenger. Vagus nerve stimulation: a new tool for brain research and therapy. *Biological Psychiatry*, 47(4):287–295, feb 2000.

[70] G. H. Glover. Overview of Functional Magnetic Resonance Imaging. *Neurosurgery Clinics of North America*, 22(2):133–139, apr 2011.

[71] L. S. Goldstein, M. W. Dewhirst, M. Repacholi, and L. Kheifets. Summary, conclusions and recommendations: adverse temperature levels in the human body. *International Journal of Hyperthermia*, 19(3):373–384, jan 2003.

[72] R. G. Gordon, R. B. Roemer, and S. M. Horvath. A Mathematical Model of the Human Temperature Regulatory System–Transient Cold Exposure Response. *IEEE Transactions on Biomedical Engineering*, BME-23(6):434–444, 1976.

[73] S. S. Grewal, R. S. Zimmerman, G. Worrell, B. H. Brinkmann, W. O. Tatum, A. Z. Crepeau, D. A. Woodrum, K. R. Gorny, J. P. Felmlee, R. E. Watson, J. M. Hoxworth, V. Gupta, P. Vibhute, M. R. Trenerry, T. J. Kaufmann, W. R. Marsh, R. E. Wharen, and J. J. V. Gompel. Laser ablation for mesial temporal epilepsy: a multi-site, single institutional series. *Journal of Neurosurgery JNS*, 130(6):2055–2062, 2019.

[74] G. Grimby, E. Häggendal, and B. Saltin. Local xenon 133 clearance from the quadriceps muscle during exercise in man. *Journal of Applied Physiology*, 22(2):305–310, feb 1967.

[75] S. P. Gurrum, D. R. Edwards, T. Marchand-Golder, J. Akiyama, S. Yokoya, J. F. Drouard, and F. Dahan. Generic thermal analysis for phone and tablet systems. In *2012 IEEE 62nd Electronic Components and Technology Conference*, pages 1488–1492. IEEE, may 2012.

[76] A. C. Guyton. *Human physiology and mechanisms of disease*. W B Saunders, London, England, 6 edition, dec 1996.

[77] K. W. Ha and J. W. Jeong. Decoding two-class motor imagery eeg with capsule networks. In *2019 IEEE International Conference on Big Data and Smart Computing (BigComp)*, pages 1–4. IEEE, 2019.

[78] M. Haghjoo. Techniques of Permanent Pacemaker Implantation, Current Issues and Recent Advances in Pacemaker Therapy. *Cardiovascular Medicine*, pages 4–10, 2012.

[79] B. A. Hargreaves, P. W. Worters, K. B. Pauly, J. M. Pauly, K. M. Koch, and G. E. Gold. Metal-Induced Artifacts in MRI. *American Journal of Roentgenology*, 197(3):547–555, sep 2011.

[80] P. A. Hasgall, F. Di Gennaro, C. Baumgartner, E. Neufeld, B. Lloyd, M. C. Gosselin, D. Payne, A. Klingenböck., and N. Kuster. IT'IS Database for thermal and electromagnetic parameters of biological tissues. urlhttps://itis.swiss/virtual-population/tissue-properties/downloads/database-v4-0/, 2018.

[81] I. Heinonen, R. Boushel, Y. Hellsten, and K. Kalliokoski. Regulation of bone blood flow in humans: The role of nitric oxide, prostaglandins, and adenosine. *Scandinavian Journal of Medicine & Science in Sports*, 28(5):1552–1558, may 2018.

[82] I. Heinonen, M. Bucci, J. Kemppainen, J. Knuuti, P. Nuutila, R. Boushel, and K. K. Kalliokoski. Regulation of subcutaneous adipose tissue blood flow during exercise in humans. *Journal of Applied Physiology*, 112(6):1059–1063, mar 2012.

[83] K. A. Higazi and J. A. Chalmers. Measurements of atmospheric electrical conductivity near the ground. *Journal of Atmospheric and Terrestrial Physics*, 28(3):327–330, 1966.

[84] S. V. Hiremath, E. C. Tyler-Kabara, J. J. Wheeler, D. W. Moran, R. A. Gaunt, J. L. Collinger, S. T. Foldes, D. J. Weber, W. Chen, M. L. Boninger, and W. Wang. Human perception of electrical stimulation on the surface of somatosensory cortex. *PLOS ONE*, 12(5):e0176020, may 2017.

[85] L. R. Hochberg, D. Bacher, B. Jarosiewicz, N. Y. Masse, J. D. Simeral, J. Vogel, S. Haddadin, J. Liu, S. S. Cash, P. van der Smagt, and J. P. Donoghue. Reach and grasp by people with tetraplegia using a neurally controlled robotic arm. *Nature*, 485(7398):372–375, may 2012.

[86] U. Hoffmann, G. Garcia, J.-M. Vesin, K. Diserens, and T. Ebrahimi. A boosting approach to p300 detection with application to brain-computer interfaces. In *Conference Proceedings. 2nd International IEEE EMBS Conference on Neural Engineering, 2005.*, pages 97–100, 2005.

[87] H. Hori, G. Moretti, A. Rebora, and F. Crovato. The thickness of human scalp: normal and bald. *The Journal of investigative dermatology*, 58(6):396–399, 1972.

[88] G. Hotson, D. P. McMullen, M. S. Fifer, M. S. Johannes, K. D. Katyal, M. P. Para, R. Armiger, W. S. Anderson, N. V. Thakor, B. A. Wester, and N. E. Crone. Individual finger control of a modular prosthetic limb using high-density electrocorticography in a human subject. *Journal of Neural Engineering*, 13(2):026017, apr 2016.

[89] C. Hughes, A. Herrera, R. Gaunt, and J. Collinger. Chapter 13 - Bidirectional brain-computer interfaces. In N. F. Ramsey and J. del R. Millán, editors, *Brain-Computer Interfaces*, volume 168 of *Handbook of Clinical Neurology*, pages 163–181. Elsevier, 2020.

[90] T. S. Ibrahim, D. Abraham, and R. L. Rennaker. Electromagnetic Power Absorption and Temperature Changes due to Brain Machine Interface Operation. *Annals of Biomedical Engineering*, 35(5):825–834, may 2007.

[91] M. T. Inc. Sam d5x/e5x family data sheet. `https://ww1.microchip.com/downloads/en/DeviceDoc/SAM_D5x_E5x_Family_Data_Sheet_DS60001507G.pdf`. Accessed: 2023-08-10.

[92] Intan Technologies. RHD2000 Series Digital Electrophysiology Interface Chips. `https://intantech.com/files/Intan_RHD2000_series_datasheet.pdf`, 2012. Accessed: 2023-06-26.

[93] B. H. Jansen, J. R. Bourne, and J. W. Ward. Autoregressive estimation of short segment spectra for computerized eeg analysis. *IEEE Transactions on Biomedical Engineering*, BME-28(9):630–638, 1981.

[94] T. Jiang, T. Jiang, T. Wang, S. Mei, Q. Liu, Y. Li, X. Wang, S. Prabhu, Z. Sha, and N. F. Ince. Characterization and decoding the spatial patterns of hand extension/flexion using high-density ecog. *IEEE Transactions on Neural Systems and Rehabilitation Engineering*, 25(4):370–379, 2017.

[95] R. S. Johansson, C. Häger, and L. Bäckström. Somatosensory control of precision grip during unpredictable pulling loads. *Experimental Brain Research*, 89(1):204–213, apr 1992.

[96] L. A. Johnson, J. D. Wander, D. Sarma, D. K. Su, E. E. Fetz, and J. G. Ojemann. Direct electrical stimulation of the somatosensory cortex in humans using electrocorticography electrodes: a qualitative and quantitative report. *Journal of Neural Engineering*, 10(3):036021, jun 2013.

[97] L. G. Jorgensen, M. Perko, B. Hanel, T. V. Schroeder, and N. H. Secher. Middle cerebral artery flow velocity and blood flow during exercise and muscle ischemia in humans. *Journal of Applied Physiology*, 72(3):1123–1132, mar 1992.

[98] A. Kachenoura, L. Albera, L. Senhadji, and P. Comon. Ica: a potential tool for bci systems. *IEEE Signal Processing Magazine*, 25(1):57–68, 2008.

[99] A. Karimi-Bidhendi, O. Malekzadeh-Arasteh, M. C. Lee, C. M. McCrimmon, P. T. Wang, A. Mahajan, C. Y. Liu, Z. Nenadic, A. H. Do, and P. Heydari. CMOS Ultralow Power Brain Signal Acquisition Front-Ends: Design and Human Testing. *IEEE Transactions on Biomedical Circuits and Systems*, 11(5):1111–1122, 2017.

[100] S. Kellis, S. Hanrahan, T. Davis, P. A. House, R. Brown, and B. Greger. Decoding hand trajectories from micro-electrocorticography in human patients. In *2012 Annual International Conference of the IEEE Engineering in Medicine and Biology Society*, pages 4091–4094. IEEE, aug 2012.

[101] B. Kerous, F. Skola, and F. Liarokapis. EEG-based BCI and video games: a progress report. *Virtual Reality*, 22(2):119–135, jun 2018.

[102] J. Kim and Y. Rahmat-Samii. Implanted Antennas Inside a Human Body: Simulations, Designs, and Characterizations. *IEEE Transactions on Microwave Theory and Techniques*, 52(8):1934–1943, aug 2004.

[103] S. Kim, P. Tathireddy, R. A. Normann, and F. Solzbacher. Thermal Impact of an Active 3-D Microelectrode Array Implanted in the Brain. *IEEE T. Neur. Sys. Reh.*, 15(4):493–501, dec 2007.

[104] D. R. Kipke, R. J. Vetter, J. C. Williams, and J. F. Hetke. Silicon-substrate intracortical microelectrode arrays for long-term recording of neuronal spike activity in cerebral cortex. *IEEE Transactions on Neural Systems and Rehabilitation Engineering*, 11(2):151–155, 2003.

[105] S. C. Kirin, T. Yanagisawa, S. Oshino, K. Edakawa, M. Tanaka, H. Kishima, and Y. Nishimura. Somatosensation Evoked by Cortical Surface Stimulation of the Human Primary Somatosensory Cortex. *Frontiers in Neuroscience*, 13, sep 2019.

[106] E. A. Kiyatkin. Brain temperature homeostasis: physiological fluctuations and pathological shifts. *Frontiers in Bioscience*, 15(1):73, 2010.

[107] S. M. Kong, M. Mariatti, and J. J. C. Busfield. Effects of types of fillers and filler loading on the properties of silicone rubber composites. *Journal of Reinforced Plastics and Composites*, 30(13):1087–1096, jul 2011.

[108] P. Kosky, R. Balmer, W. Keat, and G. Wise. Mechanical Engineering. In *Exploring Engineering*, chapter 5, pages 317–340. Elsevier, 2021.

[109] G. Kovacs, A. Berghold, S. Scheidl, and H. Olschewski. Pulmonary arterial pressure during rest and exercise in healthy subjects: a systematic review. *European Respiratory Journal*, 34(4):888–894, oct 2009.

[110] D. J. Krusienski, E. W. Sellers, D. J. McFarland, T. M. Vaughan, and J. R. Wolpaw. Toward enhanced P300 speller performance. *Journal of Neuroscience Methods*, 167(1):15–21, jan 2008.

[111] J. Kubánek, K. J. Miller, J. G. Ojemann, J. R. Wolpaw, and G. Schalk. Decoding flexion of individual fingers using electrocorticographic signals in humans. *Journal of Neural Engineering*, 6(6):066001, dec 2009.

[112] H. Kuchiwaki, S. Inao, N. Ishii, Y. Ogura, and S. P. Gu. Human dural thickness measured by ultrasonographic method: reflection of intracranial pressure. *Journal of Ultrasound in Medicine*, 16(11):725–730, nov 1997.

[113] J. LaRocco and D.-G. Paeng. Optimizing Computer–Brain Interface Parameters for Non-invasive Brain-to-Brain Interface. *Frontiers in Neuroinformatics*, 14, feb 2020.

[114] A. Laurent, F. Mistretta, D. Bottigioli, K. Dahel, C. Goujon, J. F. Nicolas, A. Hennino, and P. E. Laurent. Echographic measurement of skin thickness in adults by high frequency ultrasound to assess the appropriate microneedle length for intradermal delivery of vaccines. *Vaccine*, 25(34):6423–6430, aug 2007.

[115] I. Lazarou, S. Nikolopoulos, P. C. Petrantonakis, I. Kompatsiaris, and M. Tsolaki. EEG-Based Brain–Computer Interfaces for Communication and Rehabilitation of People with Motor Impairment: A Novel Approach of the 21st Century. *Frontiers in Human Neuroscience*, 12, jan 2018.

[116] G. Lazzi. Thermal effects of bioimplants. *IEEE Engineering in Medicine and Biology Magazine*, 24(5):75–81, 2005.

[117] B. Lee, D. Kramer, M. Armenta Salas, S. Kellis, D. Brown, T. Dobreva, C. Klaes, C. Heck, C. Liu, and R. A. Andersen. Engineering Artificial Somatosensation Through Cortical Stimulation in Humans. *Frontiers in Systems Neuroscience*, 12, jun 2018.

[118] M. C. Lee, A. Karimi-Bidhendi, O. Malekzadeh-Arasteh, P. T. Wang, A. H. Do, Z. Nenadic, and P. Heydari. A CMOS MedRadio transceiver with supply-modulated power saving technique for an implantable brain-machine interface system. *IEEE Journal of Solid-State Circuits*, 54(6):1541–1552, 2019.

[119] S. M. C. Lee, W. J. Williams, and S. M. Schneider. Role of skin blood flow and sweating rate in exercise thermoregulation after bed rest. *Journal of Applied Physiology*, 92(5):2026–2034, may 2002.

[120] R. Leeb, D. Friedman, G. R. Müller-Putz, R. Scherer, M. Slater, and G. Pfurtscheller. Self-Paced (Asynchronous) BCI Control of a Wheelchair in Virtual Environments: A Case Study with a Tetraplegic. *Computational Intelligence and Neuroscience*, 2007:1–8, 2007.

[121] D. Lesenfants, D. Habbal, Z. Lugo, M. Lebeau, P. Horki, E. Amico, C. Pokorny, F. Gómez, A. Soddu, G. Müller-Putz, S. Laureys, and Q. Noirhomme. An independent SSVEP-based brain–computer interface in locked-in syndrome. *Journal of Neural Engineering*, 11(3):035002, jun 2014.

[122] R. P. Lesser, N. E. Crone, and W. R. S. Webber. Subdural electrodes. *Clinical Neurophysiology*, 121(9):1376–1392, 2010.

[123] E. C. Leuthardt, G. Schalk, J. R. Wolpaw, J. G. Ojemann, and D. W. Moran. A brain–computer interface using electrocorticographic signals in humans. *Journal of Neural Engineering*, 1(2):63–71, jun 2004.

[124] J. Lim. *Bi-Directional Brain-Computer Interfaces: Stimulation Artifact Suppression Design and Walking Exoskeleton Implementation.* Phd thesis, UC Irvine, Irvine, CA, 2023. Available at `https://escholarship.org/uc/item/1976v36z`.

[125] J. Lim, P. T. Wang, S. J. Shaw, H. Gong, C. Y. Armacost, M.and Liu, A. H. Do, P. Heydari, and Z. Nenadic. Artifact propagation in subdural cortical electrostimulation: Characterization and modeling. *Frontiers in Neuroscience*, 16, oct 2022.

[126] C. Y. Liu. personal communication.

[127] G. Liu, H. Lin, X. Tang, K. Bergler, and X. Wang. Characterization of Thermal Transport in One-dimensional Solid Materials. *Journal of Visualized Experiments*, (83), jan 2014.

[128] H. Lorach, A. Galvez, V. Spagnolo, F. Martel, S. Karakas, N. Intering, M. Vat, O. Faivre, C. Harte, S. Komi, J. Ravier, T. Collin, L. Coquoz, I. Sakr, E. Baaklini, S. D. Hernandez-Charpak, G. Dumont, R. Buschman, N. Buse, T. Denison, I. van Nes, L. Asboth, A. Watrin, L. Struber, F. Sauter-Starace, L. Langar, V. Auboiroux, S. Carda, S. Chabardes, T. Aksenova, R. Demesmaeker, G. Charvet, J. Bloch, and G. Courtine. Walking naturally after spinal cord injury using a brain–spine interface. *Nature*, 618:126–133, may 2023.

[129] F. Lotte, L. Bougrain, A. Cichocki, M. Clerc, M. Congedo, A. Rakotomamonjy, and F. Yger. A review of classification algorithms for EEG-based brain–computer interfaces: a 10 year update. *Journal of Neural Engineering*, 15(3):031005, jun 2018.

[130] A. M. Lozano, N. Lipsman, H. Bergman, P. Brown, S. Chabardes, J. W. Chang, K. Matthews, C. C. McIntyre, T. E. Schlaepfer, M. Schulder, Y. Temel, J. Volkmann, and J. K. Krauss. Deep brain stimulation: current challenges and future directions. *Nature Reviews Neurology*, 15(3):148–160, 2019.

[131] S. J. Luck. Event-related potentials. In *APA handbook of research methods in psychology, Vol 1: Foundations, planning, measures, and psychometrics.*, pages 523–546. American Psychological Association, Washington, 2012.

[132] K. D. Maglić and D. Z. Pavičić. Thermal and Electrical Properties of Titanium Between 300 and 1900K. *International Journal of Thermophysics*, 22(6):1833–1841, 2001.

[133] A. Mahajan, A. K. Bidhendi, P. T. Wang, C. M. McCrimmon, C. Y. Liu, Z. Nenadic, A. H. Do, and P. Heydari. A 64-channel ultra-low power bioelectric signal acquisition system for brain-computer interface. *IEEE Biomedical Circuits and Systems Conference: Engineering for Healthy Minds and Able Bodies, BioCAS 2015 - Proceedings*, pages 3–6, 2015.

[134] H. A. Mahinda and O. P. Murty. Variability in thickness of human skull bones and sternum - An autopsy experience. *Journal of Forensic Medicine and Toxicology*, 26(2):26–31, 2009.

[135] O. Malekzadeh-Arasteh, H. Pu, J. Lim, C. Y. Liu, A. H. Do, Z. Nenadic, and P. Heydari. An Energy-Efficient CMOS Dual-Mode Array Architecture for High-Density ECoG-based Brain-Machine Interfaces. *IEEE Transactions on Biomedical Circuits and Systems*, pages 1–11, 2019.

[136] F. Manzouri, M. Zöllin, S. Schillinger, M. Dümpelmann, R. Mikut, P. Woias, L. M. Comella, and A. Schulze-Bonhage. A Comparison of Energy-Efficient Seizure Detectors for Implantable Neurostimulation Devices. *Frontiers in Neurology*, 12, mar 2022.

[137] W. W. Mapleson. An electric analogue for uptake and exchange of inert gases and other agents. *Journal of Applied Physiology*, 18(1):197–204, jan 1963.

[138] H. Matsuki, T. Matsuzaki, and T. Satoh. Simulations of temperature rise on transcutaneous energy transmission by non-contact energy transmitting coils. *IEEE Transactions on Magnetics*, 29(6):3334–3336, nov 1993.

[139] H. McCann, G. Pisano, and L. Beltrachini. Variation in Reported Human Head Tissue Electrical Conductivity Values. *Brain Topography*, 32(5):825–858, sep 2019.

[140] C. M. McCrimmon, P. T. Wang, P. Heydari, A. Nguyen, S. J. Shaw, H. Gong, L. A. Chui, C. Y. Liu, Z. Nenadic, and A. H. Do. Electrocorticographic Encoding of Human Gait in the Leg Primary Motor Cortex. *Cerebral Cortex*, 28(8):2752–2762, aug 2018.

[141] D. J. McFarland, L. M. McCane, S. V. David, and J. R. Wolpaw. Spatial filter selection for EEG-based communication. *Electroencephalography and Clinical Neurophysiology*, 103(3):386–394, 1997.

[142] R. L. McIntosh and V. Anderson. A Comprehensive Tissue Properties Database Provided for the Thermal Assessment of a Human at Rest. *Biophysical Reviews and Letters*, 05(03):129–151, sep 2010.

[143] I. D. McRury and D. E. Haines. Ablation for the treatment of arrhythmias. *Proceedings of the IEEE*, 84(3):404–416, 1996.

[144] J. Mellinger, G. Schalk, C. Braun, H. Preissl, W. Rosenstiel, N. Birbaumer, and A. Kübler. An MEG-based brain–computer interface (BCI). *NeuroImage*, 36(3):581–593, 2007.

[145] M. Mohr, E. Abrams, C. Engel, W. B. Long, and M. Bottlang. Geometry of human ribs pertinent to orthopedic chest-wall reconstruction. *Journal of Biomechanics*, 40(6):1310–1317, jan 2007.

[146] S. A. Mohsin. Concentration of the Specific Absorption Rate Around Deep Brain Stimulation Electrodes During MRI. *Progress In Electromagnetics Research*, 121:469–484, 2011.

[147] J. Monzée, Y. Lamarre, and A. M. Smith. The Effects of Digital Anesthesia on Force Control Using a Precision Grip. *Journal of Neurophysiology*, 89(2):672–683, feb 2003.

[148] M. J. Morrell. Responsive cortical stimulation for the treatment of medically intractable partial epilepsy. *Neurology*, 77(13):1295–1304, sep 2011.

[149] S. R. Mousavi, S. Estaji, H. Kiaei, M. Mansourian-Tabaei, S. Nouranian, S. H. Jafari, H. Ruckdäschel, M. Arjmand, and H. A. Khonakdar. A review of electrical and thermal conductivities of epoxy resin systems reinforced with carbon nanotubes and graphene-based nanoparticles. *Polymer Testing*, 112:107645, aug 2022.

[150] Y. Nakanishi, T. Yanagisawa, D. Shin, R. Fukuma, C. Chen, H. Kambara, N. Yoshimura, M. Hirata, T. Yoshimine, and Y. Koike. Prediction of Three-Dimensional Arm Trajectories Based on ECoG Signals Recorded from Human Sensorimotor Cortex. *PLoS ONE*, 8(8):e72085, aug 2013.

[151] R. Narayanamoorthi. Modeling of Capacitive Resonant Wireless Power and Data Transfer to Deep Biomedical Implants. *IEEE Transactions on Components, Packaging and Manufacturing Technology*, 9(7):1253–1263, jul 2019.

[152] C. Neuper, M. Wörtz, and G. Pfurtscheller. ERD/ERS patterns reflecting sensorimotor activation and deactivation. In C. Neuper and W. Klimesch, editors, *Event-Related Dynamics of Brain Oscillations*, volume 159 of *Progress in Brain Research*, pages 211–222. Elsevier, 2006.

[153] NeuroPace, Inc. RNS® System Physician Manual. `https://www.neuropace.com/wp-content/uploads/2021/02/neuropace-rns-system-manual-320.pdf`, 2017. Accessed: 2023-04-10.

[154] Y. Ni, S. Mulier, Y. Miao, L. Michel, and G. Marchal. A review of the general aspects of radiofrequency ablation. *Abdominal Imaging*, 30(4):381–400, 2005.

[155] V. Nirale. Evaluation of effective thermal conductivity in PCB. *IJRST*, 3:174–179, 2016.

[156] P. Nunez, R. Silberstein, P. Cadusch, R. Wijesinghe, A. Westdorp, and R. Srinivasan. A theoretical and experimental study of high resolution EEG based on surface Laplacians and cortical imaging. *Electroencephalography and Clinical Neurophysiology*, 90(1):40–57, jan 1994.

[157] B. Obermaier, C. Guger, and G. Pfurtscheller. Hidden Markov Models Used for the Offline Classification of EEG Data - Hidden Markov-Modelle, verwendet zur Offline-Klassifikation von EEG-Daten. *Biomedizinische Technik/Biomedical Engineering*, 44(6):158–162, 1999.

[158] Ohmite. Characteristics for ohmite axial-leaded resistor materials. `https://www.ohmite.com/axial-resistors-material-characteristics/`. Accessed: 2022-12-06.

[159] Y. Okazaki, C. R. Davies, T. Matsuyoshi, K. Fukamachi, K. E. Wika, and H. Harasaki. Heat from an implanted power source is mainly dissipated by blood perfusion. *ASAIO journal (American Society for Artificial Internal Organs : 1992)*, 43(5):M585–8, 1997.

[160] N. L. Opie, A. N. Burkitt, H. Meffin, and D. B. Grayden. Heating of the Eye by a Retinal Prosthesis: Modeling, Cadaver and In Vivo Study. *IEEE Transactions on Biomedical Engineering*, 59(2):339–345, feb 2012.

[161] N. A. Pelot, B. J. Thio, and W. M. Grill. Modeling Current Sources for Neural Stimulation in COMSOL. *Frontiers in Computational Neuroscience*, 12, jun 2018.

[162] H. H. Pennes. Analysis of Tissue and Arterial Blood Temperatures in the Resting Human Forearm. *Journal of Applied Physiology*, 1(2):93–122, aug 1948.

[163] O. A. Petroff, D. D. Spencer, I. I. Goncharova, and H. P. Zaveri. A comparison of the power spectral density of scalp EEG and subjacent electrocorticograms. *Clinical Neurophysiology*, 127(2):1108–1112, feb 2016.

[164] G. Pfurtscheller, D. Flotzinger, and J. Kalcher. Brain-Computer Interface—a new communication device for handicapped persons. *Journal of Microcomputer Applications*, 16(3):293–299, jul 1993.

[165] G. Pfurtscheller and F. Lopes da Silva. Event-related EEG/MEG synchronization and desynchronization: basic principles. *Clinical Neurophysiology*, 110(11):1842–1857, nov 1999.

[166] T. Pistohl, T. Ball, A. Schulze-Bonhage, A. Aertsen, and C. Mehring. Prediction of arm movement trajectories from ECoG-recordings in humans. *Journal of Neuroscience Methods*, 167(1):105–114, jan 2008.

[167] R. Powell and R. Tye. The thermal and electrical conductivity of titanium and its alloys. *Journal of the Less-Common Metals*, 3(3):226–233, jun 1961.

[168] W. S. Pritchard. Psychophysiology of P300. *Psychological Bulletin*, 89(3):506–540, 1981.

[169] N. A. A. Qasem, M. M. Generous, B. A. Qureshi, and S. M. Zubair. A Comprehensive Review of Saline Water Correlations and Data: Part II—Thermophysical Properties. *Arabian Journal for Science and Engineering*, 46(3):1941–1979, mar 2021.

[170] A. Rakotomamonjy, V. Guigue, G. Mallet, and V. Alvarado. Ensemble of SVMs for Improving Brain Computer Interface P300 Speller Performances. In W. Duch, J. Kacprzyk, E. Oja, and S. Zadrożny, editors, *Artificial Neural Networks: Biological Inspirations – ICANN 2005*, pages 45–50, Berlin, Heidelberg, 2005. Springer Berlin Heidelberg.

[171] N. F. Ramsey, E. Salari, E. J. Aarnoutse, M. J. Vansteensel, M. G. Bleichner, and Z. V. Freudenburg. Decoding spoken phonemes from sensorimotor cortex with high-density ecog grids. *Neuroimage*, 180:301–311, 2018.

[172] A. G. Rouse, S. R. Stanslaski, P. Cong, R. M. Jensen, P. Afshar, D. Ullestad, R. Gupta, G. F. Molnar, D. W. Moran, and T. J. Denison. A chronic generalized bi-directional brain–machine interface. *Journal of Neural Engineering*, 8(3):036018, jun 2011.

[173] J. C. Sanchez, A. Gunduz, P. R. Carney, and J. C. Principe. Extraction and localization of mesoscopic motor control signals for human ECoG neuroprosthetics. *Journal of Neuroscience Methods*, 167(1):63–81, 2008.

[174] T. D. Sanger. Bayesian Filtering of Myoelectric Signals. *Journal of Neurophysiology*, 97(2):1839–1845, feb 2007.

[175] C. Sarica, C. Iorio-Morin, D. H. Aguirre-Padilla, A. Najjar, M. Paff, A. Fomenko, K. Yamamoto, A. Zemmar, N. Lipsman, G. M. Ibrahim, C. Hamani, M. Hodaie, A. M. Lozano, R. P. M., A. Fasano, and S. K. Kalia. Implantable Pulse Generators for Deep Brain Stimulation: Challenges, Complications, and Strategies for Practicality and Longevity. *Frontiers in Human Neuroscience*, 15, 2021.

[176] G. Schalk and E. C. Leuthardt. Brain-Computer Interfaces Using Electrocorticographic Signals. *IEEE Reviews in Biomedical Engineering*, 4:140–154, 2011.

[177] M. H. Schieber. Constraints on Somatotopic Organization in the Primary Motor Cortex. *Journal of Neurophysiology*, 86(5):2125–2143, nov 2001.

[178] N. Sekiya, H. Nagasaki, H. Ito, and T. Furuna. Optimal Walking in Terms of Variability in Step Length. *Journal of Orthopaedic & Sports Physical Therapy*, 26(5):266–272, 1997.

[179] J. Seo, J. Jeon, J.-H. Lee, and S. Kim. Thermal performance analysis according to wood flooring structure for energy conservation in radiant floor heating systems. *Energy and Buildings*, 43(8):2039–2042, aug 2011.

[180] C. Serrano-Amenos, F. Hu, P. T. Wang, P. Heydari, A. H. Do, and Z. Nenadic. Simulation-informed Power Budget Estimate of a Fully Implantable Brain-Computer Interface. Under Review.

[181] C. Serrano-Amenos, F. Hu, P. T. Wang, S. Kellis, R. A. Andersen, C. Y. Liu, P. Heydari, A. H. Do, and Z. Nenadic. Thermal Analysis of a Skull Implant in Brain-Computer Interfaces. In *2020 42nd Annual International Conference of the IEEE Engineering in Medicine & Biology Society (EMBC)*, pages 3066–3069. IEEE, jul 2020.

[182] R. A. Serway. *Principles of physics*. Brooks/Cole, 2 edition, 1997.

[183] A. L. Sette, E. Seigneuret, F. Reymond, S. Chabardes, A. Castrioto, B. Boussat, E. Moro, P. François, and V. Fraix. Battery longevity of neurostimulators in Parkinson disease: A historic cohort study. *Brain Stimulation*, 12(4):851–857, 2019.

[184] K. M. Silay, C. Dehollain, and M. Declercq. Numerical Thermal Analysis of a Wireless Cortical Implant with Two-Body Packaging. *BioNanoScience*, 1(3):78–88, sep 2011.

[185] M. A. Silberbusch, M. I. Rothman, G. K. Bergey, G. H. Zoarski, and M. T. Zagardo. Subdural grid implantation for intracranial EEG recording: CT and MR appearance. *AJNR. American journal of neuroradiology*, 19(6):1089–93, 1998.

[186] K. A. Sillay, P. Rutecki, K. Cicora, G. Worrell, J. Drazkowski, J. J. Shih, A. D. Sharan, M. J. Morrell, J. Williams, and B. Wingeier. Long-Term Measurement of Impedance in Chronically Implanted Depth and Subdural Electrodes During Responsive Neurostimulation in Humans. *Brain Stimulation*, 6(5):718–726, sep 2013.

[187] J. D. Simeral, S.-P. Kim, M. J. Black, J. P. Donoghue, and L. R. Hochberg. Neural control of cursor trajectory and click by a human with tetraplegia 1000 days after implant of an intracortical microelectrode array. *Journal of Neural Engineering*, 8(2):025027, apr 2011.

[188] S. P. Singh. Magnetoencephalography: Basic principles. *Annals of Indian Academy of Neurology*, 17(5):107, 2014.

[189] R. Sitaram, A. Caria, R. Veit, T. Gaber, G. Rota, A. Kuebler, and N. Birbaumer. fMRI Brain-Computer Interface: A Tool for Neuroscientific Research and Treatment. *Computational Intelligence and Neuroscience*, 2007:1–10, 2007.

[190] G. A. Slack. Platinum as a Thermal Conductivity Standard. *Journal of Applied Physics*, 35(2):339–344, feb 1964.

[191] M. W. Slutzky, L. R. Jordan, E. W. Lindberg, K. E. Lindsay, and L. E. Miller. Decoding the rat forelimb movement direction from epidural and intracortical field potentials. *Journal of neural engineering*, 8(3):036013, 2011.

[192] W. J. Sohn, J. Lim, P. T. Wang, H. Pu, O. Malekzadeh-Arasteh, S. J. Shaw, M. Armacost, H. Gong, S. Kellis, R. A. Andersen, C. Y. Liu, P. Heydari, Z. Nenadic, and A. H. Do. Benchtop and bedside validation of a low-cost programmable cortical stimulator in a testbed for bi-directional brain-computer-interface research. *Frontiers in Neuroscience*, 16, jan 2023.

[193] R. A. Stine. Graphical Interpretation of Variance Inflation Factors. *The American Statistician*, 49(1):53–56, feb 1995.

[194] P. Störchle, W. Müller, M. Sengeis, S. Lackner, S. Holasek, and A. Fürhapter-Rieger. Measurement of mean subcutaneous fat thickness: eight standardised ultrasound sites compared to 216 randomly selected sites. *Scientific Reports*, 8(1):16268, dec 2018.

[195] R. B. Strother, G. B. Trophe, J. J. Mrva, and D. R. Pack. Implantable pulse generator systemis and methods for providing functional and/or therapeutc stmulation of muscles and/or nerves and/or central nervous system tissue, Mar 2007.

[196] Technical Products, Inc. `https://www.technicalproductsinc.com`. Accessed: 2022-12-06.

[197] L. Trejo, R. Rosipal, and B. Matthews. Brain-computer interfaces for 1-D and 2-D cursor control: designs using volitional control of the EEG spectrum or steady-state visual evoked potentials. *IEEE Transactions on Neural Systems and Rehabilitation Engineering*, 14(2):225–229, jun 2006.

[198] M. J. Vansteensel and B. Jarosiewicz. Chapter 7 - Brain-computer interfaces for communicationaCurrent affiliation: NeuroPace, Inc., Mountain View, CA, United States. In N. F. Ramsey and J. del R. Millán, editors, *Brain-Computer Interfaces*, volume 168 of *Handbook of Clinical Neurology*, pages 67–85. Elsevier, 2020.

[199] M. Velliste, S. Perel, M. C. Spalding, A. S. Whitford, and A. B. Schwartz. Cortical control of a prosthetic arm for self-feeding. *Nature*, 453(7198):1098–1101, jun 2008.

[200] K. Volkova, M. A. Lebedev, A. Kaplan, and A. Ossadtchi. Decoding Movement From Electrocorticographic Activity: A Review. *Frontiers in Neuroinformatics*, 13, 2019.

[201] G. Walckiers, B. Fuchs, J.-P. Thiran, J. R. Mosig, and C. Pollo. Influence of the implanted pulse generator as reference electrode in finite element model of monopolar deep brain stimulation. *Journal of Neuroscience Methods*, 186(1):90–96, jan 2010.

[202] F. T. Wallenberger and P. A. Bingham, editors. *Fiberglass and Glass Technology*. Springer US, Boston, MA, 2010.

[203] D. Wang, Q. Zhang, Y. Li, Y. Wang, J. Zhu, S. Zhang, and X. Zheng. Long-term decoding stability of local field potentials from silicon arrays in primate motor cortex during a 2D center out task. *Journal of Neural Engineering*, 11(3):036009, jun 2014.

[204] H. Wang, B. Wang, K. P. Normoyle, K. Jackson, K. Spitler, M. Sharrock, C. M. Miller, C. Best, D. Llano, and R. Du. Brain temperature and its fundamental properties: A review for clinical neuroscientists. *Front. Neurosci.*, 8:307, 2014.

[205] P. T. Wang, E. Camacho, M. Wang, Y. Li, S. J. Shaw, M. Armacost, H. Gong, D. Kramer, B. Lee, R. A. Andersen, C. Y. Liu, P. Heydari, Z. Nenadic, and A. H. Do. A benchtop system to assess the feasibility of a fully independent and implantable brain-machine interface. *Journal of Neural Engineering*, 16(6), 2019.

[206] P. T. Wang, C. E. King, C. M. McCrimmon, J. J. Lin, M. Sazgar, F. P. K. Hsu, S. J. Shaw, D. E. Millet, L. A. Chui, C. Y. Liu, A. H. Do, and Z. Nenadic. Comparison of decoding resolution of standard and high-density electrocorticogram electrodes. *Journal of Neural Engineering*, 13(2):026016, apr 2016.

[207] P. T. Wang, C. M. McCrimmon, C. E. King, S. J. Shaw, D. E. Millett, H. Gong, L. A. Chui, C. Y. Liu, Z. Nenadic, and A. H. Do. Characterization of electrocorticogram high-gamma signal in response to varying upper extremity movement velocity. *Brain Structure and Function*, 222(8):3705–3748, nov 2017.

[208] P. T. Wang, C. M. McCrimmon, S. J. Shaw, H. Gong, L. A. Chui, P. Heydari, C. Y. Liu, A. H. Do, and Z. Nenadic. Decoding of the walking states and step rates from cortical electrocorticogram signals, 2021.

[209] P. T. Wang, C. M. McCrimmon, S. J. Shawbcd, H. Gong, L. A. Chui, P. Heydari, C. Y. Liu, A. H. Do, and Z. Nenadic. Decoding of the walking states and step rates from cortical electrocorticogram signals. *arXiv preprint arXiv:2104.07062*, 2021.

[210] P. T. Wang, E. J. Puttock, C. E. King, A. Schombs, J. J. Lin, M. Sazgar, F. P. Hsu, S. J. Shaw, D. E. Millett, C. Y. Liu, L. A. Chui, A. H. Do, and Z. Nenadic. State and trajectory decoding of upper extremity movements from electrocorticogram. In *2013 6th International IEEE/EMBS Conference on Neural Engineering (NER)*, pages 969–972, 2013.

[211] Y. Wang, X. Gao, B. Hong, C. Jia, and S. Gao. Brain-Computer Interfaces Based on Visual Evoked Potentials. *IEEE Engineering in Medicine and Biology Magazine*, 27(5):64–71, sep 2008.

[212] Y. Wang and T.-P. Jung. A Collaborative Brain-Computer Interface for Improving Human Performance. *PLoS ONE*, 6(5):e20422, may 2011.

[213] Y. Wang, H. Lu, S. Li, Y. Zhang, F. Yan, Y. Huang, X. Chen, A. Yang, L. Han, and Y. Ma. Effect of cold and heat therapies on pain relief in patients with delayed onset muscle soreness: A network meta-analysis. *Journal of Rehabilitation Medicine*, 54:jrm00258, feb 2022.

[214] Z. Wang, A. Gunduz, P. Brunner, A. Ritaccio, Q. Ji, and G. Schalk. Decoding onset and direction of movements using Electrocorticographic (ECoG) signals in humans. *Frontiers in Neuroengineering*, 5, 2012.

[215] Z. Wang, Z. Ying, A. Bosy-Westphal, J. Zhang, B. Schautz, W. Later, S. B. Heymsfield, and M. J. Müller. Specific metabolic rates of major organs and tissues across adulthood: evaluation by mechanistic model of resting energy expenditure. *The American Journal of Clinical Nutrition*, 92(6):1369–1377, dec 2010.

[216] E. M. Whitham, K. J. Pope, S. P. Fitzgibbon, T. Lewis, C. R. Clark, S. Loveless, M. Broberg, A. Wallace, D. DeLosAngeles, P. Lillie, A. Hardy, R. Fronsko, A. Pulbrook, and J. O. Willoughby. Scalp electrical recording during paralysis: Quantitative evidence that EEG frequencies above 20Hz are contaminated by EMG. *Clinical Neurophysiology*, 118(8):1877–1888, aug 2007.

[217] M. Wieser, J. Haefeli, L. Bütler, L. Jäncke, R. Riener, and S. Koeneke. Temporal and spatial patterns of cortical activation during assisted lower limb movement. *Experimental Brain Research*, 203(1):181–191, may 2010.

[218] L. R. Williams and R. W. Leggett. Reference values for resting blood flow to organs of man. *Clinical Physics and Physiological Measurement*, 10(3):187–217, 1989.

[219] L. Winter, F. Seifert, L. Zilberti, M. Murbach, and B. Ittermann. MRI-Related Heating of Implants and Devices: A Review. *Journal of Magnetic Resonance Imaging*, 53(6):1646–1665, jun 2021.

[220] P. D. Wolf. Thermal Considerations for the Design of an Implanted Cortical Brain–Machine Interface (BMI). In W. M. Reichert, editor, *Indwelling Neural Implants: Strategies for Contending with the In Vivo Environment*, pages 1–20. CRC Press/Taylor & Francis, 2008.

[221] J. R. Wolpaw and D. J. McFarland. Control of a two-dimensional movement signal by a noninvasive brain-computer interface in humans. *Proceedings of the National Academy of Sciences*, 101(51):17849–17854, dec 2004.

[222] J. M. Workman and B. W. Armstrong. Oxygen cost of treadmill walking. *Journal of Applied Physiology*, 18(4):798–803, jul 1963.

[223] T. Yanagisawa, M. Hirata, Y. Saitoh, T. Goto, H. Kishima, R. Fukuma, H. Yokoi, Y. Kamitani, and T. Yoshimine. Real-time control of a prosthetic hand using human electrocorticography signals. *Journal of Neurosurgery*, 114(6):1715–1722, jun 2011.

[224] C. Yao, J. Lu, and T. Webster. Titanium and cobalt–chromium alloys for hips and knees. In M. Lysaght and T. J. Webster, editors, *Biomaterials for Artificial Organs*, Woodhead Publishing Series in Biomaterials, pages 34–55. Elsevier, 2011.

[225] Z. Ye, C. M. Wells, C. G. Carrington, and N. J. Hewitt. Thermal conductivity of wool and wool–hemp insulation. *International Journal of Energy Research*, 30(1):37–49, 2006.

[226] N. Yousif and X. Liu. Investigating the depth electrode–brain interface in deep brain stimulation using finite element models with graded complexity in structure and solution. *Journal of Neuroscience Methods*, 184(1):142–151, oct 2009.

[227] T. O. Zander and C. Kothe. Towards passive brain–computer interfaces: applying brain–computer interface technology to human–machine systems in general. *Journal of Neural Engineering*, 8(2):025005, apr 2011.

[228] J. Zhang, D. Liu, W. Chen, Z. Pei, and J. Wang. Deep Convolutional Neural Network for EEG-Based Motor Decoding. *Micromachines*, 13(9):1485, sep 2022.

[229] D. Zhu, J. Bieger, G. Garcia Molina, and R. M. Aarts. A Survey of Stimulation Methods Used in SSVEP-Based BCIs. *Computational Intelligence and Neuroscience*, 2010:1–12, 2010.

Appendix A

MATLAB Code of the Step Decoder

```
% Step Decoder based on Logistic Regressions and Jump Diffusion Bayesian
% Filter

function [out]=individual_step_decoder(exp_name,epsilon)

%%%%%%%%%%%%%%%%%%%%%%%%%%%%%%%%%%%%%%%%%%%%
%%% INPUTS:
% exp_name: string, experiment name
% epsilon: float, width of x bins

%%% OUTPUTS:
% out: struct, includes multiple fields, including MAP (decoder output),
    gyroscope
% downsampled to 20 Hz, precision and sensitivity metrics
%%%%%%%%%%%%%%%%%%%%%%%%%%%%%%%%%%%%%%%%%%%%

% Define Parameters and Constants
% Frequency bands
beta_band_fq = [20,40];
gamma_band_fq = [40,160];
```

```
high_gamma_band_fq = [80,160];

% Gyro Pre-processing
th_percentage = 0.15; % Percentage of the maximum gyro value that should
    be set to 0
% Gyro Binarization
th_percentage_step_height = 0.1; % Minimum percentage height (of the
    heighest step) to be considered a step
% Train/test split
test_time = 5; % Length of test data in seconds
% PCA Training
variance_threshold = 0.03; % How much of the variance should a Principal
    Component explain to be retained
% Decoder
downsample_factor = 13; % Fs/Downsampling factor is the final decoder rate
     (256/4 = 64 Hz)
ratemax = 1;        % max value of decoder output
noutputs = round(1/epsilon);      % Decoder output quantization levels
x_bins = linspace(ratemax/noutputs, ratemax, noutputs)'; % Quantization
    bins
% Measurement model
jump_thresh = 0.05; % Threshold that indicates a jump in gyro data is a
    step
slope = 25; % Slope of the logistic function

lp_state_fq = 0.12;

% 1. Load Data
[ecog_raw,gyro_raw,Fs,ch_index]=load_exp_data(exp_name);

% 2. Pre-process ECoG
[beta_envelope,gamma_envelope,high_gamma_envelope]= preprocess_ecog2(
    ecog_raw,beta_band_fq,gamma_band_fq,high_gamma_band_fq,Fs,lp_state_fq);
```

```
46
47 % Cut Gyro to ECoG length (ECoG ends at whole seconds, gyro doesn't)
48 gyro_raw(length(beta_envelope)+1:end) = [];
49
50 % SJ2 has gyro upside-down compared to SJ1
51 if contains(exp_name,'3')
52     gyro_raw = -gyro_raw;
53 end
54
55 % 3. Pre-process gyro
56 % gyro = preprocess_gyro2(gyro_raw,th_percentage);
57
58 % 4. Binarize/normalize gyro
59 [bin_state,bin_steps,normalized_steps]=binarize_gyro2(gyro_raw,Fs(2),
    exp_name);
60
61 % Cross-validation iterations
62 start_test_index_vec = 1:Fs(2)*test_time:size(gyro_raw,1); % Vector with
    the different start indeces for testing data in cross-validation
63 prior = ones(noutputs,1)/noutputs;            % Start with uniform prior
    prob. dist.
64 MAP = zeros(floor(length(beta_envelope)/downsample_factor),1);
65
66 for i = 1:size(start_test_index_vec,2)
67
68     start_test_index = start_test_index_vec(i);
69     % 5. Train/test split
70     [bin_state_train,~] = train_test_split(bin_state,test_time,Fs(2),
    start_test_index);
71     [bin_steps_train,~] = train_test_split(bin_steps,test_time,Fs(2),
    start_test_index);
72     [normalized_steps_train,~] = train_test_split(normalized_steps,
    test_time,Fs(2),start_test_index);
```

```
73
74    [beta_envelope_train,beta_envelope_test] = train_test_split(
      beta_envelope,test_time,Fs(2),start_test_index);
75    [gamma_envelope_train,gamma_envelope_test] = train_test_split(
      gamma_envelope,test_time,Fs(2),start_test_index);
76    [high_gamma_envelope_train,high_gamma_envelope_test] =
      train_test_split(high_gamma_envelope,test_time,Fs(2),start_test_index);
77
78    % 6. Logistic Regression - Trainingt
79    % 6.1. PCA for State
80    [pc_train,pca_coeffs] = pca_train([beta_envelope_train,
      gamma_envelope_train],variance_threshold);
81
82    % 6.2. Log Reg for State
83    [logreg_coeffs_state,logreg_feature_state_train]= logreg_train(
      pc_train,bin_state_train);
84    % 6.3. Log Reg for Steps
85    [logreg_coeffs_steps,logreg_feature_steps_train]= logreg_train(
      high_gamma_envelope_train,bin_steps_train);
86    % 6.4. Extracted Feature Computation: multiply logreg outputs (train
      only)
87    ecog_feature_train = logreg_feature_state_train.*
      logreg_feature_steps_train;
88
89    % 7. Bayesian Filter - Training
90    % 7.1. Downsample ECoG feature and Gyro (ground truth)
91    ecog_feature_train_down = downsample_split_data(ecog_feature_train,
      downsample_factor,i);
92    normalized_steps_train_down = downsample_split_data(
      normalized_steps_train,downsample_factor,i);
93    thr_gyro = min(normalized_steps_train(normalized_steps_train>0));
94    normalized_steps_train_down(normalized_steps_train_down<thr_gyro)=0;
95
```

```
96    % 7.2. Measurement Model Training
97    [m,~] = measurement_model_train(ecog_feature_train_down,
      normalized_steps_train_down,x_bins,slope);
98
99    % 7.3. Fokker-Plank based Bayesian Training
100   % [alpha,beta] = alpha_beta_train(normalized_steps_train,
      bin_steps_train,downsample_factor);
101   [alpha,beta] = alpha_beta_train(normalized_steps_train,bin_steps_train
      ,downsample_factor,epsilon,Fs(2));
102
103   % 8. Decoder Testing
104   % 8.1. PCA
105   pc_test = [beta_envelope_test,gamma_envelope_test]*pca_coeffs;
106
107   % 8.2. Log Transformationg State
108   logreg_feature_state_test = logistic(logreg_coeffs_state,pc_test);
109
110   % 8.3. Log Transformationg Steps
111   logreg_feature_steps_test = logistic(logreg_coeffs_steps,
      high_gamma_envelope_test);
112
113   % 8.4. ECoG Feature - Test
114   ecog_feature_test = logreg_feature_state_test.*
      logreg_feature_steps_test;
115
116   % 8.5. Downsample Test Data
117   ecog_feature_test_down = downsample_split_data(ecog_feature_test,
      downsample_factor,1);
118
119   % 8.6. Filter (iterations)
120   start_test_index_down = floor((start_test_index-1)/downsample_factor);
121
122   for t = 1:length(ecog_feature_test_down)
```

```
123
124         % New Reading
125         ecog_val = ecog_feature_test_down(t);
126         % Filter
127         [prior,MAP_idx]= fokker_bayesian_filter(prior,ecog_val,alpha,beta,
    m,noutputs);
128         % MAP value
129         MAP(t+start_test_index_down) = (ratemax / (noutputs-1))*MAP_idx;
130
131     end
132 end
133
134 % 9. Decoder Performance
135
136 % 9.1. Downsample gyro (ground truth)
137 gyro_down = normalized_steps(1:downsample_factor:length(normalized_steps))
    ;
138 [sensitivity1,precision1] = performance_decoder(gyro_down,MAP,0.05);
139
140 out.sensitivity = sensitivity1;
141 out.precision = precision1;
142 out.gyro = normalized_steps;
143 out.gyro_raw = gyro_raw;
144 out.bin_steps = bin_steps;
145 out.map = MAP;
146
147 end
```

```
1 function [ecog,gyro,Fs,ch_index]=load_exp_data(exp_name)
2
3 %%%%%%%%%%%%%%%%%%%%%%%%%%%%%%%%%%%%%%%%%%%%%%%%
4 %%% INPUTS:
5 % exp_name: experiment name string (main1, main2, main3, idle_walk_1,
```

```
    idle_walk_2 , idle_walk_3)

%%% OUTPUTS:
% ecog:  N x ch, matrix with raw ECoG data
% gyro: n x 1, matrix with raw gyro data
% Fs: 1 x 2, with Fs(1) = ECoG sampling rate, Fs(2) = gyro sampling rate
% ch_index: 1 x ch, indexes of the selected ECoG channels
%%%%%%%%%%%%%%%%%%%%%%%%%%%%%%%%%%%%%%%%%%%%

% Get file names where experimenta data is stored and ECoG channel indexes
% for the corresponding experiment name
[file_name1,file_name2,ch_good]=files_and_channels(exp_name);

% Load Gyro
load(file_name1,'Fs','physics')

% Load ECoG
load(file_name2,'eeg','eegchannames')
ChanNames = eegchannames;

% Choose selected ECoG channels (based on ch_good)
ecog_selected = nan(size(eeg,1),size(ch_good,2));
ch_n = nan(1,size(ch_good,2));

for i=1:length(ch_good)
    n = string(['MG',num2str(ch_good(i))]);
    ind = find(ChanNames==n);
    if isempty(ind)==0
        ecog_selected(:,i) = eeg(:,ind);
        ch_n(i) = ch_good(i);
    end
end

```

```
ch_index = ch_good;
ecog = ecog_selected;
% Get tibial gyroscope signal
gyro = physics(:,3);

end
```

```
function [beta_envelope,gamma_envelope,high_gamma_envelope]=
    preprocess_ecog2(ecog_raw,beta_band_fq,gamma_band_fq,high_gamma_band_fq
    ,Fs,lp_state_fq)

%%%%%%%%%%%%%%%%%%%%%%%%%%%%%%%%%%%%%%%%%%%%
%%% INPUTS:
% ecog_raw:  N x ch, matrix with raw ECoG data
% beta_band_fq: 1 x 2, beta band frequency bounds
% gamma_band_fq: 1 x 2, gamma band frequency bounds
% high_gamma_band_fq: 1 x 2, high gamma band frequency bounds
% Fs: 1 x 2, sampling rate of ECoG and gyro
% lp_state_fq: float, Low Pass Frequency to Filter Beta and Gamma Power
% Envelopes

%%% OUTPUTS:
% beta_envelope:  n x ch, matrix with beta envelope for each ECoG channel,
% downsampled to gyro sampling rate
% gamma_envelope:  n x ch, matrix with gamma envelope for each ECoG
    channel,
% downsampled to gyro sampling rate
% high_gamma_envelope:  n x ch, matrix with high gamma envelope for each
    ECoG channel,
% downsampled to gyro sampling rate
%%%%%%%%%%%%%%%%%%%%%%%%%%%%%%%%%%%%%%%%%%%%
ecog_raw = ecog_raw - mean(ecog_raw);

```

```
% Beta Fq: Power Envelope Computation
beta_power = nan(size(ecog_raw));
% Power Computation
for i=1:size(ecog_raw,2)
    beta_band = freqfilter(ecog_raw(:,i),Fs(1),[beta_band_fq(1)
    beta_band_fq(2) 4],'band','butter');
    beta_power(:,i) = beta_band.^2;
end
beta_power_r = resample(beta_power,Fs(2),Fs(1)); % Downsample
beta_envelope = freqfilter(beta_power_r,Fs(2),[lp_state_fq 4],'low','
    butter'); % LP filter

% Gamma Fq: Power Envelope Computation
gamma_power = nan(size(ecog_raw));
% Power Computation
for i=1:size(ecog_raw,2)
    gamma_band = freqfilter(ecog_raw(:,i),Fs(1),[gamma_band_fq(1)
    gamma_band_fq(2) 4],'band','butter');
    gamma_power(:,i) = gamma_band.^2;
end
gamma_power_r = resample(gamma_power,Fs(2),Fs(1));
gamma_envelope = freqfilter(gamma_power_r,Fs(2),[0.12 4],'low','butter');
    % LP filter

% High-gamma Fq: Power Envelope Computation
high_gamma_power = nan(size(ecog_raw));
% Power Computation
for i=1:size(ecog_raw,2)
    high_gamma_band = freqfilter(ecog_raw(:,i),Fs(1),[high_gamma_band_fq
    (1) high_gamma_band_fq(2) 4],'band','butter');
    high_gamma_power(:,i) = high_gamma_band.^2;
end
high_gamma_power_r = resample(high_gamma_power,Fs(2),Fs(1)); % Downsample
```

```
high_gamma_envelope = freqfilter(high_gamma_power_r,Fs(1),[[0.15 1.5] 4],'band','butter'); % BP filter

end
```

```
function [bin_state,bin_steps,normalized_steps]=binarize_gyro2(gyro_raw,Fs,exp_name)

%%%%%%%%%%%%%%%%%%%%%%%%%%%%%%%%%%%%%%%%%%%%
%%% INPUTS:
% gyro:  n x ch, matrix with gyro data
% Fs: int, gyro sampling rate (Hz)
% exp_name: string, experiment name

%%% OUTPUTS:
% bin_state:  n x ch, binarized state (IDLE/MOVE) data
% bin_steps:  n x ch, binarized individual steps data
% normalized_steps:  n x ch, normalized (max height = 1) individual steps data
%%%%%%%%%%%%%%%%%%%%%%%%%%%%%%%%%%%%%%%%%%%%

% BP filter
gyro = freqfilter(gyro_raw,Fs,[0.15 1.5 4],'band','butter');
% Only keep leg swings
gyro(gyro<0)=0;

% Identify each step
mph = max(gyro)*0.1;
mpd = 0.5*Fs;
% Peak detection
[height,loc,~,~] = findpeaks(gyro,'MinPeakHeight',mph,'MinPeakDistance',mpd);
% Remove false steps
```

```
index_remove = step_index_remove(exp_name);
loc(index_remove) = [];
height(index_remove) = [];

% Normalize each step
normalized_steps = gyro;
start_index = 1;
walk_idle_seg = [];

for i=1:length(loc)
    start_index_prev = start_index;
    start_index = find(gyro(start_index_prev:loc(i))==0,1,'last')+
   start_index_prev;
    normalized_steps(start_index_prev:start_index) = 0;
    end_index = find(gyro(loc(i):end)==0,1)+loc(i)-2;
    normalized_steps(start_index:end_index) = gyro(start_index:end_index)/
   height(i);

    if i==1 && loc(i+1)-loc(i)>0.75e3
        walk_idle_seg=[walk_idle_seg,start_index,end_index];
    elseif i==1
        walk_idle_seg = [walk_idle_seg,start_index];
    elseif i==length(loc) && loc(i)-loc(i-1)>0.75e3
        walk_idle_seg = [walk_idle_seg,start_index,end_index];
    elseif i==length(loc)
        walk_idle_seg = [walk_idle_seg,end_index];
    elseif loc(i)-loc(i-1)>0.75e3 && loc(i+1)-loc(i)>0.75e3
        walk_idle_seg = [walk_idle_seg,start_index,end_index];
    elseif loc(i+1)-loc(i)>0.75e3
        walk_idle_seg = [walk_idle_seg,end_index];
    elseif loc(i)-loc(i-1)>0.75e3
        walk_idle_seg = [walk_idle_seg,start_index];
    end
```

```
    start_index=end_index+1;

end

normalized_steps(start_index:end)=0;

% Binarize steps
bin_steps = normalized_steps>0.03;

% Binarize states
bin_state = zeros(size(normalized_steps));
for i=1:2:length(walk_idle_seg)
    bin_state(walk_idle_seg(i):walk_idle_seg(i+1))=bin_state(walk_idle_seg
   (i):walk_idle_seg(i+1))+1;
end

end
```

```
function [train_data,test_data]=train_test_split(orig_data,test_time,Fs,
   start_test_index)

%%%%%%%%%%%%%%%%%%%%%%%%%%%%%%%%%%%%%%%%%%%%
%%% INPUTS:
% orig_data:  n x ch, orig data that should be split
% test_time: int, length of test data in seconds
% Fs: int, sampling rate of the data
% start_test_index: int, index where test data starts

%%% OUTPUTS:
% train_data: split of data for training
% test_data: split of data for testing
%%%%%%%%%%%%%%%%%%%%%%%%%%%%%%%%%%%%%%%%%%%%

```

```
test_index = start_test_index:min(start_test_index+Fs*test_time-1,size(
    orig_data,1)); % Indicies to test with
train_index = [1:start_test_index-1,test_index(end)+1:size(orig_data,1)];
    % Indicers to train with

train_data = orig_data(train_index,:);
test_data = orig_data(test_index,:);

end
```

```
function [pc,pca_coeffs] = pca_train(data,variance_threshold)

%%%%%%%%%%%%%%%%%%%%%%%%%%%%%%%%%%%%%%%%%%%%%%%%
%%% INPUTS:
% data:  n x 2ch, beta and gamma envelopes (train only)
% variance_threshold: int, minimum variance that a PC must have to retain
% it and its coefficients

%%% OUTPUTS:
% pc: n x k, k principal components
% pca_coeffs: , principal components coefficients
%%%%%%%%%%%%%%%%%%%%%%%%%%%%%%%%%%%%%%%%%%%%%%%%

% PCA
[pca_coeffs_all,~,lat] = pca(data);

% Choose how many PCs to retain based on variance threshold
for i=1:length(lat)
    if lat(i)/sum(lat)<variance_threshold
        k=i-1;
        break;
    end
end
```

```

% Select first k pca coeffs and compute first k PCs
pca_coeffs = pca_coeffs_all(:,1:k);
pc = data*pca_coeffs;

end
```

```
function [logreg_coeffs,logreg_output]= logreg_train(data,ground_truth)

%%%%%%%%%%%%%%%%%%%%%%%%%%%%%%%%%%%%%%%%%%%%
%%% INPUTS:
% data: n x k, predictor data
% ground_truth: n x 1, binarized ground truth data

%%% OUTPUTS:
% logreg_coeffs: k+1, coefficients of the logistic regression
% logreg_output: n x 1, probability logistic regression outcome
%%%%%%%%%%%%%%%%%%%%%%%%%%%%%%%%%%%%%%%%%%%%

% Training the LogReg Coefficients
logreg_coeffs = glmfit(data,ground_truth, 'binomial', 'link', 'logit');

% Logistic Transformation to compute probability
logreg_output = logistic(logreg_coeffs,data);

end
```

```
function data_downsampled = downsample_split_data(data,downsample_factor,
    middle_index_split)

%%%%%%%%%%%%%%%%%%%%%%%%%%%%%%%%%%%%%%%%%%%%
%%% INPUTS:
% data: n x 1, original data sampled at org_fs
% downsample_factor: int, donwsample_factor = orig_fq/new_fq, where
```

```
% middle_index_split: int, index where the data is split

%%% OUTPUTS:
% data_downsampled: m x 1, data resampled at new_fs
%%%%%%%%%%%%%%%%%%%%%%%%%%%%%%%%%%%%%%%%%%%%%%%%

% If no split exists
if middle_index_split == 1
    data1 = [];
else
    data1 = resample(data(1:middle_index_split-1),1,downsample_factor);
end
% If no split exists
if middle_index_split == length(data)+1
    data2 = [];
else
    data2 = resample(data(middle_index_split:end),1,downsample_factor);
end
% Concatenate resampled data
data_downsampled = [data1;data2];
% Limit data between [0,1]
data_downsampled(data_downsampled>1)=1;
data_downsampled(data_downsampled<0)=0;

end
```

```
function [m2,x0]=measurement_model_train(ecog,gyro,bins,slope)

%%%%%%%%%%%%%%%%%%%%%%%%%%%%%%%%%%%%%%%%%%%%%%%%
%%% INPUTS:
% ecog: n x 1, ECoG feature data
% gyro: n x 1, gyro data
% bins: bins (with fixed bin size from 0 to 1) to bin data accordingly
```

```
% slope: slope of the logistic function

%%% OUTPUTS:
% m2: measurement model
% x0: logistic function midpoint
%%%%%%%%%%%%%%%%%%%%%%%%%%%%%%%%%%%%%%%%%%%%

% Train x0
% Optimal lag between signals
[r,lags] = xcorr(ecog,gyro);
[~,pos] = max(r);
opt_lag = lags(pos);

% Adjust w/ lag
ecog_cut = ecog(max([1,opt_lag+1]):end+min([0,opt_lag]));
gyro_cut = gyro(1-min([opt_lag,0]):end-max([0,opt_lag]));

% Normalized histogram for move/idle
[h1,~] = histcounts(ecog_cut(gyro_cut==0),[0;bins],'Normalization','
    probability');
[h2,~] = histcounts(ecog_cut(gyro_cut>0),[0;bins],'Normalization','
    probability');

x0 = bins(find((h2-h1)>0,1));

% New lambda
nbins = length(bins);
X = [ecog_cut,gyro_cut];
[N,c] = hist3(X,'Nbins',[1 1]*nbins);
p_ecog = sum(N,2);
N1 = N./repmat(p_ecog,1,nbins);
mean1 = sum(c{1}.*N1(1,:));
mean2 = sum(c{1}.*fliplr(N1(end,:)));
```

```
lambda = 1/mean([mean1,mean2]);

% New x0
X = [ecog_cut,gyro_cut>0.001];
[N,c] = hist3(X,'Nbins',[nbins 2]);
p_ecog = sum(N,2);
N1 = N./repmat(p_ecog,1,2);
x0 = bins(find(N1(:,1)<N1(:,2),1));

% New slope
slope = 1/mean(diff(bins));

%%%%%%
% lambda = mean(gyro_cut);
f1 = lambda*exp(-lambda*bins);
f2 = lambda*exp(lambda*bins)*exp(-lambda);
%%%%%

m = nan(length(bins),length(bins));
col = 0;

f1_norm = f1/sum(f1);
f2_norm = f2/sum(f2);

gamma_v = [];
for i = bins'
    gamma = 1/(1+exp(-slope*(i-x0)));
    gamma_v = [gamma_v,gamma];
    col = col+1;
    m(:,col) = (1-gamma)*f1_norm+gamma*f2_norm;
end

p_s_e = m;
```

```
[p_e_hist,edges] = histcounts(ecog_cut,length(bins),'Normalization','probability');
p_e = p_e_hist;
[p_s_hist,edges] = histcounts(gyro_cut,length(bins),'Normalization','probability');
p_s = p_s_hist';

p_e_m = repmat(p_e,length(bins),1);
p_s_m = repmat(p_s,1,length(bins));

p_e_s_raw = p_s_e .* p_e_m ./ p_s_m;

p_e_s = p_e_s_raw ./ repmat(sum(p_e_s_raw,2),1,length(nbins));

m2 = m./repmat(sum(m,2),1,length(bins)); % Normalized Measurement Model

m2 = p_e_s;

end
```

```
function [alpha,beta] = alpha_beta_train(gyro,bin_steps,downsample_factor,epsilon,fs)

%%%%%%%%%%%%%%%%%%%%%%%%%%%%%%%%%%%%%%%%%%%%
%%% INPUTS:
% gyro: n x 1, gyro data
% jumo_thresh: float, threshold that indicates a jump in data is a step
% downsample_factor: int, orig_fs/new_fs
% epsilon: float, width of x bins
% fs: sampling frequency of the signals

%%% OUTPUTS:
% alpha: float, alpha parameter for bayesian model
```

```
% beta: float, beta parameter for bayesian model
%%%%%%%%%%%%%%%%%%%%%%%%%%%%%%%%%%%%%%%%%%%%

d = diff(gyro);
d2 = d(d~=0);

delta_t = downsample_factor/fs;
alpha = var(d2)/2/epsilon^2*delta_t;

% Beta: count number of jumps from y
diff_bs = diff(bin_steps);
time_length = length(bin_steps)/fs;
beta = sum(abs(diff_bs)>0)/time_length*delta_t;

end
```

```
% Estimates probability of event occurring given x (predictor variables)
% and b (coefficients)

% 1. Inputs:
% - x: post-processed ecog channel data, x data used as input in the
    logistic regression (time samples x # channels)
% - b: coefficients of the regession, output of the logistic regression (
    # channels + 1 x 1 )

% 2. Outputs:
% - out: estimate of y data, input of the logistic regression,given the x
    data and the coefficients of the log regression (time samples x 1)

function out = logistic(b,x)

in = b(1) + x * b(2:end);

```

```
15 out = 1 ./ (1 + exp(-in));
16
17 end
```